

For Reference

NOT TO BE TAKEN FROM THIS ROOM

Ex LIBRIS
UNIVERSITATIS
ALBERTAENSIS



THE UNIVERSITY OF ALBERTA

Stimulated Brillouin Scattering in a CO₂ Laser-Plasma Interaction

by



Clinton Randy Giles

A THESIS

SUBMITTED TO THE FACULTY OF GRADUATE STUDIES AND RESEARCH

IN PARTIAL FULFILMENT OF THE REQUIREMENTS FOR THE DEGREE

OF Doctor of Philosophy

Department of Electrical Engineering

EDMONTON, ALBERTA

Fall 1983



Digitized by the Internet Archive
in 2023 with funding from
University of Alberta Library

<https://archive.org/details/Giles1983>

Abstract

A comprehensive set of experiments was performed to study stimulated Brillouin scattering (SBS) in a CO₂ laser-plasma interaction. The facility consisted of a TEA CO₂ laser producing either 1 GW, 40 ns FWHM gain switched laser pulses or 1.7 GW, 2 ns FWHM injection mode locked laser pulses which were focussed to 100 micron spot size onto an oxygen gas jet target. The measured average oxygen plasma conditions during the SBS were $n_e = 5 \times 10^{18} \text{ cm}^{-3}$, $T_e = 120 \text{ eV}$, $Z=6$ with the gain switched laser and $n_e = 3 \times 10^{18} \text{ cm}^{-3}$, $T_e = 150 \text{ eV}$, $Z=3$ with the injection mode locked laser. Strong ion wave damping, $\gamma_s/\omega_s \approx 0(1)$, was deduced for both cases from backscattered light spectra, reflected power and ruby Thomson scattering probing of the SBS driven ion modes. Two ion heating models were developed to interpret the convective SBS instability growth due to the large linear ion Landau damping. An ion trapping and heating description whereby only a fraction of the plasma ions was heated to temperature $O(ZT_e)$ was applicable to the 2 ns pump laser while a model incorporating energy balance with free streaming ions described the 40 ns pump laser under conditions of moderate SBS reflectivity. An 80 micron SBS interaction region measured by temporally and spatially resolved ruby Thomson scattering was explained through axial plasma density gradients.

An important experiment demonstrated SBS suppression with a multiline CO₂ pump laser. This improved laser-plasma coupling is highly desirable for direct drive laser-fusion designs. The 14% single line laser reflectivity was reduced to less than 2% when the gain switched laser oscillated on two or more equal intensity lines with the line separation, $\Delta\omega$, greater than the homogeneous plasma growth rate, $\gamma_0 = 10^{12} \text{ s}^{-1}$. Anomalous SBS mode coupling took place when $\Delta\omega < \gamma_0$ and the SBS reflectivity was not severely reduced.

Acknowledgement

I would like to thank my supervisor, Dr. Allan Offenberger, for his permission to conduct research in his laboratory and for his excellent guidance and advice. I am especially grateful to Dr. Offenberger for clarifying the more difficult points encountered during this work.

I am thankful to all the members of the Plasma Group at the University of Alberta for illuminating discussions on many diverse topics in laser and plasma physics.

This research would not have been possible without the exceptional talents of the machine shop personnel and the departments's optics technologist, Barry Arnold.

The financial support from the National Research Council of Canada and the Government of Alberta during the past four years is gratefully acknowledged.

Finally, my wife, Marion, gave the much needed love, patience and understanding to help me through my studies.

1. Experimental Methods	21
1.1 Outline of the Experimental Methods	21
1.2 Laser	25
1.2.1 TEA Carbon Dioxide Laser	25
1.2.2 Operation Mode-Locking of the TEA CO ₂ Laser	29
1.2.3 TEA Laser Model	43
1.2.4 Multi-wavelength Operation of the TEA CO ₂ Lasers	45
1.3 Target Chamber	62
1.3.1 Oxygen Gas Jet Target	64
1.3.2 CO ₂ Laser Focusing	68
1.4 Infrared Light Detection	80
1.5 Plasma Electron Temperature Measurement	85
1.6 Plasma Electron Density Measurement	88
1.7 Ruby Laser Triggered Scattering	92
2. Results	77
2.1 Introductory Remarks on the Experimental Results	77
2.2 Interferometric Measurements of the Plasma Density	77
2.3 Electron Temperature Measurements	82

Table of Contents

Chapter	Page
1. Introduction	1
1.1 Motivation for Research into Laser–Plasma Interactions	1
1.2 Early work in Stimulated Brillouin Scattering	2
1.3 Objective of this Work	4
2. Theory	6
2.1 Purpose of this Chapter	6
2.2 Dispersion Relations	7
2.3 Coupled Mode Equations	14
2.3.1 General System of Equations	14
2.3.2 Spatial Coupled Mode Solutions	17
2.3.3 Temporal Coupled Mode Equations	29
3. Experimental Methods	34
3.1 Outline of the Experimental Methods	34
3.2 Lasers	35
3.2.1 TEA Carbon Dioxide Laser	35
3.2.2 Injection Mode–Locking of the TEA CO ₂ Laser	39
3.2.3 IML Laser Model	43
3.2.4 Multiwavelength Oscillation of the TEA CO ₂ Lasers	48
3.3 Target Chamber	52
3.3.1 Oxygen Gas Jet Target	54
3.3.2 CO ₂ Laser Focussing	59
3.4 Infrared Light Detection	63
3.5 Plasma Electron Temperature Measurement	65
3.6 Plasma Electron Density Measurements	65
3.7 Ruby Laser Thomson Scattering	68
4. Results	77
4.1 Introductory Remarks on the Experimental Results	77
4.2 Interferometric Measurements of the Plasma Density	77
4.3 Electron Temperature Measurements	83

4.4	Preliminary Observations on Brillouin Scattering	85
4.5	Infrared Light Diagnostics	89
4.5.1	Backscattering with a Gain Switched CO ₂ Laser	89
4.5.2	IML Laser Backscatter Spectra	95
4.6	Stimulated Brillouin Scattering with a Multiline CO ₂ Laser	99
4.7	Ruby Thomson Scattering Measurements of SBS Ion Modes	103
4.7.1	Determination of Absolute Level of Ion Fluctuations	104
4.7.2	Spatially Resolved Thomson Scattering	107
4.7.3	SBS Ion Acoustic Fluctuation Wavenumber	111
4.7.4	Temporally Resolved SBS Ion Fluctuations	114
4.7.5	Wavelength resolved Thomson Scattering	118
4.8	Termination of SBS in the Laser-Plasma Interaction	121
5.	Conclusions	124
	Bibliography	126
	Appendix A	131
	Nonlinear Equations	131
	Ordinary Differential Equations	131
	Deconvolution of Spectra	132
	Abel Transform	133
	Plasma Susceptibility Calculation	133
	Appendix B	135
	Free Jet Program	135
	Appendix C	141
	Fresnel Mirrors Interferometer	141

List of Tables

Table	Page
3.1 TEA CO ₂ Laser Design Features	36
3.2 IML Laser System Performance	42
3.3 Some Line Combinations in a Multiwavelength IML Laser	51

List of Figures

Figure	Page
2.1 Temporal Growth Rates of Stimulated Brillouin Scattering	12
2.2 Solutions to the Spatial Coupled Mode Equations	18
2.3 SBS Reflectivity with Ion Heating Model	24
2.4 SBS Reflectivity in Ion Heating Model with Multiline Pump	25
2.5 Two Particle Distributions for Ion Trapping	27
2.6 Ion Trapping Model Estimates of SBS Reflectivity	30
2.7 Solutions to the Temporal Coupled Mode Equations	32
3.1 Gain Switched CO ₂ laser Output	38
3.2 Injection Mode Locked CO ₂ laser	40
3.3 Simplified CO ₂ -N ₂ Energy Level Diagram	44
3.4 Comparison of IML Laser Model to Experimental Results	47
3.5 Top View of the Target Chamber	53
3.6 Gas Target Design	55
3.7 n/n_c in the Oxygen Jet Flow	58
3.8 Meridional Ray Tracing of the CO ₂ Laser Focus	60
3.9 Off Axis Parabola Focus	62
3.10 Ruby Laser Interferometer	66
3.11 Thomson Scattering Wave Vectors in an SBS Experiment	70
3.12 Thomson Scattering Experiment. Streak Camera Configurations are Shown.	72
3.13 Main Components for Streak Camera Thomson Scattering	74
4.1 Gain Switched Laser Plasma Interferogram and Abel Inverted Density Profiles.	79
4.2 Plasma Electron Density Profiles 3 ns after the start of SBS	80
4.3 Electron Density Profiles for an IML Laser Irradiated Plasma	82
4.4 Electron Temperature for a Gain Switched Laser Irradiated Plasma	84
4.5 Gain Switched Laser Transmission and SBS	86
4.6 SBS and Thomson Scattering From an IML Laser Irradiated Plasma	88
4.7 Backscattered Light Spectra from a Gain Switched Laser Irradiated Plasma	91

Figure	Page
4.8 SBS Reflectivity from an IML Laser Irradiated Plasma	96
4.9 SBS Spectra for an IML Laser	98
4.10 SBS Reflectivity for a Multiline Laser	100
4.11 Multiline CO ₂ Laser Backscatter Spectra	102
4.12 Blackbody Calibration of Thomson Scattering Photomultiplier Detector	105
4.13 SBS Ion Fluctuation Levels Determined from Thomson Scattering	108
4.14 Time evolution of the Spatial Distribution of SBS Ion Fluctuations (Gain switched Laser)	110
4.15 Time Evolution of the Spatial Distribution of SBS Ion Fluctuations (IML Laser)	112
4.16 Wavenumber Spectrum of SBS Ion Fluctuations Determined from Thomson Scattering	113
4.17 SBS Ion Fluctuation Growth (Gain Switched Laser)	115
4.18 SBS Risetime Estimates from Ion Trapping	119
4.19 Time Integrated Thomson Scattered Light Spectrum	120
B.1 Flow fields and Mach Lines in a Gas Jet	136
C.1 Principal Interferometer Components	142
C.2 Interferometer Design Parameters	144

1. Introduction

1.1 Motivation for Research into Laser-Plasma Interactions

Current research in direct drive laser fusion has revealed the complex behaviour of laser-plasma interactions. Ideally, when a suitable fuel pellet is irradiated with high enough laser light intensity, it will be isentropically compressed and the ions thermally heated to thermonuclear burn resulting in large energy yields [1]. However, in both the overdense core of the irradiated target and the coronal plasma, many instabilities and laser-plasma effects take place to prevent such an event. Of interest here are those parametric instabilities which can occur in the ablated coronal plasma surrounding the target and consequently degrade the laser-plasma coupling. One instability, the photon to plasmon plus phonon parametric decay, has been postulated to be a useful absorptive instability to enhance the laser heating of the target. Unfortunately, this is only one of four similar resonant normal mode triplets which occur in the underdense plasma of the target corona. Stimulated Raman scattering (SRS) of the incident pump laser produces reflected photons and Langmuir waves in plasma density $\leq 1/4 n_c$, where n_c is the critical density for the particular laser frequency. Another parametric instability, stimulated Brillouin scattering (SBS) couples two photons to the ion acoustic wave. Both SRS and SBS are reflective type instabilities where a large fraction of the incident light energy is converted to reflected light. At the high laser intensities required to initiate fusion, these processes may be severe, even at densities much less than n_c , where the absorptive decay do not occur. SBS is especially recalcitrant as it can occur in any density, $0 < n < n_c$, and it has a low threshold in most laser plasmas. The objective of this thesis research was to study stimulated Brillouin backscatter in a CO₂ laser-plasma interaction and experimentally investigate the plasma and laser effects which may limit its growth.

1.2 Early work in Stimulated Brillouin Scattering

The first theoretically predicted parametric decay in a plasma was a Langmuir wave pumping another langmuir wave and an ion acoustic wave (Oraevsky and Sagdeev [2]). It was nine years later when this particular decay was experimentally observed in a laboratory plasma (Franklin et al. [3]). Since then, other parametric instabilities including the photon decays, SRS, SBS and two plasmon decay have been studied both theoretically and experimentally. All these parametric instabilities are normal mode resonant triplets where energy exchange takes place with frequency and wavenumber matching of the participating waves satisfying their respective plasma dispersion relations. Written explicitly, these are:

$$\omega_0 = \omega_1 + \omega_2$$

$$\underline{k}_0 = \underline{k}_1 + \underline{k}_2$$

$$\epsilon_i(\omega_i, k_i) = 0 \quad i = 0, 1, 2$$

where ω is the wave frequency, \underline{k} is the wave vector and $\epsilon_i = 0$ is the dispersion relation for a particular wave. The subscripts denote the participating waves with 0 identifying the externally provided pump wave. It is clearly seen by multiplying the frequency and wavevector sum rules by Planck's constant, \hbar , that energy and momentum are conserved as the pump wave decays to the two product waves.

Early theoretical work by Nishikawa [4] generalized the parametric process for infinite homogeneous plasma. Here, two oscillators were coupled through a third pump field and the threshold and growth rates were derived. Perkins and Flick [5] further considered the decay of an electromagnetic wave including wavenumber and frequency mismatches due to plasma inhomogeneities. Rosenbluth [6] clarified this situation by solving the WKB coupled mode equations through Laplace transform methods arriving at expressions for absolute growth in an inhomogeneous plasma. Rosenbluth et al. [7] later extended this work by discussing the evolution of temporal growth to convective saturation.

Pesme et al. [8] presented a particularly lucid exposition of the coupled equations for constant pump which described both absolute and convective wave growth as

affected by damping in cases of a homogeneous plasma, finite length plasma or inhomogeneous plasma. Their homogeneous bounded plasma equations describing the Brillouin instability are representative of the WKB approach:

$$\begin{aligned}\partial a_- / \partial t + c_- \partial a_- / \partial x &= \gamma_0 n^* \\ \partial n^* / \partial t + c_s \partial n^* / \partial x + \gamma_s n^* &= \gamma_0 a_-\end{aligned}$$

where c_- is the phase velocity of the backscattered electromagnetic wave with action a_- , and c_s is the ion sound speed associated with the ion fluctuation n . The coupling coefficient, γ_0 , is proportional to the pump electromagnetic field and γ_s is the ion wave damping. Upon solving for a dispersion relation where $\gamma_s = 0$, absolute instability in homogeneous plasma was predicted if the plasma dimension exceeded the gain length $\pi(c_- c_s)^{1/2} / 2\gamma_0$. Wave damping imposed the usual instability threshold condition, $\gamma_0 > (\Gamma_- \gamma_s)^{1/2}$, where Γ_- is the electromagnetic wave damping. Also, because of wave energy convection out from the bounded plasma, convective instability took place if $\gamma_0 > (\gamma_s / 2)(c_- / c_s)^{1/2}$. A result which is directly applicable to many stimulated Brillouin experiments came from ignoring the time derivatives and assuming strong ion wave damping. In this case, the instability growth length $c_- \gamma_s / \gamma_0^2$, was derived from the coupled equations. Finally, the case of inhomogeneous plasma showed that the characteristic dimension of the unstable region was $\approx (k')^{-1/2}$, where k' is the spatial derivative of the wave number mismatch, $k = (k_0 - k_1 - k_2)$.

A significant departure from the above descriptions came with Drake et al. [9] using the plasma fluid equations to derive a general dispersion relation for parametric instabilities. The earlier WKB models required that the spatial and temporal wave growths be small compared to the real wavenumber and frequencies. Drake et al. imposed no restriction on the pump field amplitude (within nonrelativistic theory) whereby the decay waves were no longer necessarily normal modes of a field free plasma and could therefore have growth rates comparable to their wavenumbers and frequencies. Forslund et al. [10] extended this work with examples of Brillouin and Raman scattering in both

fluid and kinetic limits of the plasma susceptibilities. In a second paper, Forslund et al. [11] showed computer simulation results and discussed nonlinear effects in the instability growth and saturation. Later work by Cohen and Max [12] generalized the studies of various parametric instabilities, including stimulated Brillouin scattering through a Green's function formulation.

Experimental studies of laser induced plasma parametric instabilities are recent when compared to earlier observations of Brillouin and Raman scattering in other materials. While Brillouin scattering from phonons in solids was detected by Chiao et al. in 1964 [13], it was not until the early 1970's that Brillouin scattering measurements in plasma were made. Both solid and gas targets have been used in the parametric instability research with high power Nd:glass and carbon dioxide lasers. The initial Brillouin experiments at low laser intensities and plasma electron densities showed fractions of a percent SBS reflectivity [14], but with increased laser power and plasma densities, reflectivities approaching unity have been measured [15]. It is clear from these high reflectivities that the seriousness of stimulated Brillouin scattering in laser fusion experiments entitles it to intensive theoretical and experimental research.

1.3 Objective of this Work

This thesis attempts to sort out the dominant laser and plasma effects which saturated the stimulated Brillouin backscatter and limited its growth rate in a series of experiments. In the experiments, a free oxygen jet was irradiated with either a long pulse, gain switched CO₂ laser pulse or a short pulse, injection mode locked (IML) CO₂ laser pulse. The long pulse laser was used to produce a well characterized, highly ionized plasma from which the laser light could then scatter. The short pulse laser generated fast rising, high intensity light pulses where comparisons to the gain switched laser results revealed the importance of different ion heating mechanisms in saturating the Brillouin instability. In particular, ion heating is examined and found to explain both the instability's temporal and spatial growth.

Chapter 2 summarizes theoretical considerations of stimulated Brillouin scattering in laser-plasma experiments. Both the generalized dispersion relation and nonlinear coupled mode equations are examined. The coupled mode approach is shown to be

particularly amenable to incorporating a wide variety of problems in both spatial and temporal instability growth. With these equations, ion heating and ion trapping models are developed.

Apparatus and diagnostic techniques are fully explained in Chapter 3. This is an important chapter describing the IML laser system, laser focussing and the oxygen gas target. Also, the infrared light detection equipment used to monitor the Brillouin backscattered light and the ruby laser Thomson scattering method are described.

The experimental results and deductions made from them are contained in Chapter 4. The plasma parameters are measured through interferometry and X-ray measurements. Next, preliminary observations on the Brillouin instability are given. The remainder of the chapter presents measurements of the backscattered light and of the ion sound waves of the Brillouin instability. These results were interpreted to show ion trapping and heating and plasma density inhomogeneity as the major contributors inhibiting the instability's growth. An important experiment was also performed to demonstrate Brillouin reflectivity reduction with a multiwavelength pump laser. Concluding remarks in Chapter 4 propose several mechanisms which could explain the sudden termination of the Brillouin scattering in the laser-plasma interaction.

2. Theory

2.1 Purpose of this Chapter

In this chapter, the theory of Stimulated Brillouin (Compton) scattering is studied with emphasis on those aspects relevant to the experiments discussed in Chapter 4. Geometrical effects on the instability are ignored and all theories will be explained through one dimensional models. Further details will be given in the analysis of the experiments based on the concepts presented here. Introductory remarks on Brillouin scattering have already been given in the first chapter and will not be repeated in this chapter.

This chapter is divided into three sections. First, the Brillouin dispersion relation derived from Maxwell's equations, Poisson's equation and Vlasov's equation is examined in both fluid and kinetic limits for temporal and spatial growth. These results apply to low amplitude waves and describe the instability's strength and bandwidth before nonlinear effects modify its behaviour. These new normal modes are not necessarily the eigenmodes of the field free plasma. The second section of this chapter is centered on examining first order coupled wave equations derived from fluid and Poisson's equations. These equations easily describe the weakly coupled temporal growth and spatial distribution of the participating waves as well as provide a simplified insight into distinguishing between convective and absolute wave growth. Nonlinear behaviour in Brillouin scattering is examined in this section. The coupled mode equations are solved for the simplest case where direct ion heating and pump depletion control the instability's spatial growth. An added benefit of the coupled equations is the straightforward extension of this model to the case of a multiwavelength laser pump which will be shown to decrease the backscattered light. A second simple model, that of ion trapping, is also incorporated into the coupled mode equations and provides an alternate description of the spatial growth. All these simplified analyses are phenomenological descriptions rather than self-consistent solutions to the wave amplitudes and plasma particle energy. The latter approach is generally not tractable except through particle simulations, whereas a phenomenological approach allows a reasonable physical picture of the different plasma effects.

2.2 Dispersion Relations

The usual two component plasma dispersion relation for low amplitude electrostatic waves in the absence of other strong electrostatic or electromagnetic waves is well known, i.e. $\epsilon = 1 + \chi_i + \chi_e = 0$ where χ_i and χ_e are the ion and electron susceptibilities respectively. For a particle velocity distribution $f_j(u)$ and for a wave with phase velocity ω/k ,

$$\chi_j = \frac{\omega_p^2}{k^2} \int \frac{\partial f_j / \partial u}{u - \omega/k} du \quad \text{Eq. 2.1}$$

where ω is the wave frequency and k is its wavenumber. The free plasma eigenmodes are those which are weakly damped. For the ion acoustic wave, the solution to this dispersion relation is the familiar

$$\omega_s/k_s = c_s = [(ZT_e + 3T_i)/M_i]^{1/2}/(1 + k^2\lambda_D^2) \quad \text{Eq. 2.2}$$

where Z is the ionization state, $T_{e(i)}$ the electron (ion) temperature, M_i the ion mass and λ_D the plasma Debye length. The imaginary frequency component is given by the Landau formula (neglecting electron contribution)

$$\text{Im } \omega = \omega_s (\pi/8)^{1/2} (ZT_e/T_i)^{3/2} \exp(-ZT_e/2T_i - 3/2) \quad \text{Eq. 2.3}$$

In the presence of a large amplitude electromagnetic wave, strong parametric coupling in the plasma can take place between it and electrostatic or other electromagnetic waves. The dispersion relation is modified from above since the solution can now admit temporal and spatial growth of the daughter waves at the expense of the pump field energy. These parametric instabilities include Raman and Brillouin scattering of the incident pump wave, the latter being of greatest interest here.

The dispersion relation for parametric instabilities has been derived many times before (Forslund et al. [10], Drake et al. [9], Cohen and Max [12]) and its derivation will be outlined here. The incident linearly polarized electromagnetic pump wave satisfies the usual dispersion relation $\omega_0^2 = \omega_p^2 + c^2 k_0^2$ since the temporal and spatial

growth rates of the instability are still small compared to ω_0 and k_0 , where ω_0 is the pump frequency, k_0 is its free space wavenumber and $\omega_p = (ne^2/\epsilon_0 m_e)^{1/2}$ is the plasma frequency. The wave equation for the sideband modes, $(\omega_{\pm}, \underline{k}_{\pm}) = (\omega \pm \omega_0, \underline{k} \pm \underline{k}_0)$ generated, together with the density fluctuations, $\delta n_{e,i}(t) \propto \exp(i(\underline{k} \cdot \underline{x} - \omega t))$ when Fourier transformed yields

$$[(k_{\pm}^2 - \omega_{\pm}^2/c^2)\underline{I} - \underline{k}_{\pm}\underline{k}_{\pm}] \cdot \underline{E}_{\pm} = -\omega_p^2/c^2(\delta n_e(\underline{k}, \omega)/n_0)\underline{E}_{0\pm} \quad \text{Eq. 2.4}$$

where \underline{E}_{\pm} is the sideband electric field and $\underline{E}_{0\pm}$ is that of the pump. This equation describes the forcing function acting on the homogeneous wave equation. Equating $\underline{E}_{0\pm}$ to 0 reduces the description to that of a freely propagating electromagnetic wave in the plasma. Also note at this point that the resonance conditions, $\text{Re}(\omega_0) = \text{Re}(\omega_{\pm} \pm \omega)$, $\text{Re}(\underline{k}_0) = \text{Re}(\underline{k}_{\pm} \pm \underline{k})$ apply, making this a linear model without higher harmonic wave coupling. From Vlasov and Poisson's equations, the electron fluctuation density and particle electrostatic potential are

$$\begin{aligned} \delta n_e(\underline{k}, \omega) &= \frac{k^2}{4\pi e} [\phi(\underline{k}, \omega) + \psi(\underline{k}, \omega)/e] \chi_e(\underline{k}, \omega) \\ \phi(\underline{k}, \omega) &= \frac{-4\pi}{k^2} \sum_j e_j \delta n_j \end{aligned} \quad \text{Eq. 2.5}$$

The ponderomotive potential, $\psi(\underline{k}, \omega)$ which drives the low frequency electron fluctuations is

$$\psi = \frac{e^2}{m\omega_0^2} |\underline{E}_{0+} \cdot \underline{E}_{-} + \underline{E}_{0-} \cdot \underline{E}_{+}| \quad \text{Eq. 2.6}$$

Substituting Equations 2.5 and 2.6 into 2.4 and eliminating δn_e in 2.4 finally yields the general dispersion relation

$$\frac{1}{\chi_e} + \frac{1}{1+\chi_i} = k^2 \left[\frac{|\underline{k}_{-} \times \underline{v}_{0s}|^2}{k_{-}^2 D_{-}} - \frac{|\underline{k}_{-} \cdot \underline{v}_{0s}|^2}{k_{-}^2 \omega_{-}^2 \epsilon_{-}} + \frac{|\underline{k}_{+} \times \underline{v}_{0s}|^2}{k_{+}^2 D_{+}} - \frac{|\underline{k}_{+} \cdot \underline{v}_{0s}|^2}{k_{+}^2 \omega_{+}^2 \epsilon_{+}} \right] \quad \text{Eq. 2.7}$$

where

$$D_{\pm} = c^2 k^2 \pm 2 \underline{k} \cdot \underline{k}_0 c^2 \mp 2 \omega \omega_0 - \omega^2$$

$$\epsilon_{\pm} = 1 + \chi_e(\omega_{\pm}, k_{\pm}) + \chi_i(\omega_{\pm}, k_{\pm})$$

and $v_{os} = (eE_0/m_e \omega_0)^{1/2}$, the electron quiver velocity. The ion Vlasov equation was also used to eliminate δn_i in 2.4 and ion ponderomotive force terms were ignored. The usual approach is to disregard the nonresonant antiStokes components (ω_+, k_+) and for Brillouin (and Raman) scattering, the electrostatic wave is coupled to two electromagnetic waves. The reduced dispersion relation is then

$$\frac{1}{\chi_e} + \frac{1}{1 + \chi_i} = \frac{k^2 v_{os}^2 \cos^2 \theta}{D_-} \quad \text{Eq. 2.8}$$

where θ is the angle between the incident and scattered electromagnetic wave vectors. From D_- in Equation 2.7, with $|\omega| \ll \omega_0$, which is certainly true for an ion acoustic wave, Equation 2.8 can be conveniently rewritten for Brillouin backscatter ($\theta = \pi$).

$$\omega = \Delta\omega + \frac{\omega_{pe}^2}{8\omega_0} \frac{v_{os}^2}{v_e^2} \frac{(1 + \chi_i)}{1 + \chi_i + \chi_e} \quad \Delta\omega = (\underline{k} \cdot \underline{k}_0 - k^2/2) c^2/\omega_0 \quad \text{Eq. 2.9}$$

When the real part of the second term on the RHS of Equation 2.9 is much less than ω_s , the real frequency component is $\approx \Delta\omega$ since $k \approx 2k_0$ which can be shown from the weak coupling dispersion relations. The electrostatic wave phase velocity is

$$\text{Re}(\omega)/\text{Re}(k) = (c_s + u)$$

where u is the plasma flow speed and c_s in the weakly coupled instability is given by Equation 2.2. However, in general, c_s may be strongly dependent upon the electromagnetic field amplitudes if the ponderomotive force is comparable to the free ion acoustic oscillation restoring force (i.e. $\psi/e \approx 0(\phi)$ in Equation 2.5). In

the limit of the fluid description, $v_e \gg \omega/k \gg v_i$, the particle susceptibilities are $\chi_i \approx -\omega_{pi}^2/\omega^2$, $\chi_e \approx k_{de}^2/k^2$ ($k_{de} = 1/\lambda_D$). Upon substituting into the Brillouin dispersion relation for strong coupling where $k^2 v_o^2 \omega_{pi}^2/8\omega_o^2 \gg k^3 c_s^3$, the solution for temporal growth is easily shown to be

$$\text{Re}(\omega) = \frac{1}{2} (\cos\Theta)^{2/3} (\omega_{pe}^2 k_o^2 v_{os}^2/2\omega_o^2)^{1/3}$$

$$\text{Im}(\omega) = \sqrt{3} \text{Re}(\omega)$$

Eq. 2.10

$$k = 2 k_o \cos\Theta$$

This is often called the reactive quasimode solution [16]. The spatial problem of stronger wave damping will be dealt with later.

Temporal growth with strong dissipation of the ion acoustic wave through linear ion Landau damping occurs for $(ZT_e/T_i) \approx 0(1)$ and the strongly coupled fluid dispersion relation is no longer valid. The ion acoustic wave is shifted to lower frequency and kinetic susceptibilities must be used in Equation 2.9. An iterative calculation method was used to evaluate complex frequencies for a given real wavenumber. These results describe the initial growth of the instability. Equation 2.9 is normalized and separated into its real and imaginary parts which describe the real frequency and growth respectively of the instability

$$\Omega_R = \frac{\Delta\omega}{2k_o v_i} + B \left\{ (1 + \text{Re}\chi_i) \left[1 + \frac{k_{De}^2}{(2k_o)^2} \frac{1}{K^2} + \text{Re}\chi_i \right] + (\text{Im}\chi_i)^2 \right\}$$

$$\Omega_i = B \frac{k_{De}^2}{(2k_o)^2 K^2} \frac{1}{K^2} \text{Im}(\chi_i)$$

Eq. 2.11

$$B = \frac{\omega_{pe}^2 v_{os}^2}{16k_o \omega_o v_i v_e^2} \left[\left(1 + \frac{k_{De}^2}{(2k_o)^2} \frac{1}{K^2} + (\text{Im}\chi_i)^2 \right)^{-1} \right]$$

where $K = k/2k_o$, $\Omega = \omega/2k_o v_i$. The ion susceptibility is given by

$$x_i(\omega, k) = (k_{Di}/k)^2 W(z) \quad \text{Eq. 2.12}$$

where

$$z = \Omega/K$$

$$W(z) = z\Gamma(z/\sqrt{2})/\sqrt{2} + 1$$

with Γ the usual plasma dispersion function (Fried and Conte [17]). Numerical computation of $\Gamma(z)$ was accomplished with a continued fraction method in the region $|y| > 1$ where $z = x + iy$ and otherwise, a convergent series for $W(z)$ (Ichimaru [18]) was used for $-1 \leq y \leq 1$. These calculation routines are summarized in Appendix A. Double precision calculations were necessary for $W(z)$ as it was calculated with a large term alternating series. Initial values of Ω_r and Ω_i were calculated from Equation 2.10 and substituted into the RHS of Equation 2.11. The Ω_r and Ω_i calculated from Equation 2.11 were then substituted back into the RHS. This iterative procedure with the appropriately chosen initial values rapidly converged to the solution of the dispersion relation.

Figure 2.1 shows the solution of the dispersion relation under conditions of moderate Landau damping ($ZT_e/T_i = 6$) and strong Landau damping ($ZT_e/T_i = 1.5$). For each graph, the strongly coupled limit $\Omega_i/\Omega_r = \sqrt{3}$ and the weak coupling $\Omega_r = \sqrt{ZT_e/T_i + 3}$ are indicated by solid and dashed lines respectively. It is apparent from these plots that strong coupling dominates in the parameter space of interest as the $\Omega_i/\Omega_r = \sqrt{3}$ line traces the peak growth almost exactly in both cases. As the pump intensity increases, both the instability growth rate and its bandwidth increase. It must be remembered that these are exponential growth rates and the experimentally observed relative amplitudes of the different frequency waves are modified by this growth. It is also clear that for decreasing pump intensity or increasing ion Landau damping, the real frequency of the ion wave approaches the weakly coupled frequency. This is expected because as the driving ponderomotive force decreases, the quasimode approaches the normal eigenmode of the free plasma. Also, with increased ion Landau damping the instability growth is diminished and the interaction waves are weakly coupled.

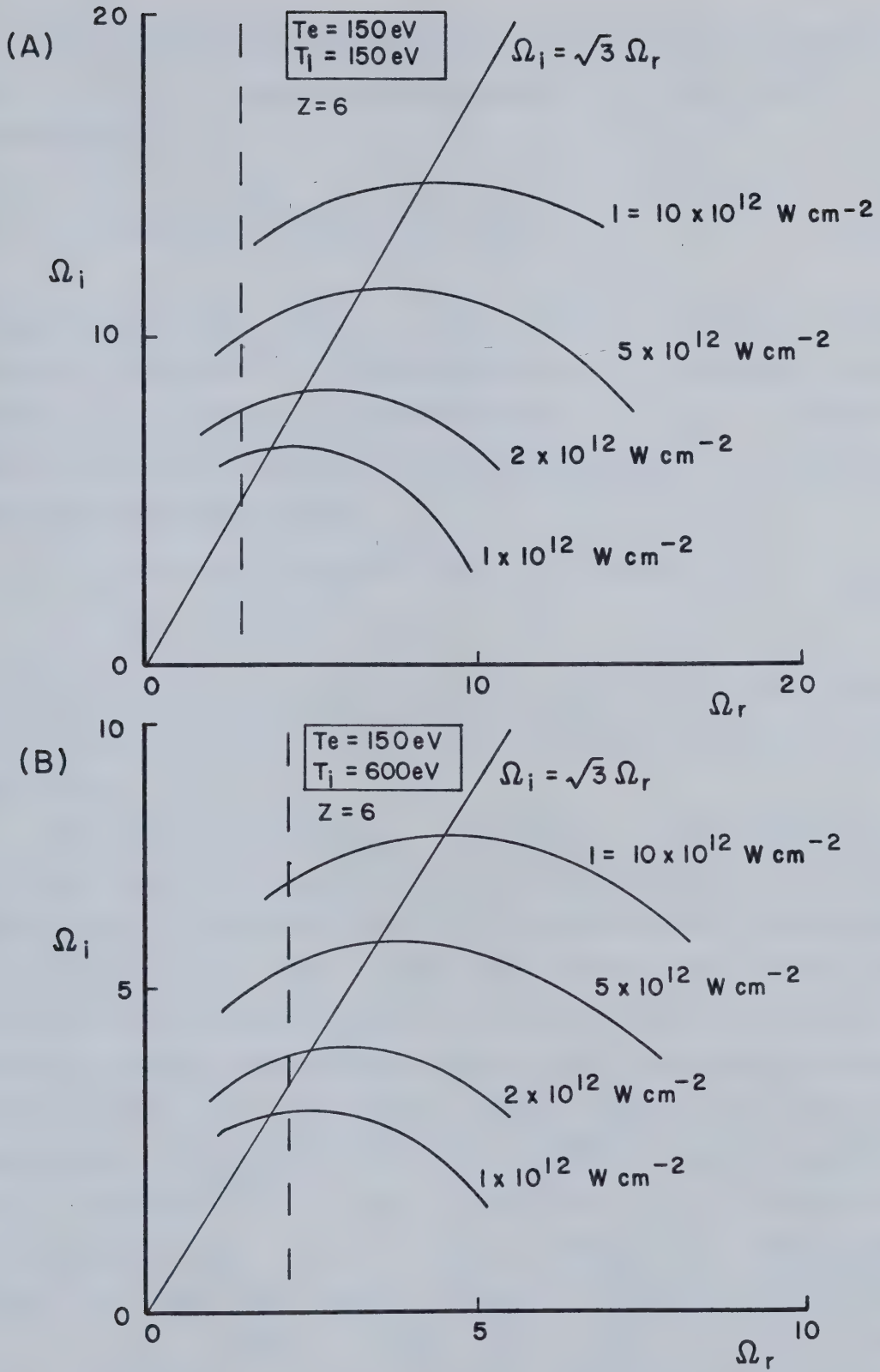


Figure 2.1 Temporal Growth Rates of Stimulated Brillouin Scattering

Even with strong temporal coupling, the real wavenumber does not deviate much from $2k_0$. Figure 2.1 was calculated for $k = 2k_0 \pm 0.2\%$. From Equation 2.9

$$\Delta\omega/\omega_s \approx \sqrt{1 - n/n_c} (c/(c_s + u))(1 - K) \quad \text{Eq. 2.13}$$

This equation shows that $\Delta\omega/\omega_s$ is $\approx c/c_s$ times that of $\Delta k/k$ and that the real frequency is strongly affected by the real wavenumber of the ion acoustic wave. In a weak electromagnetic pump field $\Delta\omega \approx \omega_s$ and from the dispersion relations for the electrostatic wave and electromagnetic waves and also from wavenumber and frequency matching

$$\begin{aligned} k &\approx 2k_0 (1 - 2c_s/c\sqrt{1 - n/n_c}) \quad u = 0 \\ n_c &= \epsilon_0 \omega_0^2 m_e / e^2 \end{aligned} \quad \text{Eq. 2.14}$$

From Equation 2.14 one sees that even for strong coupling with significant departures from the weak coupling ion sound speed, the wavenumber for significant growth is always close to $2k_0$.

After several growth periods $0(1/\text{Im}(\omega))$, nonlinear departures from this temporal growth and convection saturate the wave amplitudes. Different possible nonlinear effects will be explored more fully in the next two sections, but in any case, saturation can occur and temporal growth cease although spatial gain may still be sufficient to permit convective growth of the instability. From Figure 2.1, again, one notices that in the limit of strong damping on the ion waves, the real frequency moves to the weak coupling result as the imaginary frequency diminishes. The coupled mode equations given in the next section will be more convenient for describing spatial growth when $\text{Im}(k)/\text{Re}(k) \ll 1$ and $\text{Im}(\omega)/\text{Re}(\omega) \ll 1$. However, notice from Equation 2.11 that $\Omega_i = 0$ when $\text{Im}(\chi_i) = 0$ which provides a criterion for spatial wave growth. A zero of $\text{Im}(\chi_i)$ is approximately $z = 1 - i1$; thus $\text{Im}(k) = \text{Re}(k) = 2k_0$ and it is easy to show $\omega/\text{Re}(k) \approx 2v_i$. This regime corresponds to Compton scattering where the pump wave is scattered from the heavily damped ion wave [19]. Thus after a

few temporal growth periods the Brillouin scattering can evolve to strong convective growth. A more exact analysis of Equation 2.8 by Forslund et al [10] shows that this strong spatial coupling occurs for $v_{os}/v_e > 4ck_0/\omega_p$, a normally difficult regime to achieve experimentally, and the broad wavenumber spectrum is centered around $2k_0$.

2.3 Coupled Mode Equations

2.3.1 General System of Equations

The results of the last section showed the general dispersion relation and nominal behaviour for parametric instability in a homogeneous plasma. The spatial distribution and amplitudes of the various waves were not derived since the dispersion relation only provides complex ω , k without consideration for the nonlinear effects required to saturate wave growth. From Maxwell's equations and the 2 component plasma fluid equations, a set of coupled second order partial differential equations can be derived which describes the spatial and temporal evolution of the pump field, scattered electromagnetic wave and ion acoustic fluctuations [20]. Apart from being restricted to a linear fluid description of the Brillouin instability, the equations are quite general. However, considerable simplification is possible if WKB approximations to the mode amplitudes are invoked, i.e.

$$\begin{aligned} E_0(x,t) &= e_0(x,t) \exp(i(\underline{k}_0 \cdot \underline{r} + \omega t + \int \Delta \underline{k}_0 \cdot d\underline{r})) + c.c. \\ E_-(x,t) &= e_-(x,t) \exp(i(\underline{k}_- \cdot \underline{r} + \omega t + \int \Delta \underline{k}_- \cdot d\underline{r})) + c.c. \\ n_s(x,t) &= \tilde{n}_s(x,t) \exp(i(\underline{k}_s \cdot \underline{r} + \omega t + \int \Delta \underline{k}_s \cdot d\underline{r})) + c.c. \end{aligned} \quad \text{Eq. 2.15}$$

c.c. = complex conjugate

where e_0 , e_- and \tilde{n}_s are assumed to be slowly varying quantities in time and space as compared to the corresponding frequency and wavenumber of the mode. The integral expression is for slowly varying phase changes due to wave dispersion. Substitution of these expressions into the second order differential equations reduces them to first order equations describing the field amplitudes of the waves. The three

simultaneous coupled equations obtained are

$$\begin{aligned}
 \partial a_0 / \partial t + c_0 \partial a_0 / \partial x &= -\omega_{pe}^2 \hat{n}_s / \omega_0 N_0 \cdot a_- \exp(-i \int \Delta k_0 - \Delta k_- - \Delta k_s \, dx) / 4 \\
 \partial a_- / \partial t + c_- \partial a_- / \partial x &= \omega_{pe}^2 \hat{n}_s / \omega_0 N_0 \cdot a_0 \exp(i \int \Delta k_0 - \Delta k_- - \Delta k_s \, dx) / 4 \\
 \left(\frac{\partial}{\partial t} + \gamma_s + c_s \frac{\partial}{\partial x} \right) \frac{\hat{n}_s}{N_0} &= \frac{v_{os}^2}{2} \frac{m_e}{M_i} \frac{k_s^2}{\omega_s} a_0 a_- \exp(i \int \Delta k_0 - \Delta k_- - \Delta k_s \, dx)
 \end{aligned} \tag{Eq. 2.16}$$

where γ_s is the ion wave damping coefficient. In Equation 2.16, the electromagnetic field amplitudes have been normalized to

$$a_- = (k_- / k_0)^{1/2} e_- / E_0 \quad a_0 = e_0 / E_0$$

where E_0 is the peak incident amplitude of the pump electromagnetic field. Electromagnetic wave damping has not been incorporated in Equation 2.16 since in most instances of interest here, inverse bremsstrahlung absorption is weak in the Brillouin interaction zone. Phase mismatch between the waves is accounted for through the exponential factor on the right hand side of Equation 2.16. Mismatch sources include density gradients affecting the electromagnetic waves whereas velocity and temperature gradients cause changes in the ion mode frequency. The dispersion relations for these waves clearly show their dependence on these plasma inhomogeneities, i.e.

$$\begin{aligned}
 k &= \frac{\omega}{c} \sqrt{1 - n/n_c} && \text{Electromagnetic Waves} \\
 \omega_s &= k_s c_s + \underline{k_s} \cdot \underline{u} && \text{Ion Acoustic Waves}
 \end{aligned} \tag{Eq. 2.17}$$

Further reduction of Equation 2.16 can be effected through non-dimensionalizing time and space coordinates and renormalizing the density fluctuation. Different time and length scales are appropriate in the two cases of temporal or spatial problem. The complex wave amplitudes can then be separated to rewrite the three complex equations into a system of six real equations. The resulting system of equations is then

$$\begin{aligned}
(|c_s|/c)(\partial\alpha_0/\partial\tau) + (c_0/c)(\partial\alpha_0/\partial\zeta) &= -\alpha_-\alpha_s \cos(H(\zeta)+\phi) \\
(|c_s|/c)(\partial\alpha_-/\partial\tau) + (c_-/c)(\partial\alpha_-/\partial\zeta) &= \alpha_0\alpha_s \cos(H(\zeta)+\phi) \\
\beta\alpha_s + \partial\alpha_s/\partial\tau + \partial\alpha_s/\partial\zeta &= \alpha_0\alpha_- \cos(H(\zeta)+\phi) \\
(|c_s|/c)(\partial\theta_0/\partial\tau) + (c_0/c)(\partial\theta_0/\partial\zeta) &= (\alpha_-\alpha_s/\alpha_0)\sin(H(\zeta)+\phi) \\
(|c_s|/c)(\partial\theta_-/\partial\tau) + (c_-/c)(\partial\theta_-/\partial\zeta) &= (\alpha_0\alpha_s/\alpha_-)\sin(H(\zeta)+\phi) \\
\partial\theta_s/\partial\tau + \partial\theta_s/\partial\zeta &= (\alpha_0\alpha_-/\alpha_s)\sin(H(\zeta)+\phi) \\
\phi &= \theta_0 - \theta_- - \theta_s
\end{aligned}
\tag{Eq. 2.18}$$

The complex wave amplitudes have been expressed as $a_j = \alpha_j \exp(i\theta_j)$, where $j = 0, -, s$ and α_j, θ_j are real quantities. The ion wave amplitude renormalization is

$$a_s = \sqrt{2k_0/2k_s} (\omega_{pe}/\omega_0)(v_e/v_{os})(\tilde{n}_s/N_0)$$

and the new space and time coordinates are $\zeta = x(\gamma_0/\sqrt{cc_s})$ and $\tau = t(\gamma_0/\sqrt{c/c_s})$; γ_0 is the homogeneous instability growth rate. The gradient phase mismatch integral is $H(\zeta) = \int \Delta k_0 - \Delta k_- - \Delta k_s d\zeta$ and β is the normalized ion sound wave dissipation term

$$\beta = \sqrt{(k_s^3/k_0^3)} (\omega_0/\omega_p)(v_e/v_{os})(\gamma_s/\omega_s) \tag{Eq. 2.19}$$

Various simplifications to Equation 2.18 can be made for different special cases of instability growth. The usual approximation is to assume phase locking for maximum wave growth. Here, $\phi = 0$ and the cosine factor on the right hand side of the wave amplitude equations is maximum so that wave coupling in Brillouin scattering is largest. Plasma gradients can still affect phase mismatch through $H(\zeta)$ and limit the spatial growth region. Only cases of $\phi = 0$ and simplifications to either temporal or spatial problems will be examined here.

2.3.2 Spatial Coupled Mode Solutions

A full solution of the remaining three equations in Equation 2.18 can be obtained directly and the time asymptotic spatial distribution of the wave amplitudes can be computed. This steady state Brillouin interaction is the solution to the coupled mode equations where time derivatives are ignored. The simplified steady state, homogeneous plasma equations are

$$\begin{aligned}\partial\alpha_0/\partial\zeta &= -\alpha_-\alpha_s \\ \partial\alpha_-/\partial\zeta &= -\alpha_0\alpha_s \quad (c_-/c = -1) \\ \partial\alpha_s/\partial\zeta + \beta\alpha_s &= \alpha_0\alpha_- \end{aligned} \quad \text{Eq. 2.20}$$

with boundary conditions

$$\alpha_0(0) = 1 \quad \alpha_-(0) = \sqrt{R} \quad \alpha_s(0) = \epsilon'$$

The first condition states that the pump electromagnetic wave enters the interaction region with full intensity at $\zeta = 0$ while the second is the reflected electromagnetic wave amplitude as it exits the unstable region. The power reflectivity,

R is normalized to the incident pump intensity. For subsonic plasma flow (see Manheimer et al [21] for supersonic flow), the ion acoustic wave experiences spatial growth as it convects in the $+\zeta$ direction with initial amplitude $\epsilon' = 0$ for $\zeta = 0$.

Equations 2.20 are numerically integrated and the solutions are plotted in Figure 2.2 for several boundary conditions and damping parameter β to show how the spatial wave distribution and amplitude are affected by these parameters. The amplitudes α_-^2 and α_s^2 are plotted since it is the wave intensity which is normally detected in an experiment for both the electromagnetic waves (with suitable light detectors) and ion acoustic waves (through Thomson scattering diagnostics). The spatial invariant $\alpha_0^2 - \alpha_-^2 = 1 - R$ can be identified from the first two

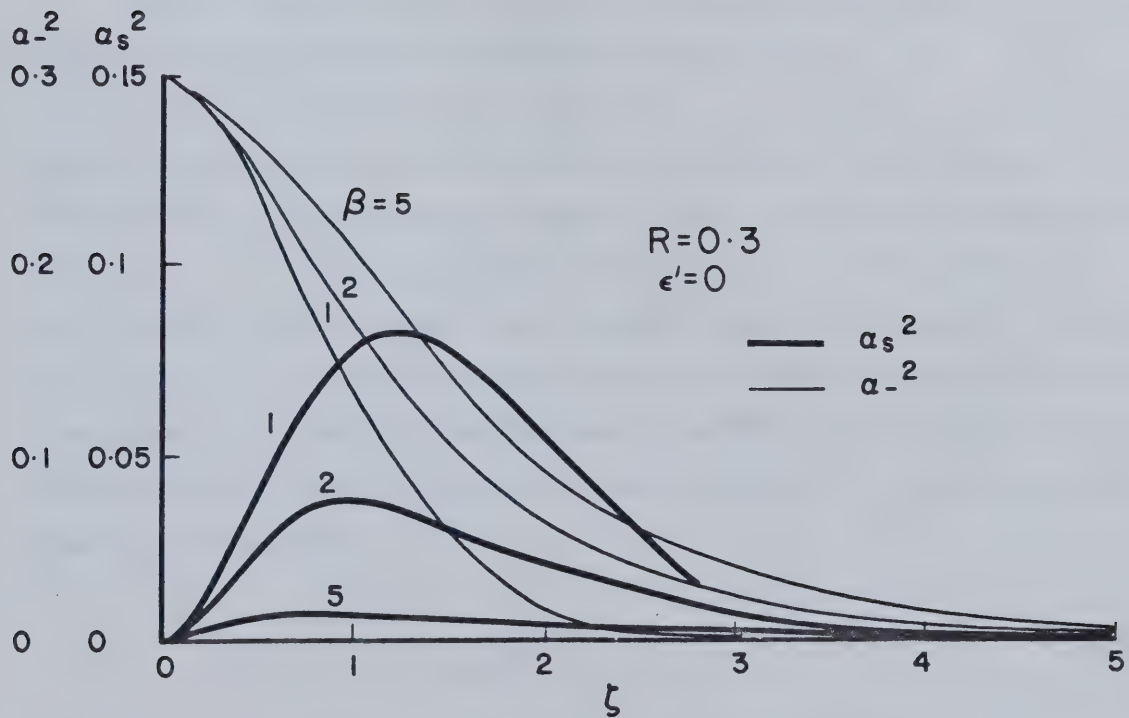
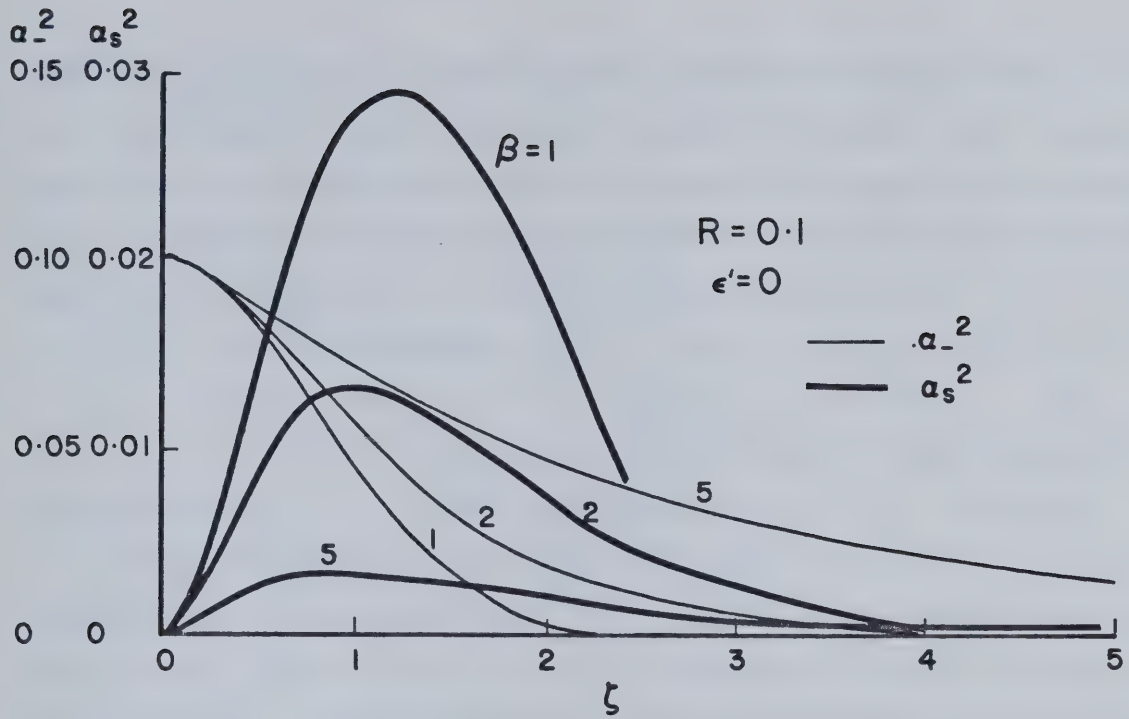


Figure 2.2 Solutions to the Spatial Coupled Mode Equations

equations of 2.20. There are several interesting features to these plots. First, for the same electromagnetic wave reflectivity, the peak ion fluctuation level decreases significantly for increased wave damping. The compensating effect is for the unstable region to enlarge so that there is sufficient growth of the reflected electromagnetic wave to attain the specified R . This is evident upon comparing the $\beta = 1$ and $\beta = 5$ spatial distributions of α_-^2 for $R = 0.1$. At $\zeta = 2.4$, α_-^2 vanishes for $\beta = 1$ whereas for $\beta = 5$, even at $\zeta = 5$, α_-^2 is 0.01 which is still too large for most plausible noise sources from which α_- may convectively grow in the $-\zeta$ direction.

A second observation from Figure 2.2 is that for $\beta = 1$, absolute instability can exist in steady state since α_-^2 can be zero and yet the waves grow. For $R = 0.1$ and $\beta = 1$, α_-^2 is zero at $\zeta = 2.4$ and grows to 0.1 at $\zeta = 0$. The ion acoustic wave does not simultaneously vanish but rather convects out of the unstable region and is damped. In general, absolute instability can be created for $\beta < 2$, but with increased ion wave dissipation the instability is convective (Forslund et al. [10]).

Another important observation which will lead to further simplification of the coupled equations is related to the ion wave distribution. From $\zeta = 0$, α_s^2 grows rapidly to its peak value because both α_0 and α_- are near maximum and the coupling on the right hand side of Equation 2.20 is large. As ζ increases, the ion wave amplitude passes through a maximum and decreases with declining α_- . What is significant is that for large wave dissipation α_s^2 is more slowly varying through the unstable region. This suggests that for $\beta \gg 1$, the ion fluctuation can be approximated as constant and the spatial derivative in the ion wave coupled equation ignored. With this assumption, an analytic expression for the reflectivity from a plasma slab of length L can be derived from Equation 2.20 (Tang [22])

$$R(1 - R) = \epsilon(\exp(G(1 - R)) - R) \quad \text{Eq. 2.21}$$

where

$$G = \frac{k_0 L}{4} \frac{n}{n_c} \left(1 - \frac{n}{n_c} \right)^{1/2} \frac{v_{os}^2}{v_e^2} \frac{1}{2\gamma_s/\omega_s} \quad \text{Eq. 2.22}$$

and $\alpha_-^2(L) = \epsilon$ is the boundary condition representing the scattered wave noise source from which the instability convectively grows. The fluctuation level, \tilde{n}_s/N_0 is now related to the reflectivity through

$$\tilde{n}_s/N_0 = 0.5(v_{os}/v_e)^2 (1/[2\gamma_s/\omega_s]) \sqrt{R} \quad \text{Eq. 2.23}$$

The most obvious source of red shifted electromagnetic noise would be reflection from a moving plasma boundary. If plasma densities greater than n_c are created during plasma formation, unity reflectivity of the pump electromagnetic wave can occur. Low reflectivity from plasma density gradients is also a significant electromagnetic noise source. It can be shown (Born and Wolf [23]) that the reflectivity R of a plasma boundary with a linear density gradient from n/n_c to 0 over a distance L is given by $R = |r|^2$ where,

$$r = \int_0^L \frac{1}{2N} \frac{dN}{dx} \exp(k_0 i \int_0^x N(z) dz) dx \quad \text{Eq. 2.24}$$

$$\text{and } N(x) = \sqrt{1 - xn/n_c L}$$

For example, $R = 3.6 \times 10^{-4}$ for $n/n_c = 0.5$ and $k_0 L = 25$ which, as will be seen in the data analysis of Chapter 4, is a reasonable noise level to seed convective instability.

The ion acoustic wave damping γ_s in Equation 2.22 can be treated as a phenomenological damping coefficient. However, if the electron and ion temperatures are known for a Maxwellian plasma, the kinetic ion Landau damping coefficient can be substituted for the hydrodynamic value resulting in

$$\omega_s/2\gamma_s = \text{Im}[(1 + x_i)/(1 + x_i + x_e)] \quad \text{Eq. 2.25}$$

This result can be readily shown by comparison of the coupled mode growth rate to the temporal growth rate from the kinetic dispersion formula, i.e.

$$\begin{aligned} \gamma &= 2\gamma_0^2/\gamma_s && \text{COUPLED MODE} \\ &= (\omega_{pe}^2/8\omega_0)(v_{os}^2/v_e^2) \operatorname{Im}[(1+x_i)/(1+x_i+x_e)] && \text{KINETIC} \end{aligned}$$

Offenberger et al. [24] used the random phase approximation (see Tsytovich [25] for a thorough explanation of this approach). to arrive at the same expression for a monochromatic pump field. This earlier result demonstrated the equivalence of the random phase model and the coherent pump model in the limit of strong ion wave damping. Substitution of the kinetic expression for the electron and ion susceptibilities results in

$$\frac{\omega_s}{2\gamma_s} = \sqrt{\pi} \frac{ZT_e}{T_i} \frac{x \exp(-x^2)}{[1+(ZT_e/T_i)(1-2x\exp(-x^2)\int_0^x \exp(t^2)dt)]^2 + (ZT_e/T_i)^2 \pi^2 x^2 \exp(-x^2)}$$

Eq. 2.26

where

$$x = \sqrt{M_i/2K_B T_i} (\omega_- - \omega_0)/|\underline{k}_- - \underline{k}_0|$$

Real frequencies and wavenumbers are used to evaluate x since the coupled mode equations apply to weak spatial coupling for which Equation 2.26 is being applied to a steady state solution. The wavenumber difference is $|\underline{k}_- - \underline{k}_0| = |\underline{k}_s|$ and in Equation 2.14 was shown to be very close to $2k_0$. Equations 2.21, 2.22 and 2.26 thus give gain as a function of the ion wave frequency shift through γ_s/ω_s .

What remains to be done to complete the description of the heavily damped ion wave model is to determine the electron and ion temperature ratio and the fraction n_t/n of the ion distribution which is contributing to the wave damping. Two approaches can be taken. The first approach uses a very simple ion heating model

proposed by Phillion et al. [26] where the fraction of the pump wave power delivered to the ion wave given by the Manley–Rowe relations, ω_s/ω_0 , is converted to thermal energy for the entire ion population in the interaction zone. The effective ion temperature is calculated through balancing this input power with energy flow out of the unstable region as the heated ions stream out at their thermal velocity. This energy balance can be written as

$$n_i v_i T_i = IR(\omega_s/\omega_0) \quad \text{Eq. 2.27}$$

where I is the electromagnetic pump intensity. With ω_s determined from the weakly coupled ion acoustic dispersion relation and the above expression, ZT_e/T_i can be determined for a given pump intensity and reflectivity. For reflectivity calculations it is more useful to express the pump intensity as the dependent variable whereby it is then easy to show

$$\left(\frac{v_{os}}{v_e}\right)^2 = \frac{n}{n_c} \frac{1}{R} \left[\left(\frac{ZT_e}{T_i}\right)^{3/2} \left(1 + \frac{3T_i}{ZT_e}\right)^{1/2} \right]^{-1} \quad \text{Eq. 2.28}$$

Substitution of Equation 2.28 into Equation 2.22 together with Equation 2.26 is the ion heating model for steady state Brillouin scattering. The result of this substitution is

$$R(1-R) = \epsilon \exp \left[\frac{k_0 L}{4} \left(1 - \frac{n}{n_c}\right)^{1/2} \left(\frac{n}{n_c}\right)^2 \left(\frac{ZT_e}{T_i}\right)^{-3/2} \left(1 + \frac{3T_i}{ZT_e}\right)^{-1/2} \left(\frac{1}{R} - 1\right) \frac{\omega_s}{2\gamma_s} \frac{1}{N} \right] \quad \text{Eq. 2.29}$$

A useful extension of this model has been made through introducing the integer divisor N in Equation 2.29. This corresponds to a multiline laser where N is the number of different equal intensity laser lines comprising the electromagnetic pump. If the frequency separation of these laser lines, $\Delta\omega_L$ is greater than the instability bandwidth, γ_0 , each line will act as an independent pump [27]. For $N > 1$, the reduced pump intensity for each scattering process results in a

significant decrease in the total scattered power due to the exponential dependence on N .

Relevant solutions for the ion heating model are plotted in Figures 2.3 and 2.4. Figure 2.3 shows the pump intensity dependence of the reflectivity at the ion wave frequency with maximum gain in Equation 2.29. The curves show the self-consistent electron-to-ion temperature ratios due to heating as well as reflectivity calculated for various noise levels as a function of pump power. Figure 2.4 is similar to Figure 2.3 except that a single noise factor $\epsilon = 10^{-3}$ is chosen, but more importantly, the reflectivity is shown for two plasma densities and the decreased reflectivity is illustrated for multiline pumps ($N = 2$ and 3).

Inspection of Figure 2.3 shows that ZT_e/T_i decreases with the pump wave intensity as expected through ion heating. For an oxygen gas target, with effective $Z = 6$, the ions are heated to the electron temperature for $(v_{os}/v_e)^2 \approx 0(1)$ but further increases in the pump intensity are slow to decrease ZT_e/T_i since ions are streaming out of the unstable region. In both Figures 2.3 and 2.4, an initial decline in the reflectivity is evident for increasing pump intensity as ion Landau damping increases. However, at some point the rate at which wave dissipation increases is unable to fully counteract the increasing pump and the reflectivity R begins to rise again. This transition in the reflectivity function occurs at $ZT_e/T_i = 4$. Also the weak influence of the noise level ϵ on the reflectivity is evident in Figure 2.3 and the logarithmic dependence can be seen from Equation 2.29. From Figure 2.3, a 10^4 variation in noise level changes the observed reflectivity by approximately a factor of 3. Finally, Figure 2.4 demonstrates the reduced scattered light reflectivity which can be obtained by dividing the pump into several equal intensity components. For the conditions of this calculation, the reduction factor is close to the number of lines participating; for example, the reflectivity decreases by approximately a factor of 2 when a 2 line pump is used. The decrease is not exponential because a lowered reflectivity moderates the ion heating and consequently ion Landau damping decreases. For the modest pump intensities and reflectivities of these calculations, the combined effects of pump intensity division and reduced ion wave damping allows only a small change in the Brillouin backscatter reflectivity. These results

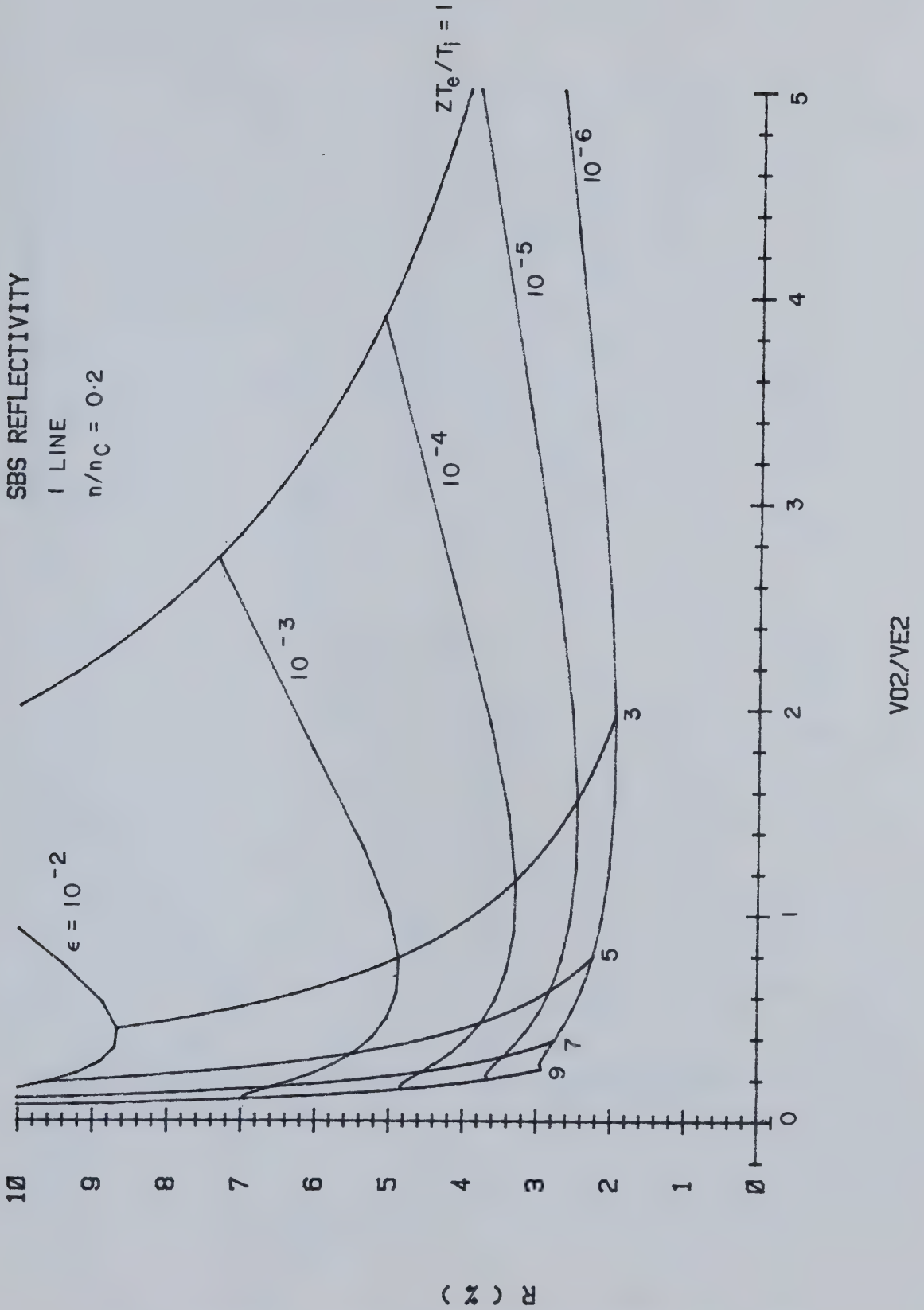


Figure 2.3 SBS Reflectivity with Ion Heating Model

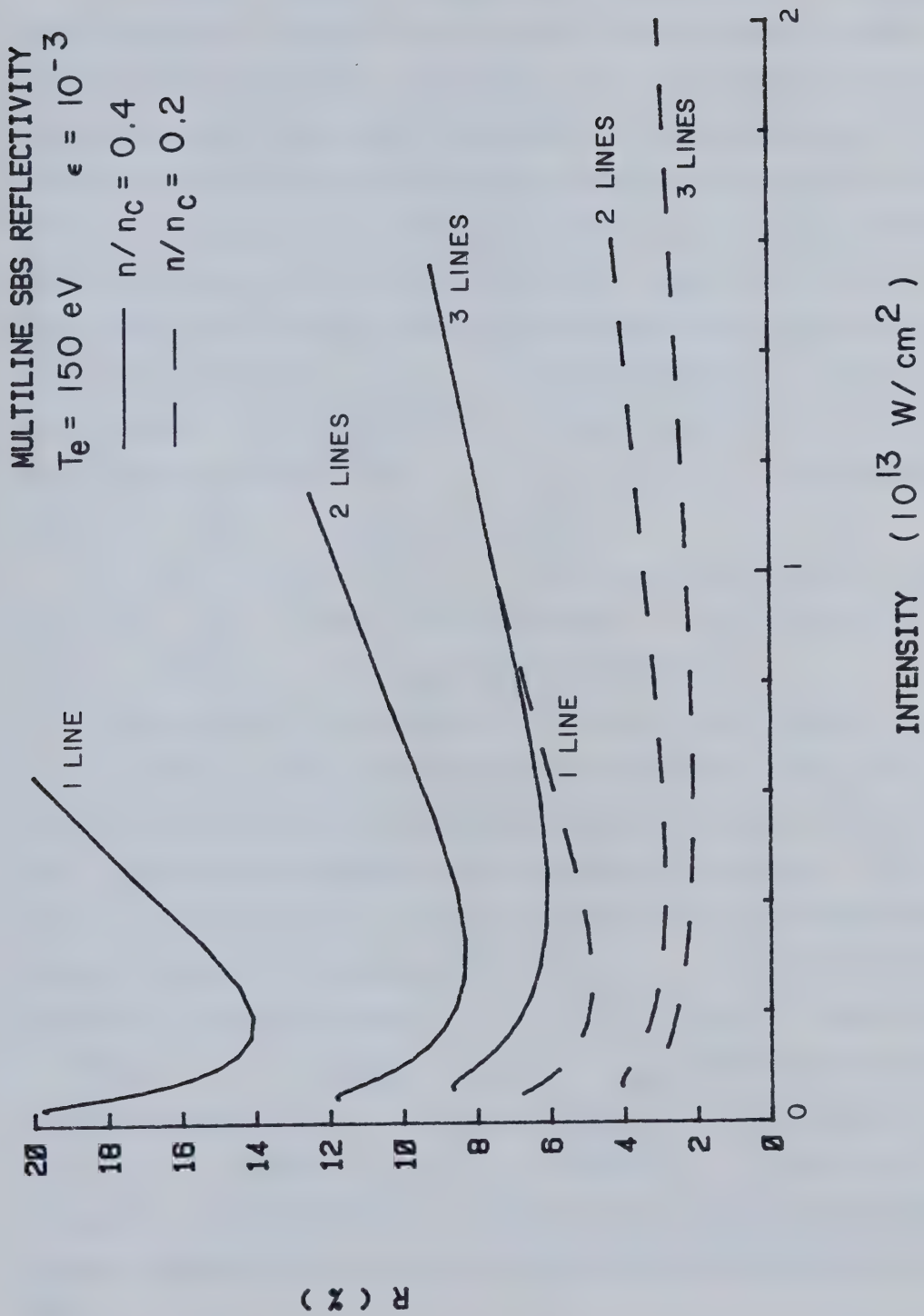


Figure 2.4 SBS Reflectivity in Ion Heating Model with Multiline Pump

will be very useful in the data analysis where the laser was tuned to oscillate on more than one line.

An alternative saturation mechanism to wave damping is ion trapping in the potential wells of a coherent ion wave. The trapping process has been described extensively in the literature (see for example, Ichimaru [18] or Davidson [28]) and will be outlined here only in the context of dissipating the ion sound waves driven through Brillouin scattering. Ions whose thermal velocity closely matches the phase velocity of the ion wave can be caught in the wave's electrostatic potential and be accelerated to the wave phase velocity. In the ion wave frame, these trapped particles bounce back and forth inside a single wavelength well and resonantly exchange energy with the ion sound wave. The velocity range, v_{tr} of the trapped particles is related to the ion wave potential $\phi = M_i v_{tr}^2 / 2e$ where ϕ is the ion wave potential related to the ponderomotive force $\phi \propto \underline{E}_0 \cdot \underline{E}$. Thus in the laboratory frame, ions whose velocities v are between $c_s - v_{tr} < v < c_s + v_{tr}$ can experience trapping. The bounce frequency, ω_B , of these trapped particles is $\omega_B \approx k(e\phi/M_i)^{1/2}$ and in times $0(1/\omega_B)$ the trapped ions are accelerated to $\approx c_s$.

There are two interpretations as to how the trapped ions can moderate the Brillouin instability. In one model, the ion wave amplitude can grow until a significant number of ions are trapped and therefore become an energy sink to clamp the ion wave level. A waterbag ion distribution is used to estimate the maximum \tilde{n}_s/N_0 of the ion wave. Figure 2.5(a) illustrates the uniform ion velocity distribution of the waterbag model and the relative position of c_s . From the kinetic dispersion calculations of the last section, $\tilde{n}_e = (1 + \chi_i)ek^2\phi$ from which, for $k^2\lambda_D^2 \ll 1$, $\tilde{n}_s/N_0 \approx e\phi/KT_e$. Together with the expression for the trapping velocity v_{tr} , the trapping range can be expressed as a function of \tilde{n}_s/N_0 . When $c_s - v_{tr} = \sqrt{3KT_i/M_i}$, ions in the waterbag distribution are trapped and there is an abrupt turn on of strong ion wave dissipation. The fluctuation amplitude at which this occurs is easily calculated from the above (Dawson et al [29])

(A) WATERBAG DISTRIBUTION



(B) MAXWELLIAN DISTRIBUTION

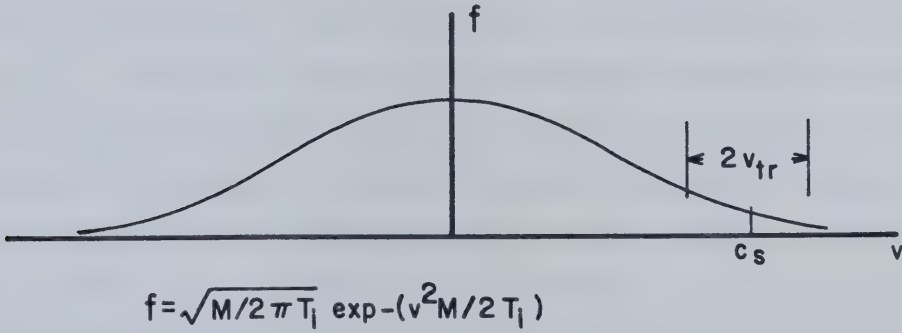


Figure 2.5 Two Particle Distributions for Ion Trapping

$$\tilde{n}_s/N_0 \approx 0.5[(1 + 3T_i/ZT_e)^{1/2} - (3T_i/ZT_e)^{1/2}]^2 \quad \text{Eq. 2.30}$$

This equation, together with the Bragg reflectivity relation

$$R = (\pi/2)(\tilde{n}_s/N_0)^2(n/n_c)^2(L/\lambda)^2$$

determine the saturated Brillouin reflectivity. For example, if $ZT_e/T_i = 6$, $L/\lambda = 10$ and $n/n_c = 0.5$, then $\tilde{n}_s/N_0 = 0.134$ from Equation 2.30 and the power reflectivity, R is 1.2%.

An alternative interpretation of ion trapping which also provides a useful connection to the ion heating model can be imagined. In this model, the fraction of ions trapped are assumed to be heated to a temperature $\approx ZT_e$, thereby creating a second distribution function on which the ion acoustic wave is linearly Landau damped (Manheimer et al. [21]). In any realistic laser-plasma interaction, the potential well coherence would not persist through the instability and a distribution of ion energies around ZT_e would result. This would not be unlike ion heating in that the ion isn't trapped for many bounce periods but is heated and convects in the direction of the ion wave. However, strong heating for only that fraction of particles in the trapping region occurs rather than the moderate heating of all ions in the ion heating model. This picture compares well with particle simulations done by Estabrook et al. [30] where equivalent damping occurred with only a fraction of the ions heated. The ion wave damping is thus moderated by that fraction of ions trapped, n_t/n . Figure 2.5(b) illustrates trapping for a Maxwellian ion distribution. The fraction of trapped ions is easily calculated by integrating the Maxwellian over the trapping region and gives

$$n_t/n = 0.5[\text{erf}(\sqrt{(ZT_e/T_i)}(1 + \sqrt{(2\delta n/n)}) - \text{sgn}(1 - \sqrt{(2\delta n/n)}) \cdot \text{erf}(\sqrt{(ZT_e/T_i)}|1 - \sqrt{(2\delta n/n)}|)] \quad \text{Eq. 2.31}$$

where

$$\text{erf}(z) = \frac{2}{\sqrt{\pi}} \int_0^z \exp(-x^2) dx$$

The effective wave damping is now $n_t/n \cdot \gamma_s/\omega_s$ where γ_s/ω_s is calculated from ion Landau damping with $T_i \approx ZT_e$. The ion wave damping coefficient, γ_s/ω_s is large i.e. $0(1)$ and the steady state, heavy damping reflectivity equation is rewritten as

$$R(1 - R) = \epsilon \left[\exp \left(\frac{k_o L}{8} \frac{\omega_s}{\gamma_s} \frac{n}{n_c} \frac{n}{n_t} \left(1 - \frac{n}{n_c} \right)^{1/2} \left(\frac{v_{os}}{v_e} \right)^2 (1 - R) \right) - R \right] \quad \text{Eq. 2.32}$$

The normalized ion fluctuation level, \tilde{n}_s/N_0 from Equations 2.23 and 2.32 completes this alternative ion trapping model. This model is not expected to accurately describe the instability growth at high reflectivities where the ion fluctuation is large. Figure 2.6 shows several solutions to these two equations. For increasing electron-to-ion temperature ratios the reflectivity increases at low intensities. This results from fewer particles being in the trapping region for increasing phase velocity. However, for $(v_{os}/v_e)^2 \geq 2$, most ions are trapped for all initial ZT_e/T_i and the damping does not change with further increases in $(v_{os}/v_e)^2$. From Figure 2.6 one also sees an initial decrease in reflectivity as a function of $(v_{os}/v_e)^2$ for large ZT_e/T_i . This occurs because the rate of increase of trapped particles with increasing pump is sufficient for the damping to outweigh the pump and although \tilde{n}_s/N_0 increases, the reflectivity does not.

2.3.3 Temporal Coupled Mode Equations

The steady state parametric instability is relatively straightforward to analyse because a system of ordinary differential equations describes the behaviour. When the instability's temporal growth must be dealt with, it is no longer obvious that a similar simplification of the coupled mode equations is valid. Obviously, if the wave amplitudes are constant throughout an infinite plasma, the spatial derivatives can be ignored and a system of three differential equations with only time derivatives describes the 3-wave decay. The appropriate temporal, spatial and density fluctuation normalizations to reduce Equations 2.16 are

$$t = 2\sqrt{2Z(ck_o/c_s k_s)} (v_e/v_{os}) (1/\omega_{pe}) \tau' = \tau'/\gamma_0 \quad x = c_s \zeta'/\gamma_0$$

$$\tilde{n}_s/N_0 = \sqrt{(2/Z)(c_s k_s/ck_o)} (\omega_o/\omega_{pe}) (v_{os}/v_e) \alpha_s$$

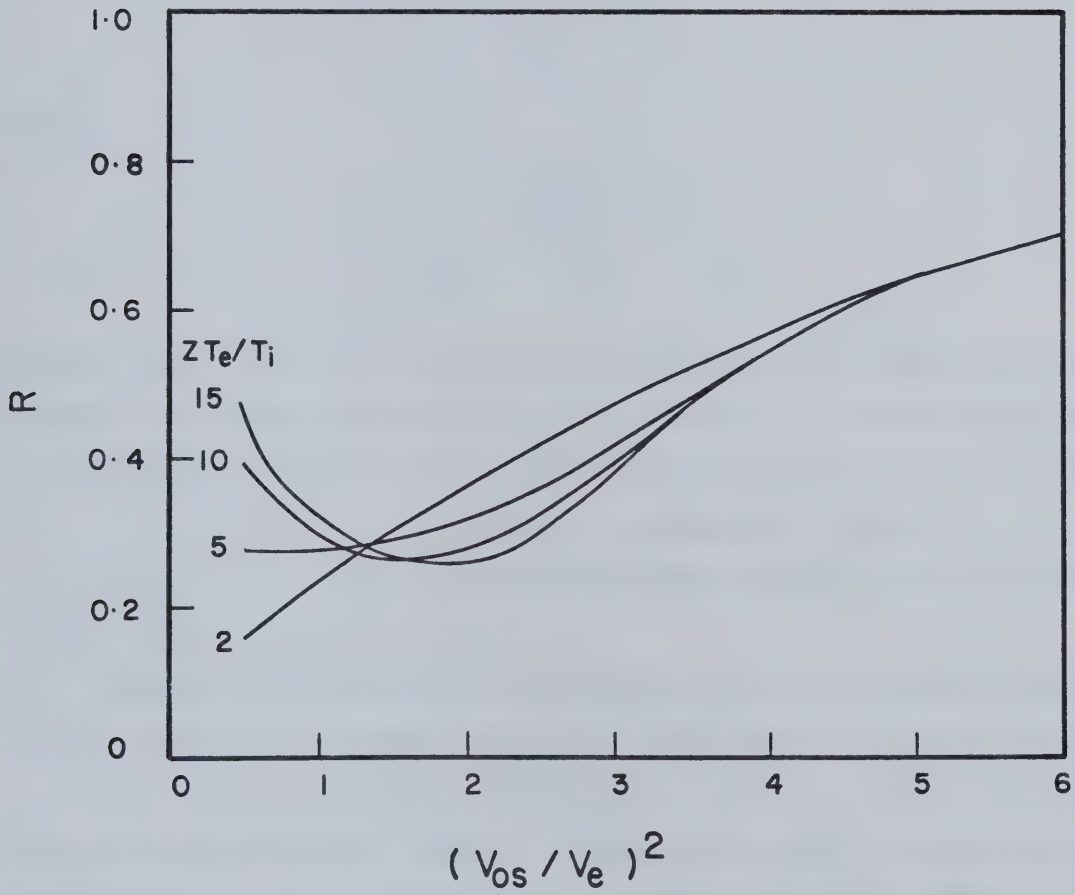


Figure 2.6 Ion Trapping Model Estimates of SBS Reflectivity

Note that the time scale is $0(1/\gamma_0)$ where γ_0 is the homogeneous plasma growth rate. The temporal equations are thus given by

$$\begin{aligned}\partial \alpha_0 / \partial \tau' &= -\alpha_- \alpha_s \\ \partial \alpha_- / \partial \tau' &= \alpha_0 \alpha_s \\ \partial \alpha_s / \partial \tau' + \beta' \alpha_s &= \alpha_0 \alpha_- \end{aligned} \quad \text{Eq. 2.33}$$

where

$$\beta' = \sqrt{2Z} \frac{v_e}{v_{os}} \frac{\gamma_s}{\omega_s} \left(\frac{c_s k_s}{c k_0} \right)^{1/2} \frac{\omega_0}{\omega_{pe}}$$

Equation 2.33 is very similar to Equation 2.20 describing the steady state problem except in one important respect. The sign of the driving term is reversed in the second equation and consequently the conservation law from the first two equations of 2.33 is $\alpha_0^2 + \alpha_-^2 = 1$ (initial conditions $\alpha_0(0) = 1$, $\alpha_-(0) = 0$). Thus the system electromagnetic energy is constant within the approximation $\omega_s/\omega_0 \ll 1$.

Weiland and Wilhelmson [31] have examined Equations 2.33 and their conclusions will be outlined and expanded upon here. When there is no wave dissipation, $\beta' = 0$ and the solution to the system of equations are Jacobi elliptic functions.

These functions describe oscillatory exchange of energy between the two electromagnetic waves and amplitude modulation of the ion acoustic wave. With ion wave dissipation however, the oscillations damp out and the system relaxes to

$\alpha_0 = \alpha_s = 0$ and $|\alpha_-| = 1$; all the energy has been transferred to the decay electromagnetic wave. Figure 2.7 is a plot of α_-^2 and α_s^2 for several β' . For $\beta' > 0$, the wave amplitudes stabilize to their steady state values in times $0(10/\gamma_0)$ with some ringing. Increased dissipation limits the ion wave's peak amplitude which after several oscillations, becomes negligible. Once

$\alpha_s = 0$, there is no parametric coupling of the electromagnetic waves and the instability ceases with the end result of the pump wave completely depleted and

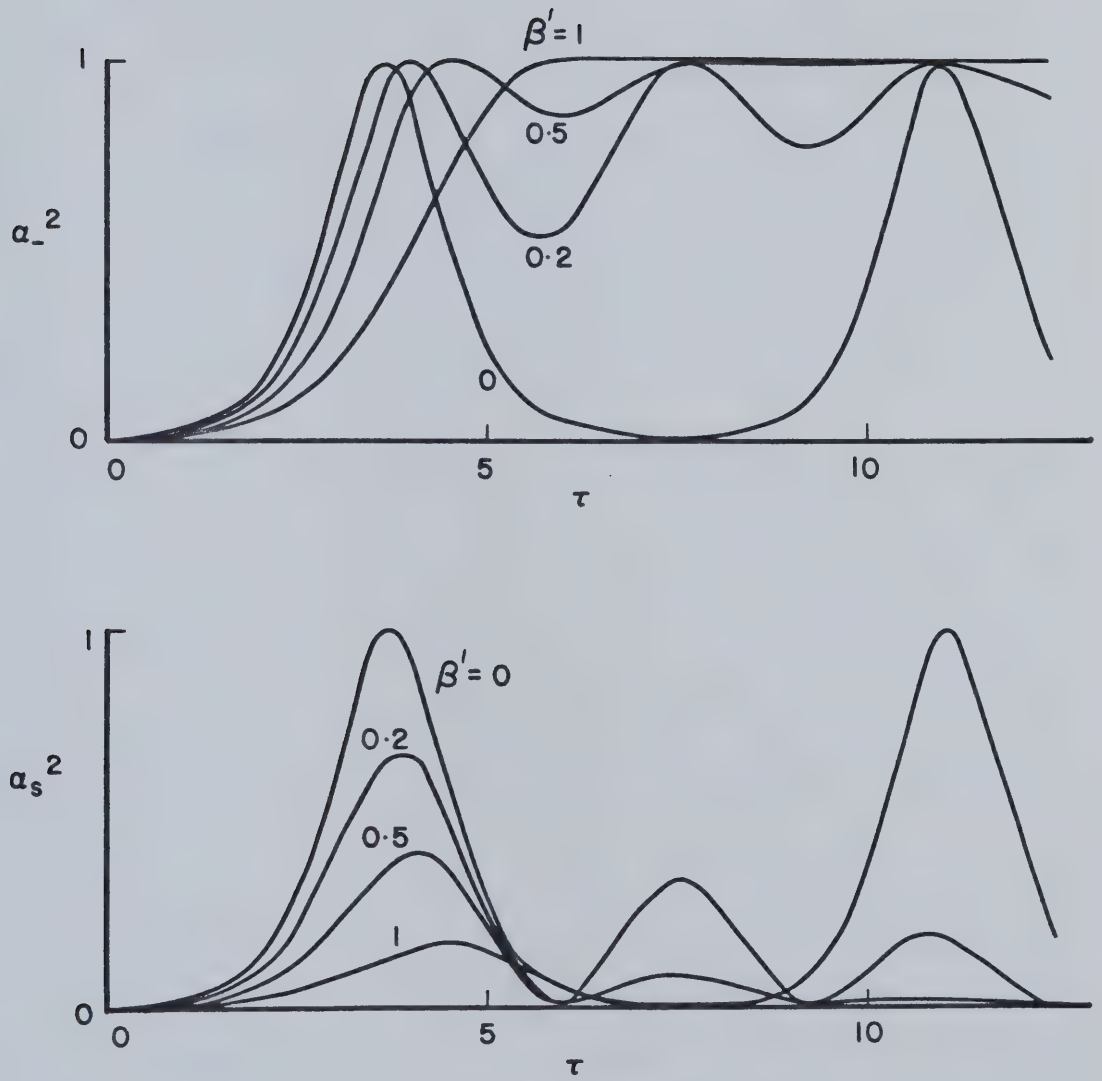


Figure 2.7 Solutions to the Temporal Coupled Mode Equations

converted to the scattered electromagnetic wave.

3. Experimental Methods

3.1 Outline of the Experimental Methods

A considerable number of diverse experiments were performed in the course of this laser-plasma interaction research. There were two broad classes of experiments; firstly those experiments from which laser or plasma parameters were measured and secondly, those experiments where the laser-plasma interaction was diagnosed. Examples of the first type are laser injection mode locking and interferometric plasma electron density measurements while the second class included backscatter light and ruby laser Thomson scattering measurements. This range of experiments required a wide variety of instrumentation and the purpose of this chapter is to explain this apparatus and its implementation.

The experimental facility consisted of two high power carbon dioxide lasers and an evacuated target chamber in which a focussing mirror and gas jet target were located. Most of the interaction experiments in laser fusion use either planar or spherical solid targets. The interpretation of Brillouin measurements from these experiments is complicated by large density and velocity gradients in the underdense coronal plasma. Also, solid targets often have limited diagnostic access, particularly for forward scattered or transmitted signals. These reasons alone motivate one to use gas targets when studying SBS.

Suitable ports on the target chamber allowed entry of the laser light as well as viewing accessibility for the different diagnostic experiments. Electronic equipment for synchronizing the firing of the two CO₂ lasers with the gas target generation was located in a Faraday cage screen room. Other control instrumentation and oscilloscopes were also located in this screen room to reduce electromagnetic interference generated from the high voltage laser discharges. When operational, the entire laser-target system could be fired and data collected once every 45 seconds. In this time the CO₂ laser capacitors were recharged, the target chamber was evacuated to remove the spent target gas and then refilled with a low pressure static helium fill. Of course the data obtained from any shot was specific to the experiment being conducted. The different experimental methods to be detailed in this chapter include carbon dioxide laser injection mode locking

and multiwavelength oscillation, laser focussing and target generation, absorber/scintillator measurement of plasma X-ray emission, temporally and spectrally resolved infrared light detection, ruby laser interferometry and ruby laser Thomson scattering.

3.2 Lasers

3.2.1 TEA Carbon Dioxide Laser

The principal laser used for the laser-plasma interaction studies was a high power transverse electric atmospheric (TEA) CO₂ laser. This TEA laser was designed and fabricated at the University of Alberta (Burnett and Offenberger [32]). On firing the laser, three single stage Marx voltage doublers supplied 100 kV to the laser discharge electrodes and pre-ionizing pins. The active volume pre-ionization was accomplished through a series of pin discharges located on either side of the main discharge volume and electrically connected in parallel with the Rogowski profiled discharge electrodes. The total charge in the pin discharge arcs was limited with 570 pF series capacitors. Upon firing the laser Marx banks, arcs between the pre-ionizing pins flooded the active volume with photoionizing ultraviolet radiation (Sequin et al.[33]). The resulting O(10⁸ cm³) electron density ensured a uniform electrical discharge between the main discharge electrodes, leading to efficient excitation and inversion of the active medium. Six pairs of opposing graphite and aluminum Rogowski electrodes ballasted the discharge current to further inhibit arcs while delivering electrical energy to the main discharge volume. The total gain length of the TEA CO₂ laser was 3 m and the resonator mirror separation was 4 m. An unstable resonator design permitted 40 J light energy extraction from the laser in a 40 ns FWHM gain switched pulse. Up to 1 GW peak power was delivered in this mode of operation. Table 1 lists the principal features of this CO₂ laser.

The gas kinetics of the CO₂-N₂-He mixture in the laser is well known [34] and will be briefly explained here. Basically, the nitrogen molecule is vibrationally excited through electron impact during the laser current discharge and it couples efficiently to the (00⁰1) state of CO₂ molecules to resonantly transfer its energy and excite carbon dioxide molecular vibrational states. The resultant inverted population of CO₂ molecules (between

Wavelength	10.59 microns
Energy Storage Capacitance	1.2 microfarad
Operating Voltage	55 kV
Preionization	50 x 2 side discharge pins
Active Volume	4.1 l
Active Area	3.7 cm x 3.7 cm
Electrical Efficiency	2.7%
Resonator	4 m unstable
Rear Mirror	12.8 m radius of curvature 5 cm diameter
Output Mirror	-4.96 m radius of curvature 1 cm diameter
Gas Mix (CO ₂ :N ₂ :He)	22:5:73
Laser Light Energy	40 J
Peak Power	1 GW , gain switched 1.7 GW , injection mode locked

Table 3.1 TEA CO₂ Laser Design Features

00°1 and 10°0) amplifies the infrared light and lasing occurs with an optical resonator surrounding the medium. Helium is added to the gas mixture to collisionally de-excite an intermediate CO₂ energy level which would otherwise prevent efficient relaxation of the CO₂ molecule. The helium also increases the thermal transfer to the walls. A helium-rich gas mixture was required to eliminate arcs between the Rogowski profiled electrodes and the reduced carbon dioxide concentration did cause a slight decrease in the total energy extraction. A numerical solution of the rate equations for level populations and photon lifetime for the unstable resonator [35] showed a weak He concentration dependence of the energy extraction in the first 40 ns of the gain switched laser output. Further details of this model will be explained when injection mode locking is discussed in section 3.2.2.

The temporal modulation in the gain switched laser output was different from the simple numerical calculations mentioned above. Strong axial mode beating resulted in an irregular intensity modulation of the laser output as illustrated in Figure 3.1. Figures 3.1(a) and 3.1(b) show two oscilloscope traces where the laser power was monitored with 300 ps resolution and 3.5 ns resolution (for estimating the average laser power). The fast power modulations as seen in Fig. 3.1(a) can complicate some of the laser-plasma interaction experiments and necessitated constant monitoring of the CO₂ laser output power. Figure 3.1(b) shows a limited "nitrogen tail" in the laser output where $\approx 80\%$ of the laser light energy was extracted in the 40 ns gain switched pulse. A power calibration of the laser detector was straightforward from these oscilloscope traces once the total laser energy was known.

The CO₂ laser's positive branch unstable resonator optics were designed for low output beam divergence and good energy extraction from the active volume. Zeroth order calculations from Siegman's equations [36] were used to determine the radii of curvature and mirror sizes for 85% laser output coupling. The calculated values are listed in Table 1. The cavity mode structure was not predicted from these calculations but requires complex calculations based on repeated diffracting aperture calculations [37]. Although these computations were not done here, some useful observations could be made. Firstly, the problem with the zero'th order resonator calculation is that the laser output is presumed to be a uniform annulus. In fact, the transverse modes of the

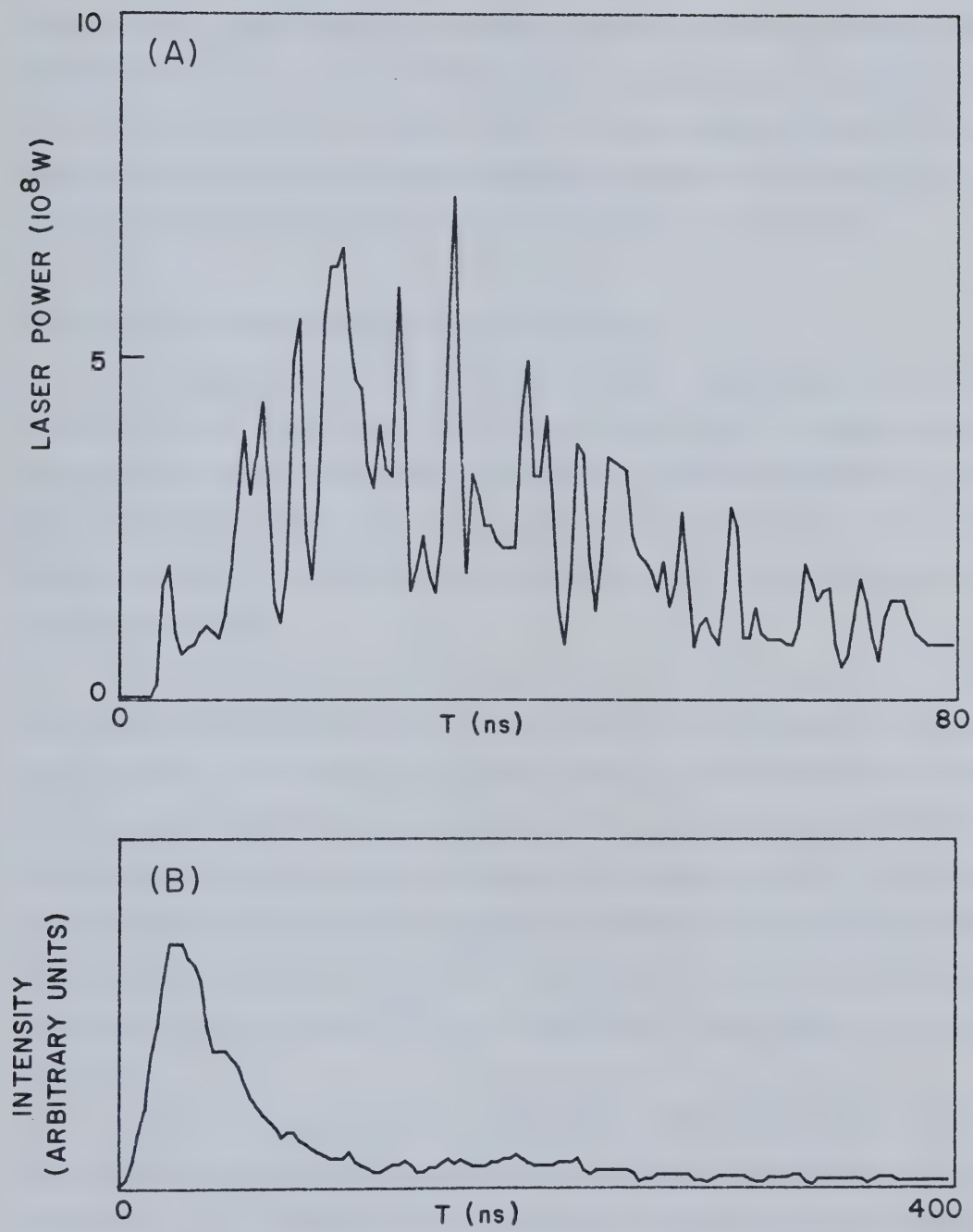


Figure 3.1 Gain Switched CO₂ laser Output

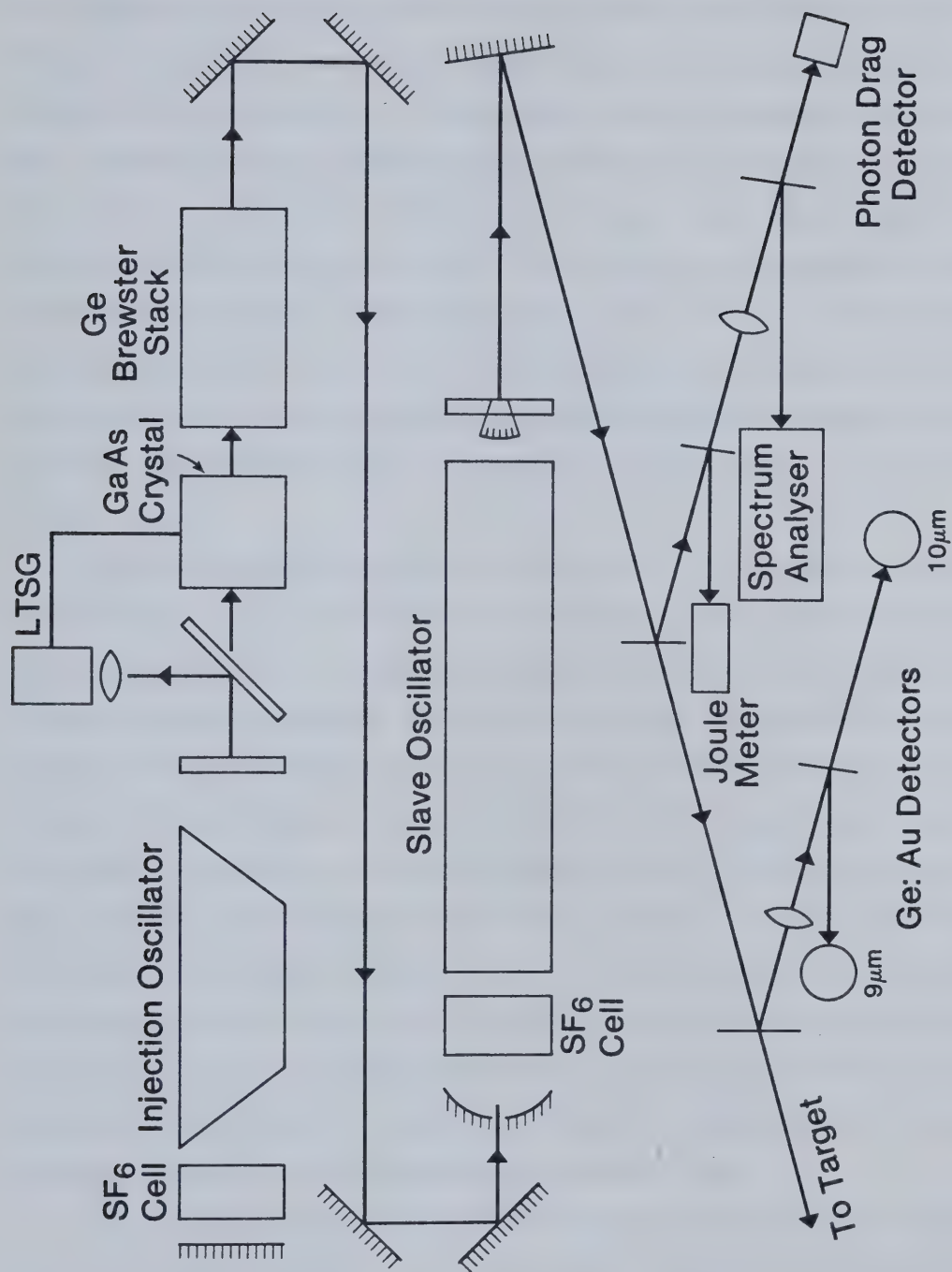
cylindrical resonator are described by generalized Gauss-Laguerre polynomials [38]. Rather than rely upon detailed calculations, these radial intensity modulations in the beam profile were approximated as Gaussian weighted sinusoids whose period was determined through burn paper patterns. These measurements were needed for the focal spot intensity calculations in section 3.3.2. A second important feature of the unstable resonator was the diffraction limited laser beam divergence. This led to higher focussed laser intensities illuminating the gas target in the laser-plasma experiment.

3.2.2 Injection Mode-Locking of the TEA CO₂ Laser

Two modifications of the 4 m TEA CO₂ laser were made in the course of the experimental work. First, the laser was injection mode-locked to produce a train of short duration pulses rather than the usual gain switched lasing. This modification is described here. In the second change which is described in section 3.2.4, the laser was forced to oscillate at several wavelengths simultaneously in either gain switched or injection mode-locked pulses.

Short duration laser pulses were required for their fast intensity rise in the laser-plasma interaction and their high peak intensity as compared to gain switched lasing. Short pulses can be obtained through mode-locking a high power laser or amplifying a low level light pulse. Preliminary experiments with two pass pulse amplification in the 3 m amplifier showed severe parasitic oscillations and made it necessary to use some other pulse generation technique. This was not too surprising as the high gain module was designed for laser oscillation rather than light amplification. Conventional amplifiers normally consist of a series of low gain modules which are isolated to prevent parasitic generation.

Injection mode-locking [39] was selected for producing high intensity pulses from the 4 m TEA CO₂ laser. This mode-locking method was preferred for its ease of operation and did not require modulating high light fluxes with expensive, easily damaged electro-optic components. Figure 3.2 is a schematic of the injection mode-locking system constructed in our laboratory. The two laser oscillators were a 1 m unstable resonator (0.5 m gain length) TEA CO₂ laser injection oscillator with 100 MW peak output power and the slave oscillator, the 4 m TEA CO₂ laser previously described.

Figure 3.2 Injection Mode Locked CO₂ laser

The injection oscillator was a copy of a single section of the slave oscillator but with Brewster angle sodium chloride windows rather than the resonator optics sealing the laser box ends. This was done to produce vertically polarized light from the injection oscillator, making it suitable for pulse slicing in the front-end electro-optic shutter. A laser triggered spark gap (LTSG) provided automatic synchronization of the shutter with the injection oscillator and controlled the light pulse width. Upon firing the injection oscillator, the LTSG generated an ≈ 9 kV, 2 ns charge cable voltage pulse to activate the Chromium doped Gallium Arsenide Pockels cell (7 mm x 7 mm x 40 mm). For the 2 ns, the injection oscillator output was rotated 90 degrees upon traversing the Pockels cell and subsequently analysed by a 3500:1 polarization rejection germanium Brewster stack. Low level unpolarised light from the injection oscillator limited the pulse-to-leakage contrast to 200:1.

The switched out laser pulse was directed into a 2 mm diameter hole drilled into the rear mirror of the slave oscillator and diffraction coupled to the laser mode volume. The timing between the injection and slave oscillators was electronically controlled through two delay generators. Timing jitter of 10–50 ns resulted from shot-to-shot variation in the two oscillators' gain build up but was not critical to achieve mode-locking. The light pulse switched out from the injection oscillator output was injected into the slave cavity at threshold, i.e. before spontaneous emission build up could lead to normal gain switching. The subsequent cavity photon growth is described as regenerative amplification. The injected light pulse grows in the laser cavity and only a fraction of the pulse energy is re-introduced into the cavity after reflection off the output coupler. The resultant laser output is a series of short pulses separated by the slave cavity round trip transit time. The pulse width is approximately that of the injected pulse and the pulse train envelope is similar to the slave oscillator gain switched output.

Table 3.2 summarizes the significant IML system characteristics. As seen in Table 3.2, the IML laser peak power was nearly double that delivered by gain switching. The pulse-to-low level lasing was highly variable and was a function of both injection timing and the injected photon density. Within the 100 ns injection window, the pulse-to-noise contrast was typically better than 20:1. Further improvement in the contrast was accomplished by inserting a low pressure (≈ 4 Torr-cm) sulfur hexafluoride saturable

Injection Oscillator	<ul style="list-style-type: none"> -500 mJ, 40 ns gain switched output -Self synchronized laser triggered sparkgap to GaAs electro-optic modulator
Injection Characteristics	<ul style="list-style-type: none"> - 10 W total power - 50 ns injection jitter - 100 ns injection window - 2 to 3 ns FWHM injection pulse
Slave Oscillator	<ul style="list-style-type: none"> - 0.020 to 0.035 cm⁻¹ gain - Peak power to 1.7 GW - Horizontal Polarization - Pulse contrast better than 20:1

Table 3.2 IML Laser System Performance

absorber cell between the injection and slave oscillators to reduce low level light leakage from the germanium analyser. IML laser prepulse levels were difficult to control due to its sensitivity to injection characteristics. This meant that the CO₂ laser power had to be constantly monitored during laser-plasma experiments. One virtue of this varying output power was that pump intensity scaling of experiments was easily done- a large number of laser shots would provide data points over a large span of pump intensity.

3.2.3 IML Laser Model

A computer model was written to assist in understanding the injection mode-locking and to conveniently study the effects of different operating parameters. The CO₂-N₂-He rate equations used in these computations are similar to Manes et al.[40]. A cell model was used whereby the active medium was partitioned into cells of length ct_p , where c is the speed of light and t_p the injected pulse width. Competition with spontaneous emission was ignored and the slave oscillator resonator mode structure was assumed to be spatially uniform. Consequently, the model did not predict the observed injection window (see for example [41] where a different model is used to obtain this) nor the complex spatial variations in gain saturation throughout the active medium. The injection pulse was introduced R1 round trips after the start of the slave oscillator discharge current and advanced to successive cells each time step. The rate equations for each cell were solved with zero photon density in all cells except where the pulse currently resided. A fraction of the photon density, $1-R$, coupled out of the laser cavity each time the pulse reached the output coupling mirror of reflectivity R . The remaining photons passed through the cavity twice before a second laser pulse was produced. Zero gain cells could also be introduced at either end of the active medium to model the effects of changing the cavity length.

A simplified energy level scheme for the CO₂-N₂ kinetics is given by Andrews et al.[35] and was used here. As seen in Figure 3.3, the nitrogen is excited through electron impact to level N which resonantly transfers to carbon dioxide level n_1 , at rate k . Within the CO₂ energy levels, there is stimulated emission of the laser line from n_1 to n_2 with subsequent decay to ground n_0 through intermediate energy level n_3 . Electron impact also affects the CO₂ n_1 population to some degree. The various rate coefficients used in this

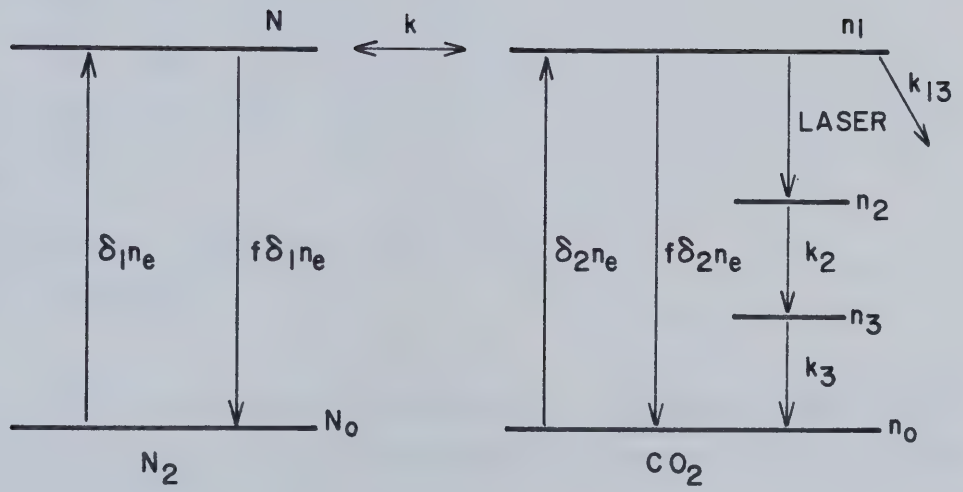


Figure 3.3 Simplified CO_2 - N_2 Energy Level Diagram

model were calculated for the 73:5:22 He:N₂:CO₂ laser gas mixture. The rate and conservation equations used for each cell are:

$$\begin{aligned}
 dn_1/dt &= \delta_1 n_e (n_o - f n_1) + K(N n_o - n_1 N_o) - K_{13} n_1 - \sigma c q (n_1 - n_2) \\
 dN/dt &= \delta_2 n_e (N_o - f N) - K(N n_o - n_1 N_o) \\
 dn_2/dt &= \sigma c q (n_1 - n_2) - K_2 n_2 \\
 dn_3/dt &= K_2 n_2 - K_3 n_3 + K_{13} n_1 \\
 dq/dt &= \sigma c q (n_1 - n_2) \\
 n_o &= N_{CO_2} - n_1 - n_2 - n_3 \\
 N_o &= N_{N_2} - N \\
 n_e &= n_{eo} (4t/\tau)(1 - t/\tau) \quad 0 \leq t \leq \tau \\
 &= 0 \quad \text{otherwise}
 \end{aligned}
 \tag{Eq 3.1}$$

where n_e is the discharge electron density and q the photon density in a cell. N_{CO_2} is the total CO₂ molecule density and similarly N_{N_2} is the total N₂ density. The rate coefficients and cross sections for this laser are:

$$\begin{aligned}
 \delta_1 &= 6 \times 10^{-9} \text{ cm}^3 \text{ s}^{-1} \\
 \delta_2 &= 2 \times 10^{-8} \text{ cm}^3 \text{ s}^{-1} \\
 K &= 5.4 \times 10^{-13} \text{ cm}^3 \text{ s}^{-1} \\
 K_{13} &= (85(\text{He}) + 110(\text{N}_2) + 365(\text{CO}_2))760 = 1.12 \times 10^5 \text{ s}^{-1} \\
 K_2 &= 1.06 \times 10^8 (0.056(\text{He}) + 0.46(\text{N}_2) + (\text{CO}_2)) = 3.07 \times 10^7 \text{ s}^{-1} \\
 K_3 &= 760(4000(\text{He}) + 40(\text{N}_2) + 200(\text{CO}_2)) = 2.25 \times 10^6 \text{ s}^{-1} \\
 \sigma &= 1 \times 10^{-19} \text{ cm}^2 \\
 f &= 1.157
 \end{aligned}$$

(He), (N₂), (CO₂) are the fractional helium, nitrogen and carbon dioxide gas constituents

The laser electrical discharge has been described by Burnett and Offenberger [32] who

measured a 400 ns current pulse. Electron density calculations [42] from their figures indicate peak electron densities in the discharge of $3 \times 10^{13} \text{ cm}^{-3}$.

Equations 3.2 were solved numerically with a second order Runge-Kutta integration and the principal conclusions from the modelling are as follows. There is only an extremely weak dependence of the peak IML laser output power on injected photon density and timing. This was tested with six, 2 ns gain cells comprising the laser and energy from 10^{-12} to 10^{-6} J injected into the slave oscillator at 1 to 18 round trip times after the start of the laser discharge current pulse. Spontaneous emission was not incorporated in the model since the injection window is not as large as these results indicate. Lowered output coupler reflectivity reduced the cavity feedback and moved the peak pulses into higher gain above threshold. The outcome was higher peak powers in the IML laser pulses with lower coupler reflectivities. A larger resonator gave the same effect, with an 8 m cavity giving $\approx 40\%$ higher peak powers than for 4 m resonators with the same active medium length. This behaviour has been experimentally observed in other laboratories [41]. Another very important effect clearly demonstrated in the model was the dependence of the peak pulsed power in the injected pulse width. The energy per pulse remained approximately invariant to the pulse width, resulting in decreased peak powers for increased pulse width. This effect was very noticeable in the laser operation where poor electro-optic gating of the injection oscillator output reduced the peak intensities by factors of two and more. This made it essential to pay close attention to the alignment of the laser triggered spark gap and electro-optic shutter.

The model predictions compared well with the initial pulses of the observed IML laser output. A model result and two measured laser pulse trains are depicted in Figure 3.4. After the first few pulses, the model does not closely resemble the actual IML laser output. After gain depletion from the first four or five laser pulses, the oscillator gain falls below threshold and the spontaneous emission competes with the IML lasing in the nitrogen tail. Consequently, the nitrogen tail was reduced to a weakly modulated pulse train as significant low level lasing decreased the gain available to the IML laser pulses. Figure 3.4(c) shows how SBS fed back into the slave oscillator caused double pulsing in the nitrogen tail of the laser output to further limit the late time peak powers.

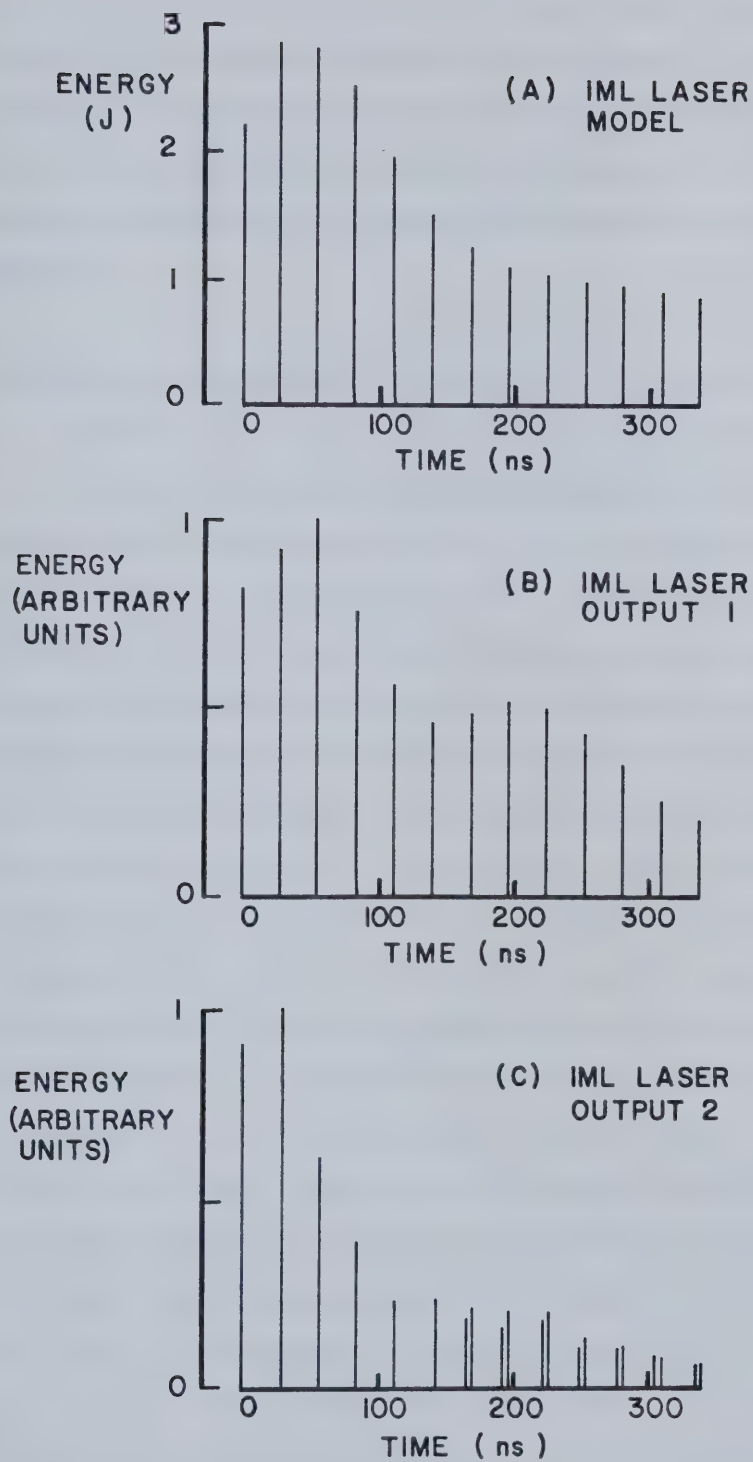


Figure 3.4 Comparison of IML Laser Model to Experimental Results

The utility of the IML laser model came in identifying the parametric response of the IML laser to injection timing and density, resonator coupling and length and injected pulse width. These results revealed the important features to attend to in operating the lasers. Since only the first high power pulse was important in the laser-plasma experiments, the late time deviations of the model from the real laser performance were ignored.

3.2.4 Multiwavelength Oscillation of the TEA CO₂ Lasers

The CO₂ laser operation described above has been for single line extraction, that is, of all the available carbon dioxide lasing transitions, only the P20, 10.59 micron line was produced. This was simply a result of P20 having the highest gain and therefore the fastest buildup to gain switching. Upon gain switching, the CO₂ rotational levels re-thermalize in ≈ 0.2 ns and thus gain depletion occurs for all the possible transitions as energy is extracted by the dominant P20 line. Single wavelength oscillation is not always desirable. With extremely short laser pulse generation, the thermalization time can be too long for effective energy extraction from the active medium. Secondly, in a CO₂ laser-plasma experiment, a multiwavelength laser can reduce stimulated Brillouin scattering as was demonstrated in this research. It was also of scientific interest to demonstrate that it was possible to obtain multiline injection mode-locking of a high power CO₂ laser. This section will describe the criteria that need to be satisfied to obtain multiwavelength laser oscillation and how it is accomplished.

Two methods have been used in conventional gain switched TEA CO₂ lasers to obtain multiline lasing. Cavity etalon tuning provides line selection and can preferentially detune P20 to allow other transitions to lase [43]. The second and more common method is to install intracavity absorption cells which selectively absorb the P20 line and inhibit it from lasing. Our choice was absorption cells with sulphur hexafluoride (SF₆) absorption gas. SF₆ has strong absorption at 10.6 microns as compared to other CO₂ laser transitions and, as a saturable absorber, it conveniently bleaches at laser gain switching to minimize laser absorption losses and maximize extracted laser power. Figure 3.2 illustrates the 7 cm aperture SF₆ cells installed in both the injection and slave oscillators. Whether operated in a gain switched or IML output, the slave oscillator could be

operated multiline. By simultaneously tuning the injection and slave oscillators to lase on common lines, multiline IML lasing was obtained. This is believed to be the first demonstration of multiwavelength injection mode-locking of a high power TEA CO₂ laser.

Multiline oscillation of the slave oscillator occurs through the simultaneous growth of several laser lines which have close to the same gain and consequently gain switch at the same time. For the simplified case of a pulsed laser with a linear gain increase from zero to $\bar{\alpha}$ cm⁻¹ (averaged over cavity) in time τ , the gain switch time T for an injected (or spontaneous emission) photon density ϕ_j cm⁻³ is [44]:

$$T = \tau \ln M / \bar{\alpha} L + \sqrt{[2\tau \ln(\phi_s / \phi_j) / c\bar{\alpha}]} \quad \text{Eq. 3.2}$$

where M is the resonator magnification, ϕ_s is the saturation photon density ($\phi_s = 2 \times 10^{16}$ cm⁻³) and L is the cavity length. The first term of this equation is the time to reach threshold from the beginning of the laser gain and the second term is the time to achieve gain switching from threshold. To induce two laser lines in the oscillator output, their gain switched times must be approximately equal to ensure that gain depletion from one line does not inhibit the second line. This condition applies equally well to gain switched and IML lasers. For two lines j and k to successfully participate in lasing then:

$$|T_j - T_k| \leq \text{cavity transit time}$$

Inspection of Equation 3.2 for T shows the main controlling factors in obtaining multiwavelength oscillation. First, T is only logarithmically dependent on the spontaneous or injected photon density ϕ_j . For example, with the CO₂ laser parameters in Table 1 and a gain of 0.025 cm⁻¹, if 10 W of power is injected at one wavelength, a second injected line with 4–30 W would satisfy the gain depletion criteria and still lase. Injected energies over six orders of magnitude (10⁻¹² to 10⁻⁶ J) were tested in the IML laser program and the gain switch time did not change over more than ± 120 ns. This time range is greater than what was acceptable for simultaneous gain switching but does illustrate the validity of approximation in Equation 3.2.

The second observation is the direct dependence T has on $\bar{\alpha}$ —small changes in the laser gain for any laser transition could drastically alter its gain switch time. Since $\bar{\alpha}$ depends on both the absorption cell losses and the laser gain, their adjustment is very critical to obtain multiwavelength lasing. The gain buildup time T is only dependent on the electrical discharge pumping of the active medium and is the same for all laser transitions. Overall, T was approximately 600 ns to 1000 ns within the normal laser operating conditions. This range was much greater than the permissible ± 14 ns difference in gain switching for two laser wavelengths. However, control of $\bar{\alpha}$ through the SF_6 absorption cell enables T for several laser lines to be roughly equal.

Obtaining multiwavelength oscillation from the gain switched CO_2 laser was straightforward. The intracavity absorption cell was filled with 2–250 Torr-cm of SF_6 and helium buffered to atmospheric pressure. As a result, upon lasing, the 10.59 micron P20 line was eliminated and lasing on 2 to 5 lines in the 10.3 micron or 9 micron bands took place. The output energy was reduced from the single line output by approximately 50% to 17 J because of cell absorption losses and reflection losses from the sodium chloride windows. An Optical Engineering CO_2 laser spectrum analyser was used to detect the various lines in the laser output. The laser energy distribution in these lines was determined with an infrared multichannel analyser located behind a 0.5 m infrared grating spectrograph (see section 3.4).

Injection mode-locking on several lines was achieved through tuning the injection oscillator with its absorption cell and those lines common to the two oscillators were in the IML laser pulse train. Table 3.3 gives those combinations of equal power lines which were obtained for various amount of intracavity SF_6 . The wavelength content was highly sensitive to the laser gain and SF_6 pressure as expected from Equation 3.2. Drift was observed in the output line content as either characteristic changed during laser operation and thus the spectrum had to be monitored continuously.

As with the gain switched laser, the IML laser performance was reduced in multiline operation. Peak total multiline powers of 390 MW were observed with approximately equal power in the participating lines (up to three lines). The power contrast of the laser pulses to the low level lasing between pulses was $\approx 9:1$. This was significantly poorer than the 20:1 contrast in the single line, 10.59 micron lasing because

INTRACAVITY SF ₆		LINES
0	Torr cm	P ₁₀ (20)
<5	Torr cm	R ₁₀ (26)
		R ₁₀ (10), R ₁₀ (14)
		R ₁₀ (18), R ₁₀ (20)
		R ₉ (14), R ₁₀ (18), R ₁₀ (26)
		R ₉ (14), R ₁₀ (16), R ₁₀ (18)
		R ₉ (14), R ₉ (16)
5-25	Torr cm	R ₉ (14)
		R ₉ (14), R ₉ (16)
		R ₉ (14), R ₉ (16), R ₉ (18)
250	Torr cm	P ₉ (18), P ₉ (22), R ₉ (12)

Table 3.3 Some Line Combinations in a Multiwavelength IML Laser

a saturable absorber was not available to uniformly eliminate light leakage from the electro-optic switch at the injection wavelengths and obtain a high quality injection pulse. The total extracted energy in the IML pulse train was ≈ 15 J with approximately 50% of the energy residing in the laser pulses and the balance in low level lasing. Only horizontal output polarization was obtained with the multiline IML laser. The birefringent mylar used with the single line IML laser to obtain random polarization was a narrow 10.6 micron bandpass filter and therefore could not be installed at the injection aperture of the slave oscillator for multiwavelength injection.

Multiline operation of both the gain switched and injection mode-locked oscillators was valuable in experimentally confirming the pump dependence in stimulated Brillouin scattering. The details of this experiment will be given in Chapter 4.

3.3 Target Chamber

The principal experimental equipment consisted of the TEA CO₂ laser system and experimental target chamber into which the laser beam was directed and then focussed onto the gas jet target. The target chamber was a 70 cm diameter by 35 cm high aluminum cylinder with eight optical/general purpose ports around its perimeter. A 5 cm thick plexiglass plate on top of the chamber was removeable to permit access to the gas target, focussing mirror and diagnostic instrumentation. Electrical connections, gas and vacuum lines were provided through suitable ports and feed-throughs on the bottom plate of the chamber cylinder. The gas jet target was centrally located in the target chamber and a gold coated 10 cm focal length parabolic concave mirror was located to intercept the incoming CO₂ laser beam and focus it onto the gas jet. Details of the target jet and focussing mirror are given later.

The interior layout of the target chamber and the position of its ports are shown schematically in Figure 3.5. The main optical access windows used were ports 2, 3 and 7. The CO₂ laser light was directed through the 7.5 cm diameter sodium chloride etalon at port 2 which also provided a reflected light signal for CO₂ laser power, energy and spectral content monitoring. Stimulated Brillouin backscattering also exited from the target chamber through this port. Ports 3 and 7 were used extensively for Ruby laser Thomson scattering and interferometry.

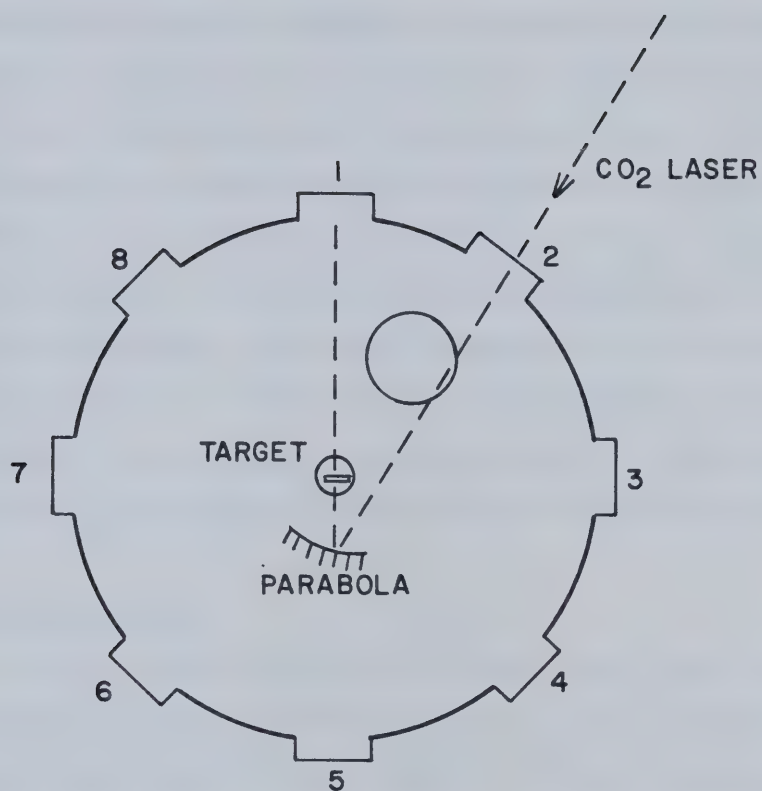


Figure 3.5 Top View of the Target Chamber

In operation, the target chamber was evacuated to ≈ 0.01 Torr with a dual stage mechanical vacuum pump and then backfilled with 10 Torr of helium (except in special cases) for stabilizing the gas flow in the target jet. The gas target reservoir was simultaneously re-pressurized to 2000 Torr of oxygen at the time of helium backfilling. This target chamber preparation sequence was automated through a specially designed microprocessor controller which was activated immediately after CO₂ laser firing. The evacuation and gas filling solenoid valves were operated by the controller and solid state pressure transducers for monitoring the gas pressures were interfaced to it through standard analog-to-digital converters. The controller software was designed to allow control system recovery from noise interference generated by the TEA CO₂ lasers as well as electrical discharges from other experiments. After the gas jet target was produced and the TEA CO₂ lasers fired, the target chamber preparation cycle was repeated. A 45 s experiment cycle time was possible with this arrangement although longer times were often required for data recording or experimental modifications.

3.3.1 Oxygen Gas Jet Target

The focussing mirror and gas jet assembly were located inside the target chamber. The gas jet assembly provided a supersonic laminar oxygen gas jet which was irradiated with high intensity CO₂ laser radiation. The laser ionized gas provided the medium in which the laser-plasma interaction took place. The construction of the gas jet is illustrated in Figure 3.6. In operation, the refill solenoid opened to allow filling the gas reservoir to 2000 Torr oxygen and then closed. Upon triggering the gas target, the dual solenoid valve was opened for 500 ms and the laminar jet was formed. A piezoelectric pressure transducer detected the gas pressure pulse below the jet orifice and gave a timing signal for instrumentation in the screen room and for synchronizing the laser firing with the gas jet generation.

The expansion orifice of the target jet was designed as a supersonic nozzle. Gas flow became sonic at the throat and subsequently supersonic upon expansion into the 10 Torr Helium environment. Gas parameters at the nozzle were 58 Torr pressure, 5×10^{18} cm⁻³ particle density and 500 m s⁻¹ flow speed. Shadowgraphy was used to observe the gas jet boundaries for different helium gas fill pressures to compare profiles with its

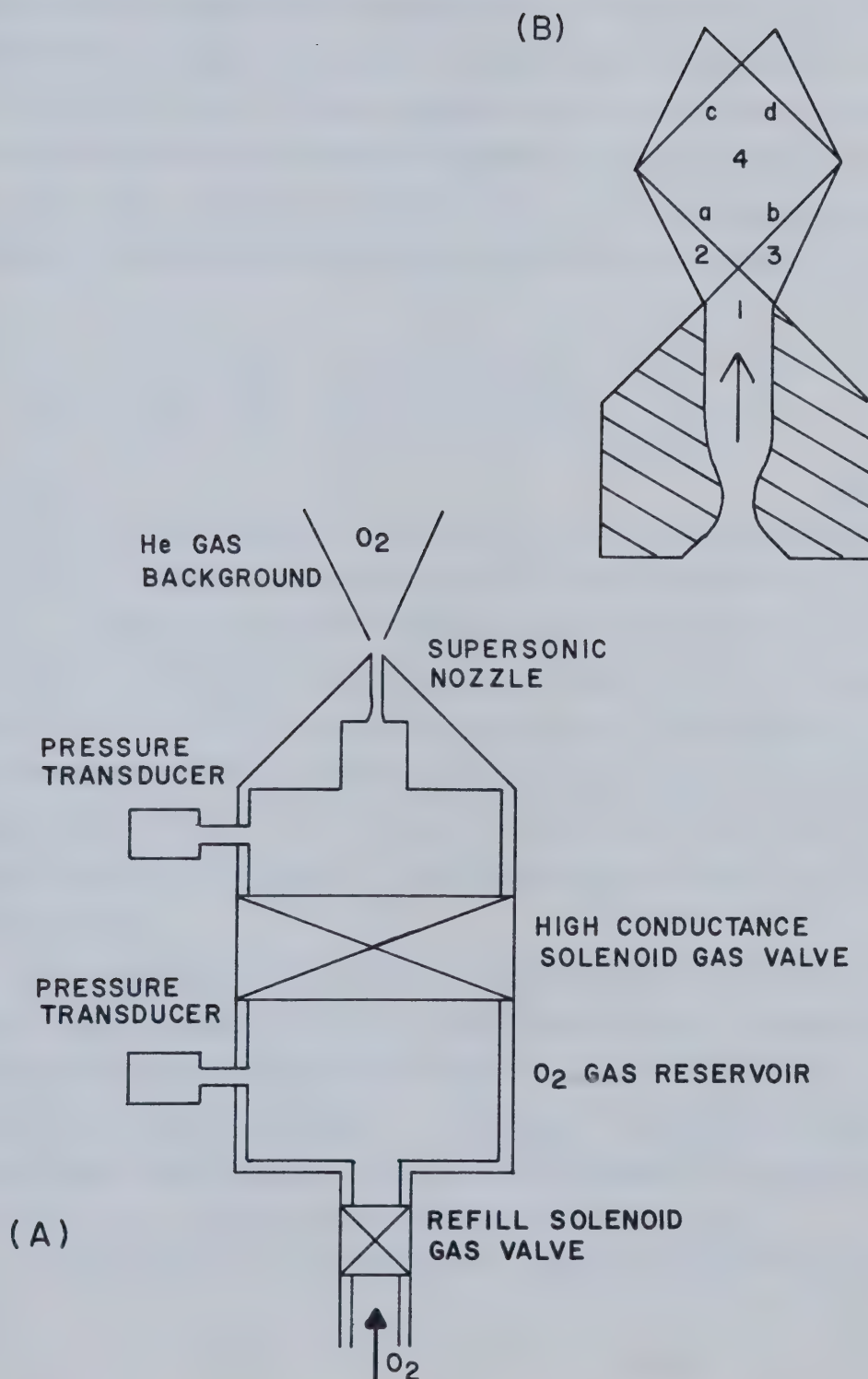


Figure 3.6 Gas Target Design

calculated behaviour. The gas flow exhausted into low ambient helium pressure.

Under these conditions, an underexpanded jet formed over the supersonic nozzle and the potential equation for compressible flow was solved through the method of characteristics to obtain flow parameters in the jet (Shapiro [45]). Isentropic calculations were used and the region of validity extended above the jet only until frictional forces between the ambient gas and jet became significant. Figure 3.6(b) will assist in explaining the method used in the free jet calculations. First, in region 1, the gas is just leaving the nozzle, with a Mach number calculated from the isentropic flow relation:

$$A/A_T = \frac{1}{M} \left[\frac{2}{\gamma + 1} \left(1 + \frac{\gamma - 1}{2} M^2 \right) \right]^{\frac{\gamma + 1}{2(\gamma - 1)}}$$

where A_T

is the nozzle throat dimension (flow is sonic at the throat) and M is the Mach number at any position of dimension A downstream from the throat. The ratio of specific heats is

γ which is 1.4 for diatomic molecules. Once the Mach number at the nozzle exit is calculated, all other gas parameters such as pressure, density and temperature are calculated through the various isentropic flow equations. The gas outside the nozzle is freely expanding and the jet boundary conditions are determined from the static gas fill. In Figure 3.6(b), the gas flow boundaries are shown with the streamline directions changing each time a rarefaction or compression wave is crossed. Lines a and b are rarefaction waves.

More detailed calculations reveal that these waves (they are the characteristics of the flow potential equations) are actually Prandtl Meyer fans with a continuous change in streamline flow direction across them. The Mach numbers in regions 2 and 3 are easily found as their pressure must equal P_{ambient} (no pressure difference across a free boundary). Once the Mach number of these two regions is found, then the angle of the free boundary can be calculated from the Prandtl-Meyer equation:

$$\omega(M) = A \tan(\sqrt{M^2 - 1}) - \sqrt{(\gamma + 1)/(\gamma - 1)} A \tan \sqrt{(\gamma - 1)(M^2 - 1)/(\gamma + 1)}$$

Eq. 3.4

and $\theta_3 = \omega(M_1) - \omega(M_3)$ where θ_3 is the streamline direction in region

3 with respect to the jet axis. The rarefaction waves are lines across which gas conditions change. The angle these waves make to the average flow direction (eg $(\theta_2 + \theta_4)/2$ across a) is the average of α for the two regions separated by the particular line

$$\alpha = \text{Atan}[(M^2 - 1)^{-1}] \quad \text{Eq. 3.5}$$

From these equations it is possible to follow the flow-parameters through the free jet as rarefaction and compression waves are crossed. Once the change in flow direction is calculated, the Prandtl-Meyer equations can be used to calculate the Mach number in the new region (region 4). The calculations are simplified by recognizing the jet symmetry and replacing the center streamline with a solid boundary. A program listing of the calculation method is given in Appendix B.

Two cases of p_O and p_{He} are calculated as above and shown in Figure 3.7. where p_O is the O_2 jet stagnation pressure and p_{He} is the ambient helium pressure. The measured throat dimension was 113 microns and the nozzle exit was 460 microns. In Figure 3.7 the density n/n_c is indicated inside each flow field where, n is the electron density if the oxygen in the jet is ionized to $Z=6$ and n_c is the critical density for the 10.59 micron CO_2 laser wavelength. Two features are seen in these results. First, there is a high density sheath around a low density region and finally a high density core of variable extent, depending upon the pressure ratio. Secondly, the CO_2 laser focus was set up such that the lowest density region was not necessarily accessed. The density sampled in the $p_O = 2000$ Torr, $p_{He} = 10$ Torr calculation would provide $0.78 n_c$ and 500 microns further into the plasma it would rarify to $0.29 n_c$. The important conclusion is that there really is an optimum focal position for the CO_2 laser in the neutral jet and it must be carefully selected.

Shadowgraphic measurements of the neutral gas flow boundary compared well with the above calculations. A pulsed ruby laser light source was used to illuminate the neutral gas target for these results. The dashed line in Figure 3.7 for the 10 Torr background helium is the observed oxygen jet boundary. The comparison of the

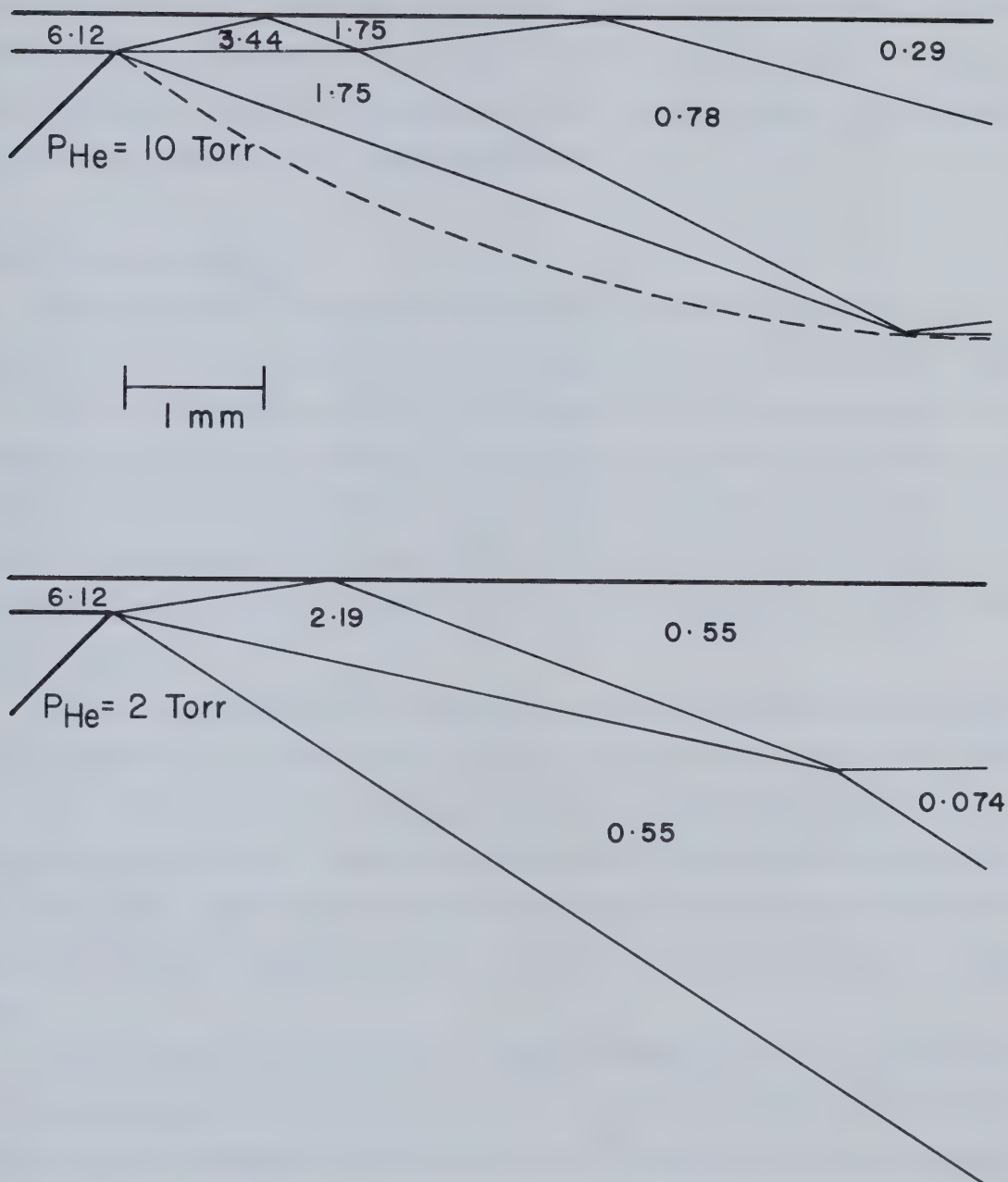


Figure 3.7 n/n_c in the Oxygen Jet Flow

theoretical and experimental results is excellent although it must be remembered that shadowgraphy does not measure the absolute gas density. Interferometry measurements of the oxygen density were not made because of the limited extent of the low refractive index neutral gas. At least the theoretical calculation is a useful guide to the expected oxygen densities under different operating conditions.

3.3.2 CO₂ Laser Focussing

The TEA CO₂ laser and gas target performance have been treated in the previous sections. The remaining principal component to be described is the parabolic mirror used to focus the incoming CO₂ laser light onto the gas jet. The mirror consisted on an aluminum substrate coated with copper and gold overcoated for high reflectivity, high damage threshold and tarnish resistance. Mirror fabrication was done in the department's optics shop as described by Arnold and Offenberger [46]. The mirror was mounted on a moveable, tiltable carriage so that the mirror focus could be adjusted to anywhere within the neutral gas jet.

The off-axis parabolic mirror focussing of the CO₂ laser light was modelled to assist in determining the focussed laser intensities. Because of mirror aberrations, CO₂ laser beam divergence and laser beam mode structure, the intensity distribution was difficult to measure directly. Also, measurements from a Helium-Neon alignment laser could only give a limited estimate of the mirror focussing characteristics because its divergence and mode structure were very different from those of the actual CO₂ laser beam.

The calculation approach is shown in Figure 3.8. Meridional rays are incident upon a reflecting surface $y=f(x)$ whose radius of curvature is $r = R(x)$. The radius of curvature could be calculated from the shape of the parabola but since it is calculated with a second derivative of $f(x)$, it is extremely sensitive to errors in f . Thus the radius of curvature of the parabola was directly measured in a Ronchii test. The incoming CO₂ beam is incident at an angle δ to the parabola's axis and is intercepted by the parabola's reflecting surface. Ray tracing was done by approximating the reflected light beam as a bundle of rays. The center ray θ_c was traced and the distance F along its reflection was used to define the origin of a new coordinate system (\hat{x}', \hat{y}') whose

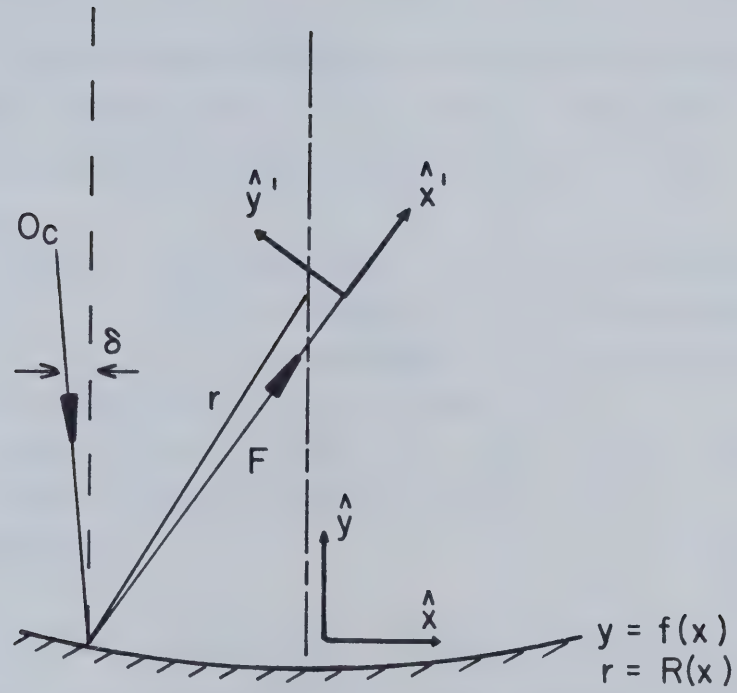


Figure 3.8 Meridional Ray Tracing of the CO₂ Laser Focus

\hat{x}' axis was parallel to the reflected ray. All other rays of the CO₂ laser beam were traced and their \hat{y}' intercepts calculated. By weighting the rays with the CO₂ unstable resonator intensity distribution, the intensity profile along the \hat{y}' axis was easily calculated for any position along \hat{x}' . A further refinement included laser beam divergence. Divergence was introduced in the modelling by dividing each ray into several equal angle spaced subrays which were then traced. These equal intensity subrays spanned the range of incident angles resulting from the laser beam divergence.

The measured functions $f(x)$, $R(x)$ and $W(x)$ where $W(x)$ was the laser intensity weighting function were:

$$f(x) = \sum_{i=1}^6 a_i x^i \quad \begin{array}{ll} a_1 = -0.023095 & a_4 = -0.00959025 \\ a_2 = -0.0939695 & a_5 = -0.001734167 \\ a_3 = -0.024770834 & a_6 = -0.00011277778 \end{array}$$

$$R(x) = 19.4 + 0.07547 x \quad 0 \leq x < 2.65$$

$$= 19.0421 + 0.2105 x \quad 2.65 \leq x \leq 3.6$$

$$= 19.4727 + 0.0909 x \quad 3.6 \leq x \leq 5.8$$

$$W(x) = \sin^2(4\pi x/3.7)$$

The 0.3 mrad CO₂ laser beam divergence was calculated as the diffraction limit of the unstable resonator's annular aperture [23]. Further, focussing diffraction was accommodated by selecting a grid dimension close to the mirror's diffraction limit. The diffraction limit in the f/3 focussing was approximately 30 microns and so a 20 micron grid size was selected. A finer grid would have generated nonphysical high frequency spatial intensity modulation in the focal region.

Figure 3.9 shows the calculated intensity profile through the focal region of the parabolic mirror with the above parameters. Sixty to seventy per cent of the incident laser power is within a 100 micron diameter spot in an 800 micron waist. This long waist is a result of the mirror aberration and as a consequence, a uniform laser intensity illuminates the plasma region of interest during the laser-plasma interaction (at least until severe plasma refraction takes place). At the peak intensity (axial position 0 microns in Figure 3.9), the beam FWHM is 60 microns although at this axial position, a significant fraction of the incident power is off axis by 150 microns.

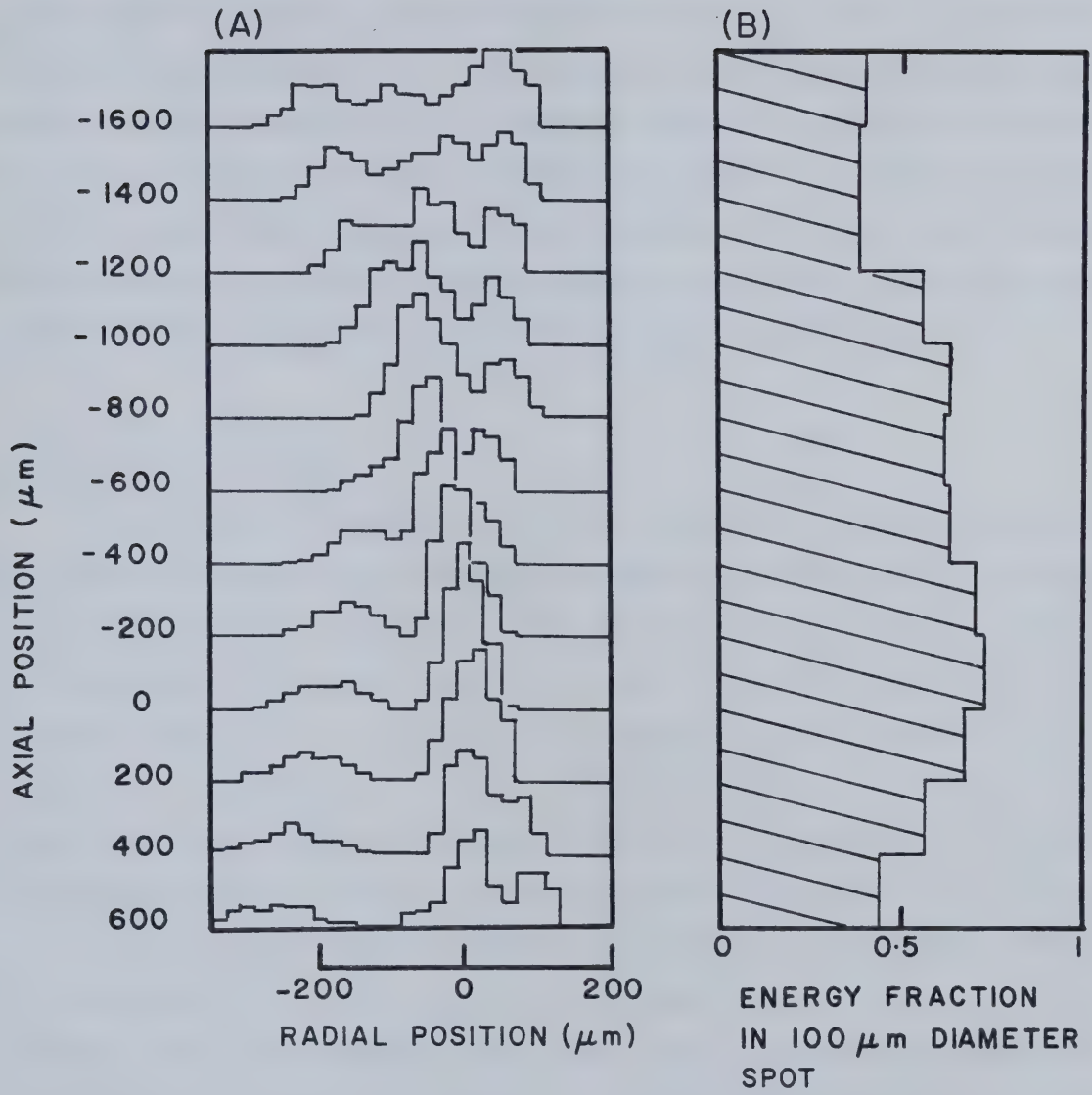


Figure 3.9 Off Axis Parabola Focus

It is important to consider how the CO₂ laser focus was aligned over the gas jet orifice. An alignment Helium–Neon laser for the unstable resonator optics was focussed onto a 200 micron diameter microball suspended above the jet orifice. The mirror focus was adjusted for maximum occlusion of the He–Ne laser light from the microball. Similar focussing model calculations for the He–Ne laser showed maximum occlusion within 200 microns of the CO₂ laser focus which is acceptable positioning accuracy for a long beam waist. Even for this case in calculating the CO₂ focus position and intensity distribution, once the oxygen target is ionized, refraction and absorption alter the light intensity distribution. However, it is still important to estimate the focussing properties of the optical system for laser pump calculations in the laser–plasma interaction.

3.4 Infrared Light Detection

Several kinds of infrared light sensitive instruments were used to monitor the TEA CO₂ laser performance and light scattered in the laser–plasma interaction. Four detectors were available for time resolved measurements of the infrared light. First, low sensitivity doped germanium photon drag detectors were used as monitors for the incident and transmitted light from the plasma. Typical responsivity and risetime were 0.5 $\mu\text{V/W}$ into 50 Ω and < 1 ns respectively. The observed risetimes were slower due to amplifier, cable and oscilloscope risetimes so that ≈ 2.4 ns signal risetimes were normal. Type 7834 Tektronix storage oscilloscopes with 7A19, 50 Ω vertical amplifiers (400 MHz bandwidth) were the principal oscilloscopes used for all measurements. Two other detectors were liquid nitrogen cooled, gold doped germanium (Ge:Au) photodetectors which were used in applications requiring high infrared light sensitivity (0.2 V/W into 50 Ω) and medium bandwidth (1 ns intrinsic risetime). Various bandpass, cut-on and cut-off infrared interference filters were used in front of these detectors during multiwavelength laser experiments. Finally, high speed infrared light monitoring was done with 100 ps risetime pyroelectric detectors (5 $\mu\text{V/W}$ into 50 Ω) connected directly with 1.5 m of coaxial cable to a type 7104 Tektronix oscilloscope with a 7A29 vertical amplifier. The risetime with this combination was better than 360 ps.

Time integrated infrared light measurements were done either with a pyroelectric joulemeter for routine laser energy monitoring or with an infrared multichannel analyser (IRMA). The IRMA was a PARC type 1204A pyroelectric vidicon with a 10 mm x 10 mm scanned area and 33 micron effective channel width. The IRMA controller had an output line to synchronize scanning with the CO₂ laser firing. Accumulated data were displayed on both a numerical readout and on an oscilloscope. Spectrally resolved backscattered light measurements were made by positioning the IRMA head behind a 0.5 m infrared grating spectrograph with a suitable imaging arrangement. Either a 75 lines/mm, 64 x 64 mm, 8 micron blazed grating or a 148 lines/mm, 5 micron blazed grating were installed in the spectrograph. The lower resolution grating yielded 3.2 Å/chn dispersion on the IRMA with 35 Å resolution and the high resolution grating was approximately twice as dispersive with twice the resolution, as expected. The low resolution grating was normally used to provide a large scanning range and higher grating efficiency.

The limited resolution in spectral measurements was improved through deconvolution of the instrumental slit function from the data points. To accomplish this, the spectral data points were first convolved with the measured spectrograph slit function. In the first iteration the changes in the data point values are the correction to the original data. Several iterations of this calculation procedure were done by the "pseudodeconvolution" method [47]. This approach was superior to direct single pass matrix inversion to remove the instrumental response because of its low noise sensitivity and avoidance of troublesome computational round off errors. The calculation algorithm is given in Appendix A. All spectral data in this thesis, including visible light spectra, has had the instrumental function deconvolved. A test of the method was done by deconvolving an instrumental function from itself. Ideally, the solution should converge to a single point. In fact the test resulted in a four times improvement of the spectral resolution. This was considered very satisfactory performance and justified its routine application to spectral data.

3.5 Plasma Electron Temperature Measurement

The infrared detectors described above provided information on the CO₂ laser light and light backscattered from the laser-plasma interaction. To complete the characterization of the interaction, the plasma electron temperature, T_e , electron density n_e and electron density gradient ∇n_e were determined. The electron temperature measurement is described here.

Once the oxygen plasma was created through photoionization and cascade ionization in the gas jet target, the high temperature plasma emitted bremsstrahlung and line radiation in all directions. The X-ray spectra of this emitted radiation was monitored through a very simple thin absorbing foil/scintillator arrangement from which the plasma electron temperature was calculated. A detection head consisting of a 5 mm aperture drilled in a shielding aluminum housing was located approximately 4 cm away from the plasma. Various thicknesses (1.75 – 12 micron) of aluminum foil were placed in this aperture, behind which was located an NE102A plastic scintillator. The blue light scintillations from the NE102A material were coupled to an RCA 8645 photomultiplier through a low loss 6 mm x 30 cm flexible fiber optic bundle. The calculated response time of this arrangement including oscilloscope, cabling and amplifiers was 3.7 ns (1500 V on photomultiplier). The relative photomultiplier signal as a function of aluminum foil thickness was compared to theoretical calculations for a Maxwellian electron distribution in an oxygen plasma [48] to provide electron temperature estimates. In all cases, the electron temperature was much less than 1 keV.

3.6 Plasma Electron Density Measurements

The plasma electron density was measured through ruby laser interferometry. The diagnostic method provided a 400 ps exposure single frame interferogram whose fringe deviations were Abel transform inverted to calculate the radial and axial electron density distribution. Figure 3.10 shows the interferometer in place for the laser-plasma experiment. A pulsed ruby laser light source illuminated the plasma and the Fresnel mirrors were slightly angled to each other to produce fringes. This arrangement was essentially a Fresnel mirror division of wavefront interferometer with a telescope to image the plasma region in front of the recording camera lens. This interferometer was

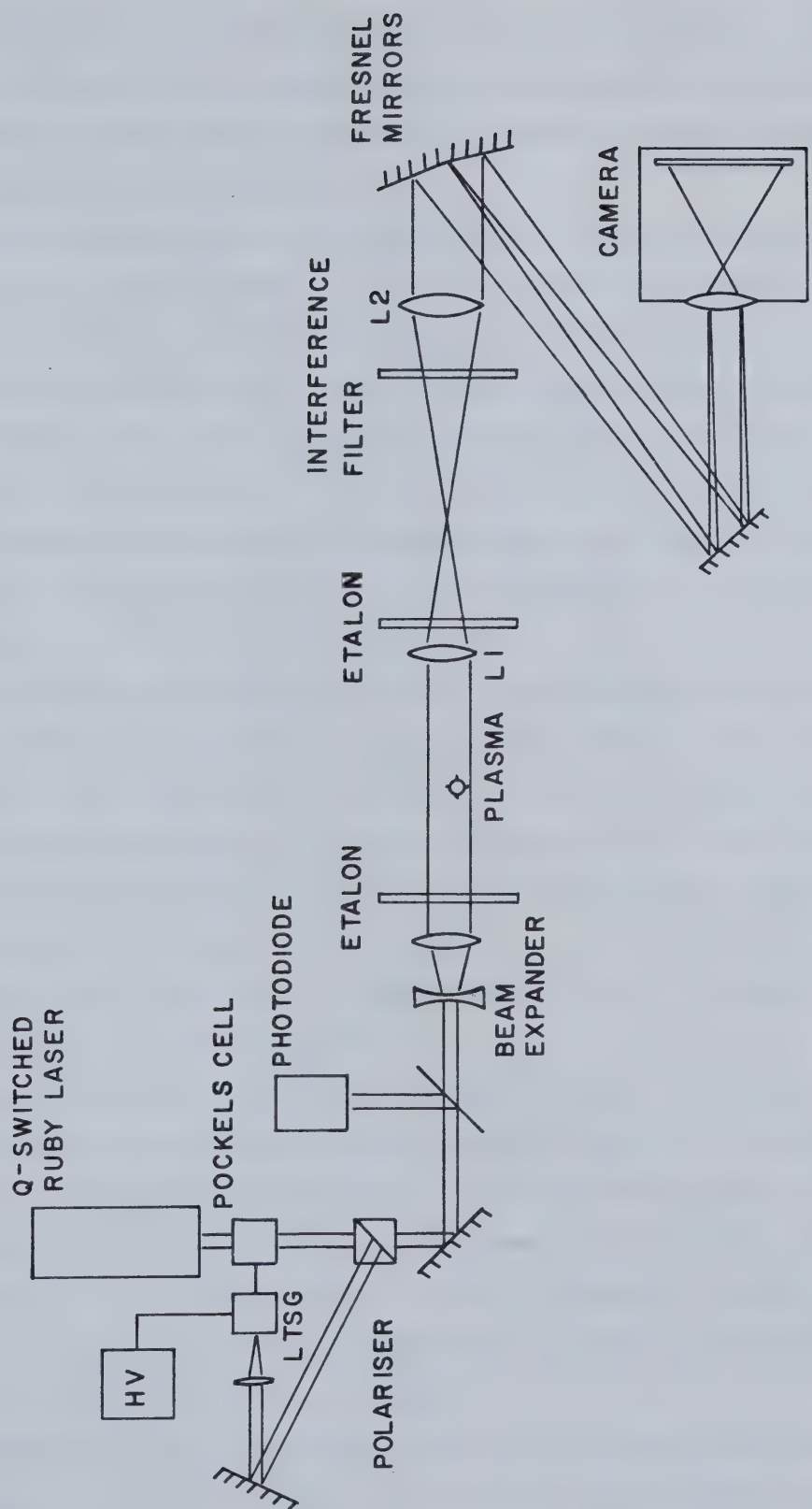


Figure 3.10 Ruby Laser Interferometer

selected because the optical paths of the reference and test sections were nearly coincident, allowing simple beam handling. Also, maximum fringe brightness was achieved as compared to the 50% intensity reduction with division of amplitude interferometers such as the Mach-Zender interferometer.

The interferometer light source was a Korad K1Q ruby laser which produced 20 ns FWHM, 200 mJ pulses of 6943 Å light. An optical shutter consisting of crossed Glan-Thomson polarizers, a KD*P Pockels cell and a laser triggered spark gap, sliced a 400 ps pulse from the ruby laser output. The laser triggered spark gap voltage and optical alignment were critical in achieving maximum energy and contrast in the pulse. Full wave voltage was applied to the KD*P cell in a fast rising step from the spark gap so shutter transmission occurred only on the leading edge as the Pockels voltage passed through its half wave voltage. The shutter output was expanded with a convex/concave lens telescope and directed into the target chamber so that one half of the beam intercepted the plasma region and the other half was an unperturbed reference beam. A two-lens telescope then directed the ruby laser light onto the Fresnel mirrors and localized the fringes at the plasma. An interference filter in the telescope cut out the plasma bremsstrahlung emission. The optical configuration of the interferometer was designed to optimize film exposure, image magnification on the film and fringe resolution. Typical figures for this setup were 1 $\mu\text{J}/\text{cm}^2$ energy onto the film, 50x magnification and 25–50 micron fringe separation. More information on the interferometer design is given in Appendix C.

The ruby laser was electronically synchronized to the TEA CO₂ laser firing with approximately 20 ns jitter. The main contribution to jitter was in the CO₂ laser gain switch time. Timing of the interferometer exposure to the plasma formation was done through simultaneous monitoring of the 400 ps ruby pulse on a high speed Optics Technology photodiode and infrared backscattered light on a pyroelectric detector. In most experiments the ruby laser was timed to illuminate the plasma during stimulated Brillouin scattering from the CO₂ laser – plasma interaction.

Interferograms from this diagnostic method were photographically enlarged and then digitized on a Hewlett Packard microcomputer. Data smoothing and an Abel transform technique were used to unfold the refractive index distribution through the

plasma. The refractive index formula $\mu^2 = 1 - ne^2/\epsilon_0 m_e \omega_r^2$, where μ is the refractive index and ω_r is the ruby laser frequency, was used to convert the refractive index to electron density. The computational algorithm for the Abel transform is given in Appendix A.

3.7 Ruby Laser Thomson Scattering

Aside from infrared light measurements, ruby laser Thomson scattering [49] provided the most versatile diagnostic method for probing the plasma instabilities produced in the laser-plasma interaction. Both thermal and nonthermal electron and ion fluctuations can be measured with this technique through appropriate selection of the incident and collected light directions. In the experiments done in this research, only the ion fluctuations driven by the Brillouin instability were of direct interest. However, some general comments on the Thomson scattering diagnostic method will be made first.

Thomson scattering takes place when a light beam impinges upon a region with free electrons such as in a plasma. The electrons are perturbed by the electromagnetic field and re-radiate light due to their acceleration. If these electrons are already in motion, the incident light is Doppler shifted in the electron's frame as is the re-radiated Thomson scattered light in the laboratory frame. The outcome is a double Doppler frequency shifting of the Thomson scattered light. Since the electron scattering may be due to either uncorrelated or collective fluctuations, the Thomson scattering method can probe both types of plasma fluctuations. The difference wavevector of the incident probe beam and Thomson scattered light determines which is detected. Wavevector matching of the two electromagnetic waves and the wavevector of the fluctuations giving rise to the scattering is given by $\underline{k}_s = \underline{k}_0 + \underline{k}_f$ where \underline{k}_0 is the incident wavevector, \underline{k}_s the Thomson scattered wavevector and \underline{k}_f is the fluctuation wave vector. If $|\underline{k}_f \lambda_D| \gg 1$, where λ_D is the plasma Debye length, then the fluctuation scale length being sampled is smaller than the Debye shielding scale length. As a result, uncorrelated electron density fluctuations such as thermal motion are sampled. In the opposite case where $|\underline{k}_f \lambda_D| \ll 1$, long scale length electron density fluctuations are detected. These electrostatic wave fluctuations can be either ion or electron plasma modes and are distinguished by the

frequency shift of the scattered light. The phase velocity of the particular wave connects the frequency shift $\Delta\omega$ of the Thomson scattered light and the fluctuation wave number, $v = \Delta\omega/|k_f|$.

Simple geometrical arguments assist in interpreting Thomson scattering experiments. Figure 3.11 illustrates the wavevector geometry for Thomson scattering where θ is the angle between the incident and scattered light. With electromagnetic waves whose frequency is much larger than the electron plasma frequency,

$|k_0| \approx |k_s|$ and so $|k_f| \approx 2|k_0|\sin\theta/2$, or for small θ such as for Thomson scattering from Brillouin ion fluctuations,

$|k_f| \approx |k_0|\theta$. The associated wavelength shift of the scattered light is $\Delta\lambda = (2\lambda_0 v/c)\sin\theta/2$ where v is the component of the electron velocity in the k_f direction. For low velocity ion motion, the wavelength shifts can be very small, often less than one angstrom.

The plasma fluctuation levels associated with the sampled wavenumber determine the scattered light level. The scattering cross section $d\sigma$ written in terms of the scattering form factor $S(\omega, k)$ is $d\sigma = \sigma_T S(\omega, k) d\omega d\Omega$. Here $d\omega$ and $d\Omega$ are the frequency interval and light collection solid angle respectively and σ_T is the Thomson cross section, $8.85 \times 10^{-26} \text{ cm}^2$. Integrating $S(\omega, k)$ over all ω gives the total Thomson scattering for a selected k . Calculations for thermal plasma fluctuations [49] show:

$$S(k) = \int S(\omega, k) d\omega = 1/(1 + \alpha^2) + Z\alpha^4/[(1 + \alpha^2)(1 + \alpha^2 + Z\alpha^2 T_e/T_i)]$$

$$\alpha = 1/k\lambda_D \quad \text{Eq. 3.7}$$

where the first term is the electron mode contribution and the second is the ion mode contribution. When $k\lambda_D \ll 1$, the thermal Thomson scattering is primarily due to ion mode fluctuations; conversely, electron thermal motions dominate scattering when $k\lambda_D \gg 1$. When nonthermal levels of fluctuations are present from the CO_2 laser-plasma interaction, the form factor can be greatly enhanced and large Thomson scattered signals can be detected. It is in this context that Thomson scattering

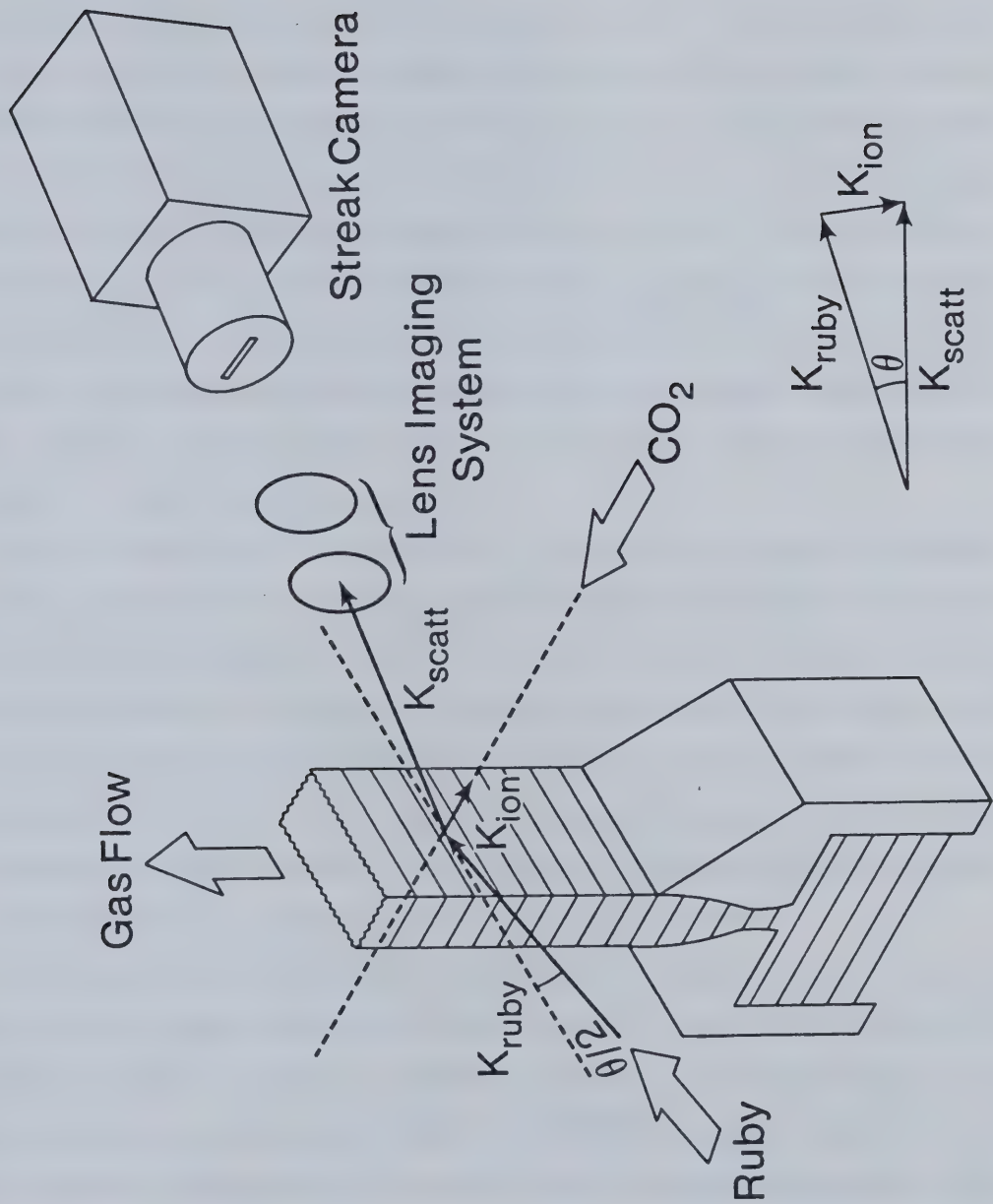


Figure 3.11 Thomson Scattering Wave Vectors in an SBS Experiment

was applied to the study of the Brillouin induced ion fluctuations in the CO₂ laser-plasma experiment.

The Q-switched ruby laser described in the interferometry experiment and a scattered light detector were the main instrumentation used in Thomson scattering. A simple lens focussed the ruby laser light onto the plasma and a second lens was positioned for Thomson scattered light collection. Figure 3.12 illustrates the equipment layout, including the beam dump and stray light shield which were necessary to prevent swamping the Thomson scattered light signal with stray ruby light. Precise alignment of the ruby laser and collection optics was done with the ruby laser alignment He-Ne laser illuminating a 200 micron diameter plastic microball positioned at the CO₂ laser focus. The He-Ne laser light specularly scattered off the microball and the light intercepted by the Thomson scattering collection lens could be seen by eye, allowing relatively easy positioning of the light detection equipment.

The ruby laser output was monitored by the Optics Technology photodiode (< 0.5 ns risetime) for scattered signal normalization and timing the laser with stimulated Brillouin backscattering. The 20 ns FWHM ruby laser pulse made timing with the short duration Brillouin event relatively straightforward although fine structure (≈ 150 ps period) was occasionally detected with high speed instrumentation. With a 7 mm ruby cavity aperture, 0.5 J pulses with 0.8 mrad half energy beam divergence were produced. Stops inserted in the ruby laser path to eliminate high divergence structure in the laser output lowered the amount of energy reaching the plasma to ≈ 160 mJ.

Three light detectors were used in the Thomson scattering experiments. One detector was an RCA 8645 photomultiplier which permitted absolute scattered light level measurements through a blackbody calibration procedure. With the modest 3.7 ns detection risetime, only time averaged density fluctuation levels were calculated from the amount of Thomson scattered light. The second Thomson scattered light detector was a PARC type 1205A Optical multichannel analyser (OMA). The OMA target head consisted of a silicon intensified target vidicon with an S-20 photocathode. The target plate was a linear array of 500, 25 micron wide channels each with ≈ 10 -20 photons per count sensitivity. Thomson scattered ruby light was focussed into a Perkin Elmer E-1 0.58 m grating spectrograph whose output was imaged onto the OMA target plate. The

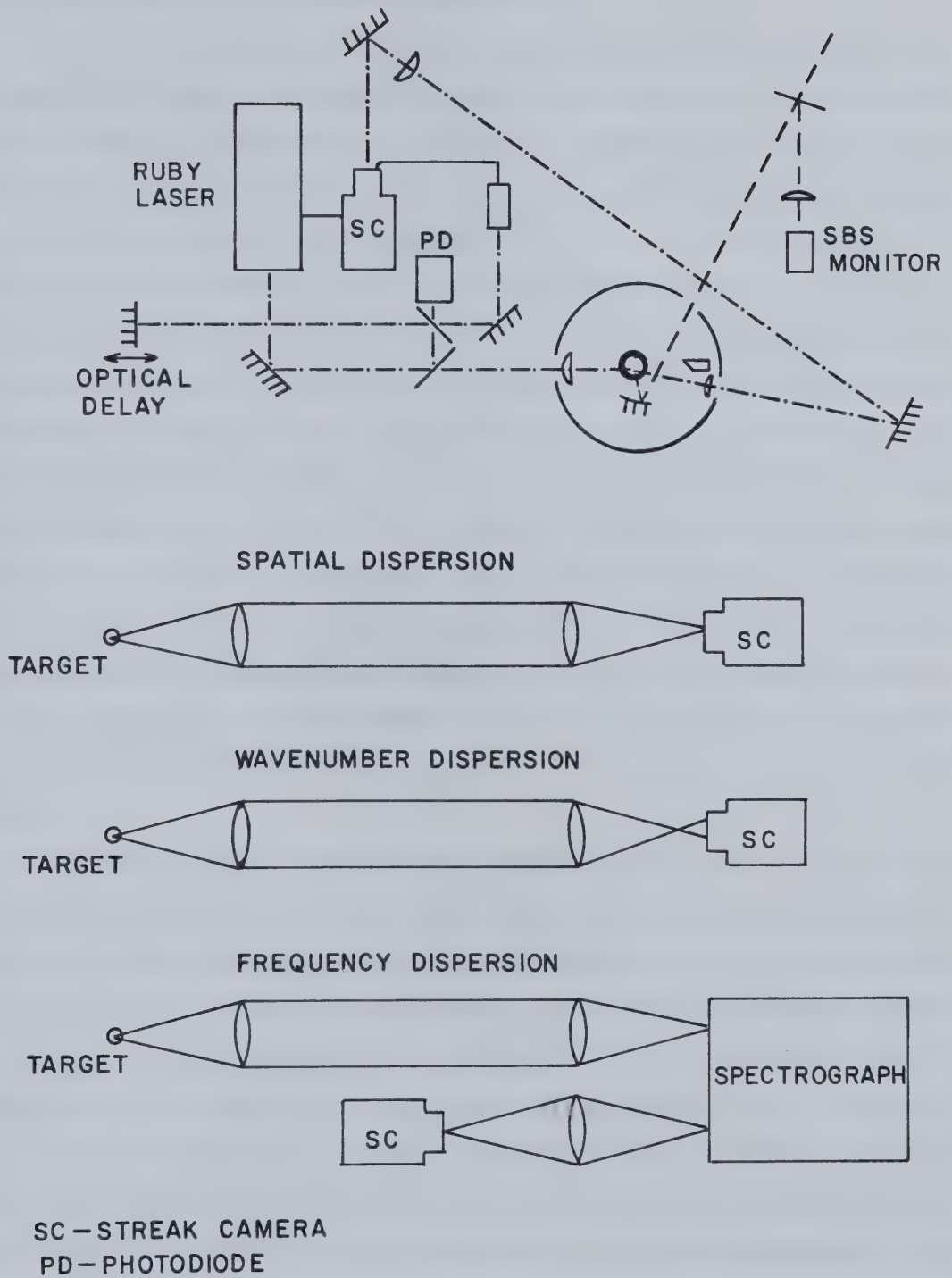


Figure 3.12 Thomson Scattering Experiment. Streak Camera Configurations are Shown.

.04 Å per channel dispersion and the 0.4 Å resolution of this spectrograph/OMA setup limited its usefulness in the Brillouin experiments.

The most useful detector for Thomson scattered ruby light measurements was a high speed streak camera. The scattering system is illustrated in Figure 3.13. The streak camera consisted of a Hamamatsu C979 temporal disperser, C1000-18 high gain vidicon camera and a C1330 temporal analyser. Ten picosecond resolution was possible with a 30 micron entrance slit and high light gain ($< 6 \times 10^3$) was achieved with a microchannel plate in the streak tube. Streak camera information was digitized by the temporal analyser system and displayed on a video monitor. The display field consisted of 64 windows across the 3 mm streak camera entrance slit and 256 time channels. Various data routines of the temporal analyser permitted graphical displays of the streak camera counts. Consequently, the digitized streak camera field was three dimensional as time, space and intensity co-ordinates were displayed. The space coordinate was also calibrated for wavelength or wavenumber of the Thomson scattered light as different imaging methods were used. A fiducial was placed to one side of the streak camera entrance slit to permit scattered light normalization and timing to the ruby laser output. A 50 micron diameter core x 30 cm graded index silica fiber (1275 MHz km bandwidth) whose free end was illuminated with a fraction of the ruby light was used for this purpose.

As mentioned above, various imaging techniques were used to illuminate the streak camera's entrance slit. Spatial imaging was done with a magnifying relay lens focussing the collected Thomson scattered light onto the camera slit. This arrangement allowed one to follow the temporal evolution of the ion mode spatial distribution. Better than 10 micron resolution referred to the plasma source was achieved with the f/10 focussing onto the entrance slit. In these spatial measurements, it was important to ensure that the ruby laser beam uniformly illuminated the whole scattering region. This required a slight defocussing of the ruby probe beam at the CO₂ laser-plasma interaction volume. Figure 3.12 illustrates the optical configurations for spatial measurements as well as wavenumber and frequency spectra of the scattered light. Defocussed illumination on the streak camera slit permitted wavenumber discrimination of the Thomson scattered light. The simpler approach with a single lens collimating the scattered light and projecting

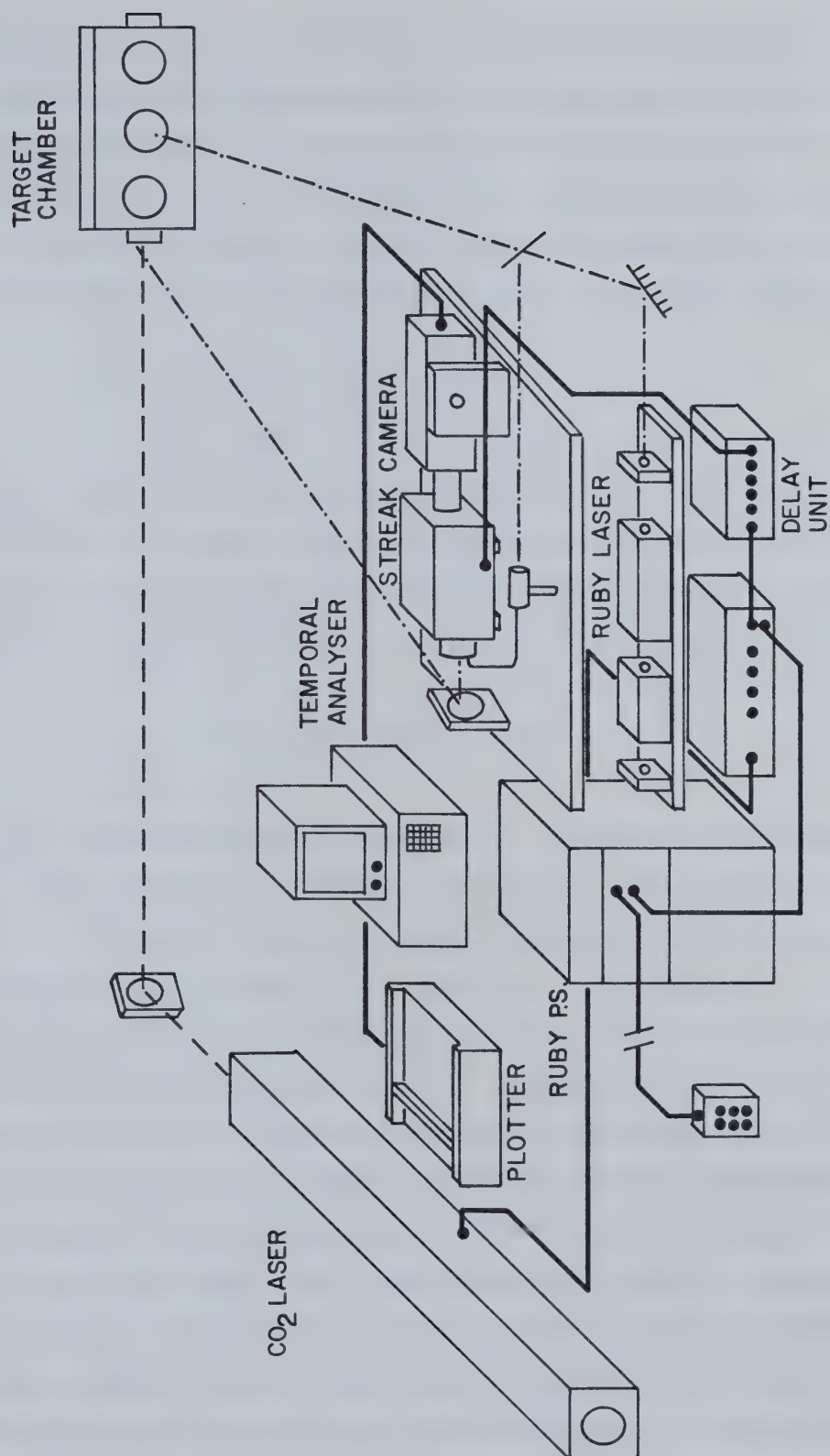


Figure 3.13 Main Components for Streak Camera Thomson Scattering

it onto the camera slit was not implemented as it required a small aperture lens close to the CO₂ laser focus. Both small aperture diffraction and obstruction of the CO₂ laser beam by a close proximity lens made this direct solution impractical. Ray matrix calculations for the optical components and path in Figure 3.12 show how in this wavenumber discrimination method, a poor choice in optical design could introduce a source position dependence in the streak camera illumination. In ray matrix notation:

$$\begin{pmatrix} r_{out} \\ r'_{out} \end{pmatrix} = \begin{pmatrix} A & B \\ C & D \end{pmatrix} \begin{pmatrix} r_{in} \\ r'_{in} \end{pmatrix}$$

where r_{in} and r_{out} are the source and detected ray distances from the optic axis and r' denotes their slope. The ray matrix coefficients A,B,C and D are calculated from the product of each ray matrix along the optical path. To eliminate the effects of source position on r_{out} the A coefficient must be zero which imposes the criteria:

$$x = f_2/[1 - f_2/(L - f_1)] \quad \text{Eq. 3.8}$$

where f_1 is the collection lens focal length, f_2 is the imaging lens focal length and L is their separation. The required distance from the imaging lens to the camera slit is x . The collection optics configuration was set up to satisfy this condition. ($f_1 = 10$ cm, $f_2 = 30$ cm, $L = 350$ cm, $x = 33$ cm).

For the small Thomson scattering angle in this experiment, the ion fluctuation wavenumber was directly proportional to θ , the scattering angle. Typical θ values expected for Thomson scattering from the Brillouin fluctuations were six to eight degrees, depending upon the plasma electron density and wavenumber bandwidth. These small angles required effective ruby laser beam spatial filtering and dumping to prevent stray light interference. After taking these precautions, Thomson scattering was positively indicated as ruby light was detected only when a scattering plasma was present. Light refraction from the plasma was not important at these angles as was estimated through an approximation of the eikonal equation and the known refractive index profile measured through ruby laser interferometry.

Finally, in exactly the same manner as with the OMA, the streak camera was also located behind the E-1 grating spectrograph for scattered light spectral measurements. Time broadening across the diffraction grating [50] limited the ultimate temporal resolution capabilities. This temporal smearing is the result of path length differences across the grating for a given wavelength, and is given by

$$\Delta\tau = mN\lambda/c \quad \text{Eq. 3.9}$$

where $\Delta\tau$ is the time broadening, N is the number of grating lines intercepting the λ wavelength light and m is the diffraction order. Time broadening, $\Delta\tau > 100$ ps is expected from the E-1 spectrograph. Although this temporal resolution was sufficient for all but the fastest modulations, the spectral resolution still limited the overall usefulness of these measurements.

All of these streak camera diagnostic configurations were used to completely characterize the ruby Thomson scattered light. Subsequent calculations from these measurements provided important insight concerning the ion fluctuation content of the plasma and, in particular, those fluctuations driven by the Brillouin instability during the CO₂ laser-plasma interaction.

4. Results

4.1 Introductory Remarks on the Experimental Results

A variety of experiments are presented and analysed in this chapter. The results are examined in an attempt to first characterize the laser and plasma conditions under which the light scattering occurs and then to explain the nature of the stimulated Brillouin instability. The chapter is divided into three sections. In the first section, the plasma electron density and temperature are discussed, followed by a brief recapitulation of the carbon dioxide laser behaviour both when gain switched and injection mode-locked. The next section presents preliminary measurements of the Brillouin backscattered light from which certain model predictions are validated. Finally, in the last section, more detailed investigations into the ion mode behaviour are interpreted. These are based exclusively on measurements of ruby laser Thomson light scattering from ion acoustic waves driven by the Brillouin interaction. Cumulatively, this chapter identifies the laser-plasma processes which determine the space and time evolution of the Brillouin scattering.

4.2 Interferometric Measurements of the Plasma Density

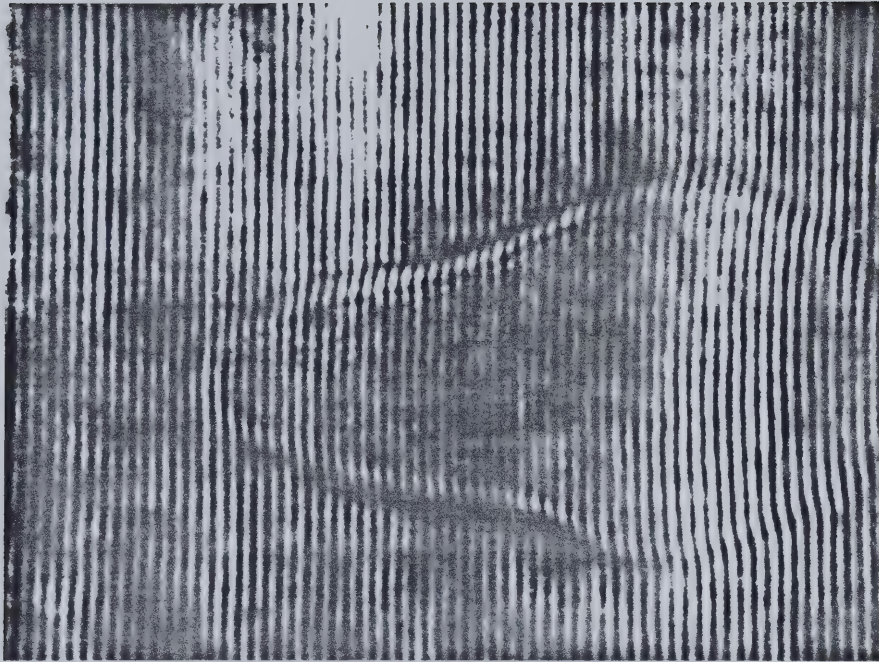
Several interferometric measurements of plasma electron density were performed with the apparatus described in Chapter 3. Not only was the average electron density measured, but the axial and radial profiles were computed through Abel inversion of the interferogram. These density measurements represent data which were crucial for determining the stimulated Brillouin growth rate and investigating whether plasma inhomogeneities or interaction nonlinearities in a homogeneous plasma control the Brillouin gain.

Three distinct laser-target conditions were examined. Two test conditions were with a gain switched CO₂ laser irradiating the oxygen gas target and a third with the injection mode-locked laser. The oxygen stagnation pressure : helium chamber pressure ratio was either 2000 Torr : 10 Torr or 2000 Torr : 0 Torr for the gain switched carbon dioxide laser while a 10 Torr helium background was always maintained for the IML laser shots. The two conditions with a 10 Torr helium background were almost exclusively

used for further laser-plasma studies as it assured reproducible underdense plasmas even though there was a penalty of neutral gas density gradients within the target which could restrict the extent of uniform plasma.

Figure 4.1 shows an interferogram for a plasma within 1 ns of the start of the Brillouin scattering event. A 700 MW peak power CO₂ laser irradiated the helium stabilized oxygen target. In the same figure, the electron density is plotted for the first few fringes from the leading edge of the plasma. The axial density is well behaved in a 100 micron diameter cylinder within which the average electron density is $4.3 \times 10^{18} \text{ cm}^{-3}$ (excluding the first fringe at the ionization front) and the density gradient scale length, $[(dn/dx)/n]^{-1} = 600 \text{ microns}$. The formed plasma extends 1.5 mm axially with a boundary approximating that of the calculated laser focus though wider as a result of hydrodynamical expansion and photoionization from the intense line and bremsstrahlung emission from the laser heated plasma. Also, as seen in the interferogram, the back end of the plasma is shaped like a diverging lens ($\mu < 1$ for plasma) for which beam refraction can expand the laser spot size over its vacuum dimensions. A computer simulation with CASTOR [51] supported this idea though unfortunately the simulation did not include photoionization. Figure 4.2 is a second electron density profile only now measured 3 ns after the stimulated Brillouin scattering began. The average axial electron density is $\approx 0.7 n_c$, which is considerably higher than that in Figure 4.1. A combination of Abel inversion error ($\pm 0.05 n_c$) and shot variation could account for the density change. From many interferograms, the mean electron density was calculated to be $\approx 0.5 n_c$ in the time interval 3 to 8 ns from the start of the laser-plasma interaction.

When the gas jet was operated with 0 Torr helium, similar electron densities and radial profiles were obtained. At first sight, this might seem surprising because of the extreme underexpansion in the jet flow. However, the flow Mach number was low and an intermediate density core to the gas flow persisted. Plasmas formed under these conditions were generally of longer axial extent and the ionization front moved axially $\approx 3.8 \times 10^6 \text{ cm/s}$. With 10 Torr helium background, on the other hand, the ionization front moved at a speed $< 1 \times 10^6 \text{ cm/s}$ during the Brillouin instability. This lower speed is thought to be due, at least in part, to laser inverse bremsstrahlung absorption in



25 micron fringe spacing

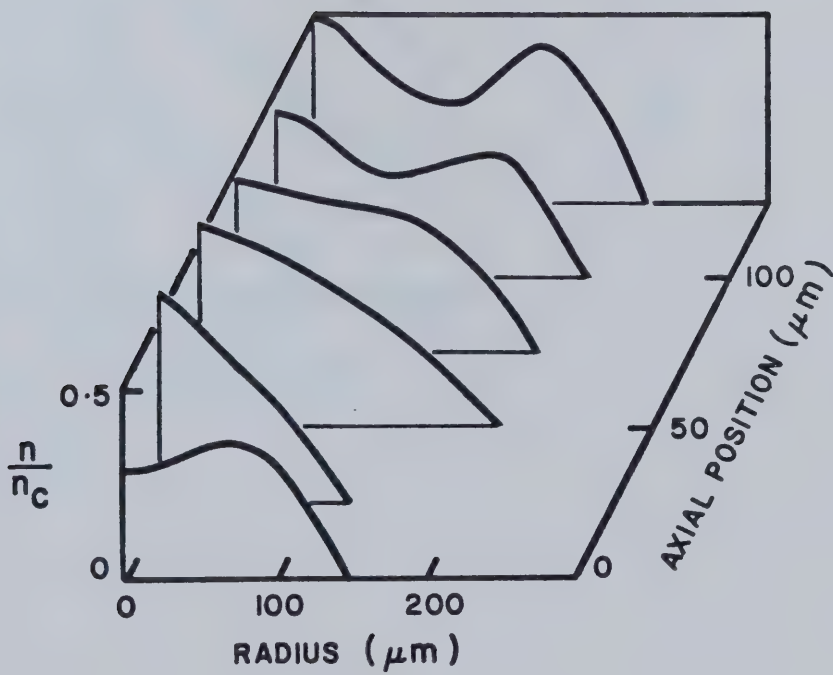


Figure 4.1 Gain Switched Laser Plasma Interferogram and Abel Inverted Density Profiles.

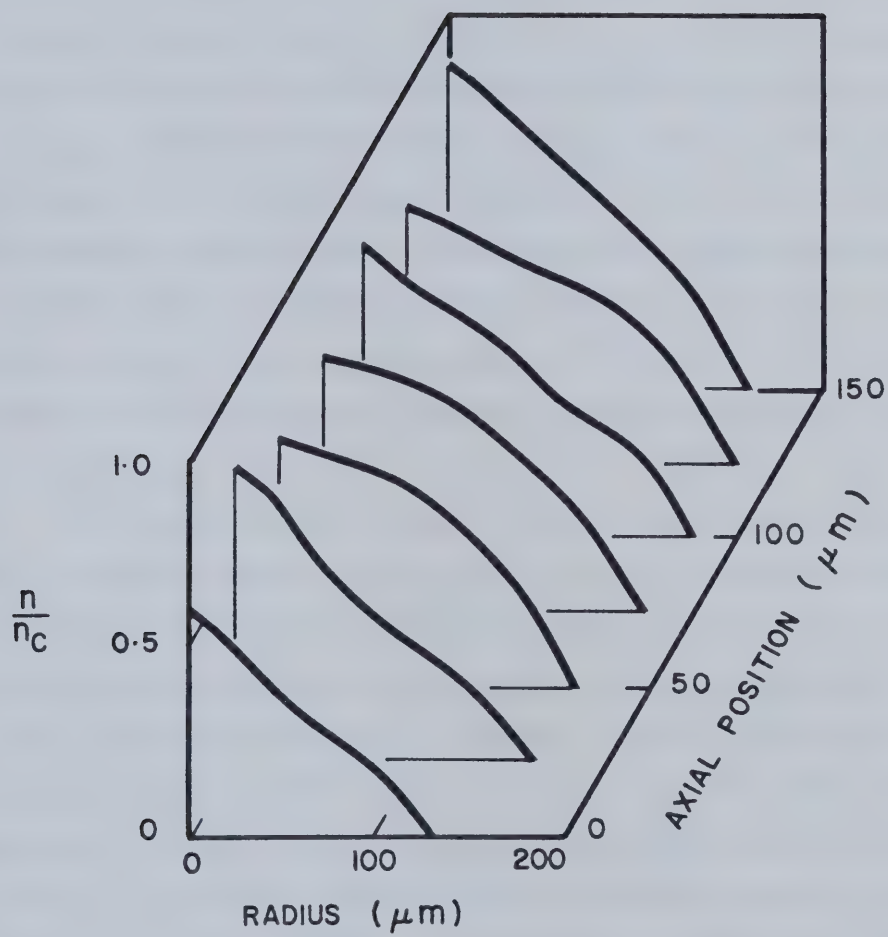


Figure 4.2 Plasma Electron Density Profiles 3 ns after the start of SBS

the low density, low temperature plasma formed away from the interaction zone leading to a decrease in laser intensity at the ionization front [52] (where radiation and conduction losses balance the heating resulting in a relatively stationary front).

The final series of interferograms were made for 2 ns FWHM laser pulses irradiating the gas target. Figure 4.3 presents density profiles for the plasma created during the Brillouin scattering. Again, the plasma boundary was similar to that expected from the laser focussing geometry but there were two striking differences from the previous interferograms. First, the ionization was significantly lower than that obtained with the gain switched laser. With the short 2 ns laser pulse, the Brillouin scattering was prompt because of the higher pump intensities at the time of gas breakdown but correspondingly the finite ionization times result in lower ionization. In the gain switched laser irradiation case, the Brillouin scattering was delayed ≈ 4 ns after gas breakdown. This long time explains the increased ionization of the oxygen for the gain switched laser experiment. The second feature of the density profiles in Figure 4.3 was the sudden density jump from $\approx 0.17 \ n_c$ to $\approx 0.31 \ n_c$ (calculation error $\pm 0.05 \ n_c$ in both cases) over 50 microns. This density step was the result of the plasma breakdown crossing a Mach line in the neutral gas flow. The electron density gradients were not smeared through plasma expansion at this early time of plasma formation (as also evidenced through the low electron densities). From this observation it is clear that the laser focus position has to be carefully chosen to ensure that the plasma characteristics are not complicated by the density structure in the neutral gas flow. Positioning the CO₂ laser focus 300 microns further back towards the laser eliminates this problem in the Brillouin interaction zone. Subsequent interferograms consistently showed an average electron density $n = 0.30 \ n_c \pm 0.05 \ n_c$ as expected for a low ionization plasma.

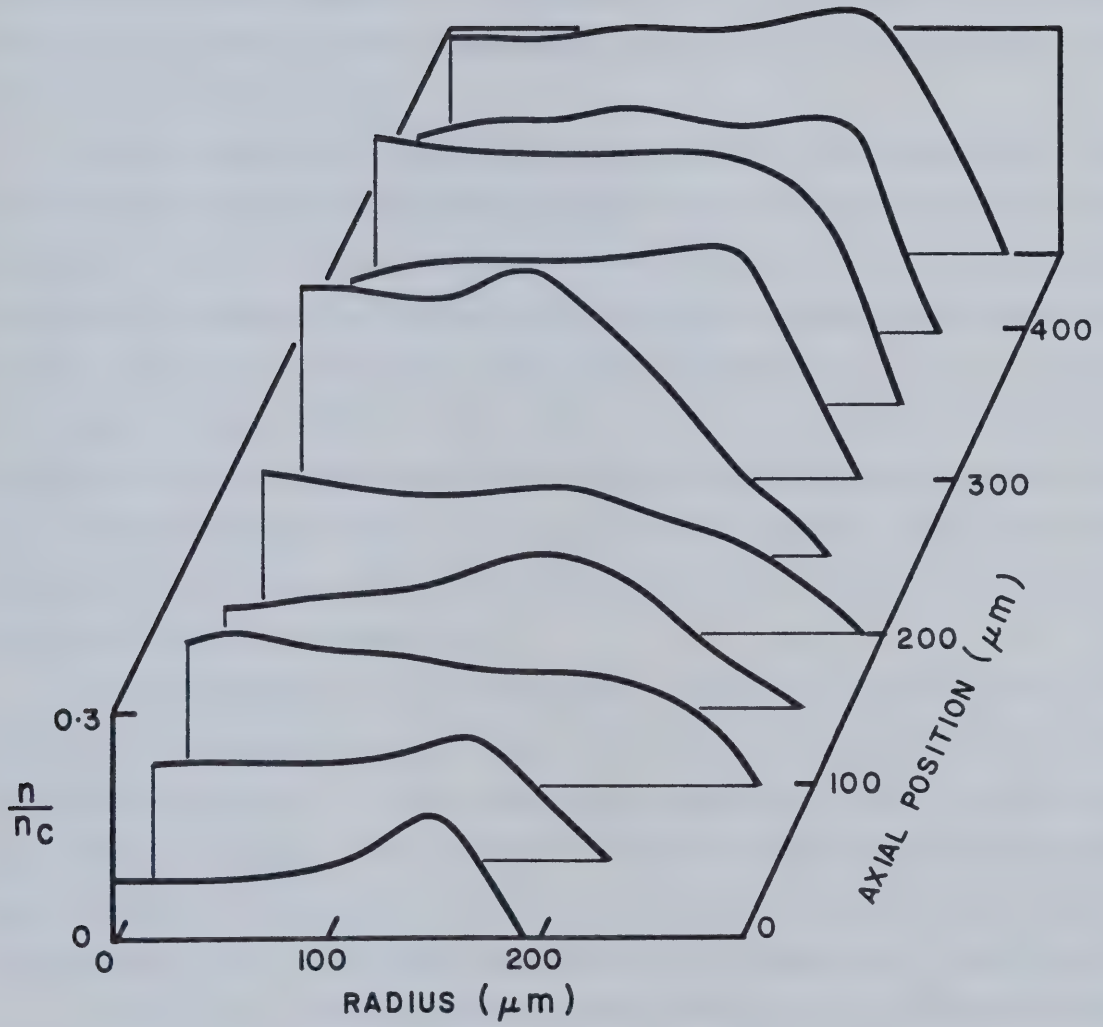


Figure 4.3 Electron Density Profiles for an IML Laser Irradiated Plasma

4.3 Electron Temperature Measurements

The second plasma parameter diagnosed was the electron temperature. As discussed in the experimental methods, an absorber–scintillator detector arrangement was used to obtain relative X-ray signals for varying absorber foil thicknesses. These relative signals were compared to those calculated for an oxygen plasma, emitting both line and bremsstrahlung radiation at different temperatures and detected through various thickness of aluminum foil [48].

Electron temperature measurements were done for plasmas created with a gain switched laser and the injection mode–locked laser. Figure 4.4 is a plot of the measured X-ray signal from the gain switched laser irradiated plasma for several aluminum foil thicknesses. For comparison, these experimental results are superimposed on theoretical relative X-ray signal curves. The best fitting theoretical curve gives an electron temperature estimate of 120 ± 20 eV. The accuracy of the temperature estimate was limited by the shot-to-shot variation in the X-ray signal at any foil thickness. There was no significant temperature change over the range of 300 MW to 1 GW incident laser power. With the IML laser, similar X-ray measurements gave $T_e = 150 \pm 20$ eV for 500 MW to 1 GW incident laser power.

All measurements were time integrated by the 4 ns detection risetime and consequently the temporal evolution of the X-rays was not examined in detail. However, it was observed that the < 20 ns signal pulse duration was shorter than the ≈ 40 ns gain switched laser pulse. This was a result of plasma rarefaction which lowered both plasma temperature and density at late times in the laser–plasma interaction. Plasma interferograms taken 15 ns after plasma breakdown showed a low density core ($n < 0.1 n_c$) which would have a greatly diminished X-ray emission even with continued laser heating and sustained temperature. The low temperature, higher density plasma periphery would also be a weak X-ray emitter with the overall consequence of a short lived X-ray signal as compared to the laser pulse.

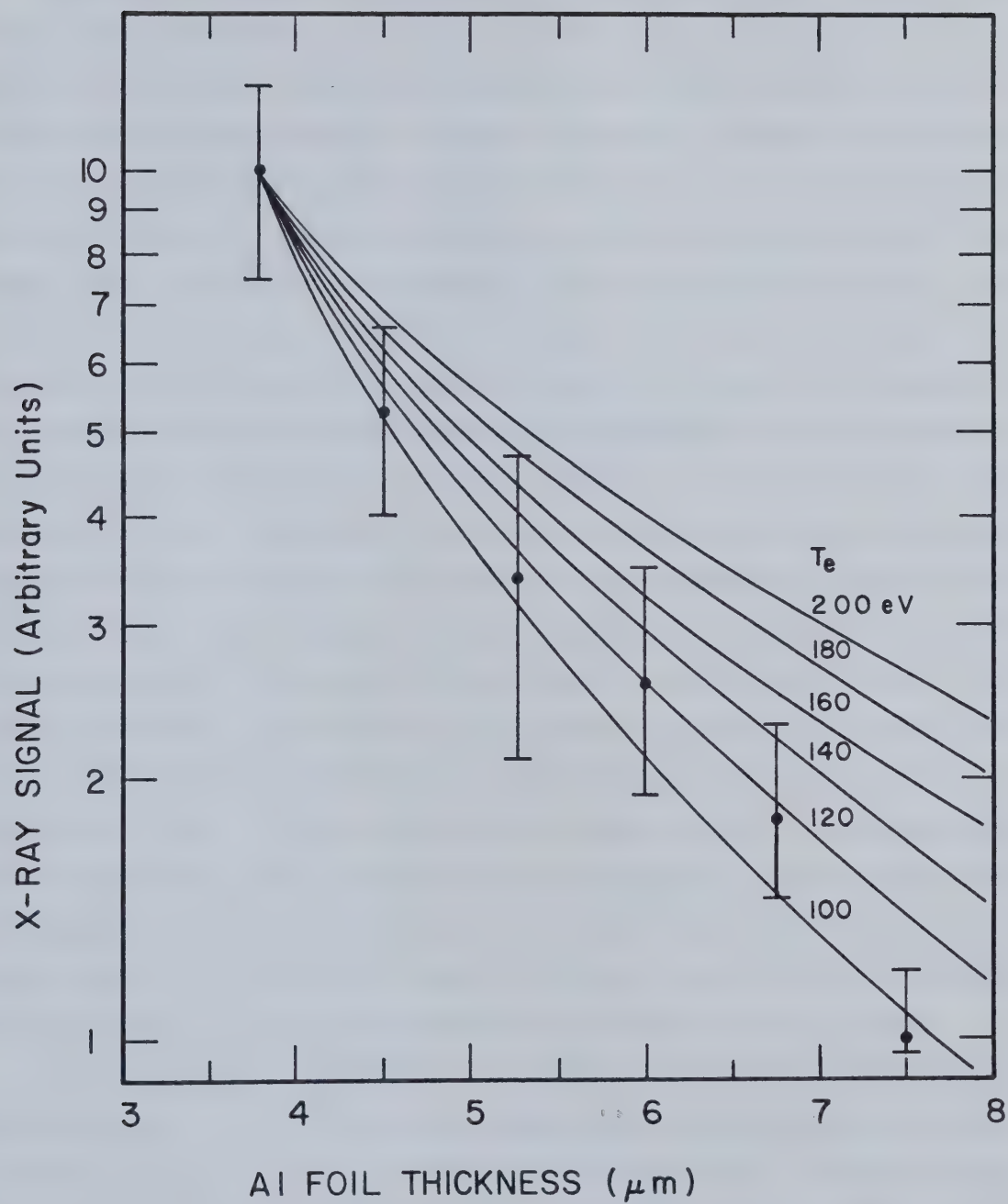


Figure 4.4 Electron Temperature for a Gain Switched Laser Irradiated Plasma

4.4 Preliminary Observations of Brillouin Scattering

The first and easiest characterization of the stimulated Brillouin scattering was through monitoring the backscattered red-shifted CO₂ laser light. An 8% sodium chloride beamsplitter in the incident laser path collected directly backscattered light (to within ≈ 5 mrad). Earlier laser plasma studies on the polar distribution of CO₂ laser light scattered from this target (Offenberger [53]), determined that during the first 10 nanoseconds after gas breakdown, only backscattering occurred. Late time forward refraction of the incident light occurred but was unrelated to the Brillouin scattering. Besides ray re-tracing [54] and a gain maximum [16] to explain the strong directionality of the backscattered light, polarization and plasma density gradients could be very important in this experiment. Brillouin sidescatter amplification is undiminished for Transverse Electric (TE) polarized light and is zero for transverse magnetic (TM) polarization [12]. For this reason, the maximum instability gain for an unpolarized gain switched laser beam would be in the backwards direction. The TE polarized IML laser beams also exhibited strong direct backscatter which suggested that other mechanisms were sufficient to control Brillouin sidescattering. These could include the finite focal spot size and the 200 – 300 micron radial density gradient scale length measured from the interferograms which would restrict the plasma length available for sidescatter gain. As mentioned in the theory chapter, this is due to the phase mismatch from the electromagnetic wave dispersion in the inhomogeneous plasma limiting the spatial amplification. In addition, laser beam inhomogeneities could act to enhance the transverse density inhomogeneities and further inhibit sidescatter. The cumulative effect of all these features to the laser-plasma interaction is that direct backscatter of the Brillouin generated light should dominate.

Preliminary Brillouin scattered light measurements identified the temporal features of the instability. Figure 4.5 shows the incident gain-switched CO₂ laser, laser light transmitted through the plasma and Brillouin backscattered light. The relative timing between these plots is accurate to better than 1 ns. Axial mode beating in the CO₂ laser output resulted in typically $\sim 50\%$ modulation of the beam intensity. Prior to gas breakdown, the transmitted light followed the incident light but with breakdown the signal fell rapidly to noise level as light absorption and scattering occurred. The Brillouin scattered light consistently appeared ± 4 ns after breakdown (independent of the incident

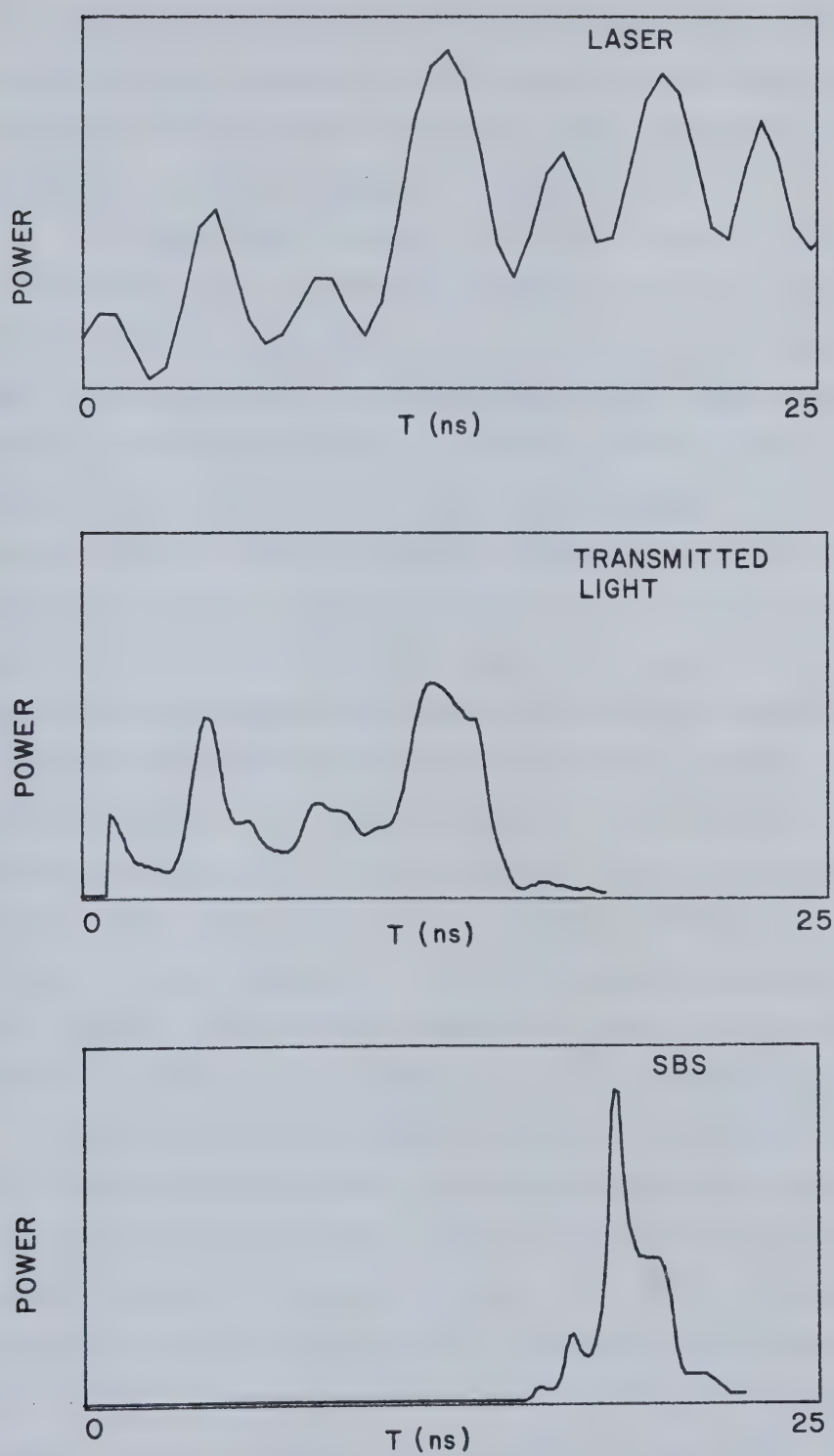


Figure 4.5 Gain Switched Laser Transmission and SBS

laser power). This delay seems likely to have resulted from a combination of limited ionization rate, laser absorption during ionization and plasma electron density and velocity smoothing from hydrodynamic flow. The exact contribution from these was not separable from a simple measurement of light transmission.

The Brillouin signal risetime $\sim 0(1 \text{ ns}) \gg 1/\omega_s, 1/\gamma_0$ suggested that fast temporal growth to convective saturation did not occur. Time resolved ruby laser Thomson scattering measurements of the ion mode confirmed this and will be discussed later. The instability growth can be moderated by wave energy loss mechanisms such as inverse bremsstrahlung absorption of the pump and backscattered light and ion Landau damping or ion trapping acting on the ion mode. However, in view of this long risetime and the duration of stimulated Brillouin scattering, a steady state model description is likely adequate. Figure 4.5 shows an example of a 4 ns duration Brillouin scattered light pulse during which time convective saturation can occur. Over many laser shots, the backscattered light varied in pulse width from 2 ns to 8 ns duration with an average of 4 ns. More quantitative discussion will follow in succeeding sections. One final comment on the gain-switched laser is that the scattered light modulation was not completely correlated with the pump modulation. Brillouin instability gain is proportional to pump intensity, but as seen in Figure 4.5, the scattering terminates before the laser pump is removed. This spiky behaviour of SBS has been observed by other researchers ([53], [55], [56]) even with temporally smooth laser pulses. No single mechanism has been positively identified to cause this abrupt termination of the Brillouin instability.

Similar studies on the IML laser-plasma interaction showed notable differences to that with the gain switched laser. In the first place, Brillouin backscattering was prompt. In Figure 4.6, the incident CO₂ laser, the Brillouin backscattered light and the ruby Thomson scattered signals are illustrated. As seen in this figure, the scattered light turns on abruptly within 2 ns of the pump arrival. The ruby Thomson scattered signal provided a useful indicator of plasma formation and also confirmed the rapid rise of the Brillouin instability. The Ruby Thomson scattered signal had a precursor 750 ps ahead of the Brillouin ion mode scattering. This source of this precursor is not known although enhanced Rayleigh scattering due to a neutral O resonant state could take place [57]. The main point is that the Brillouin instability occurred much sooner after breakdown than for

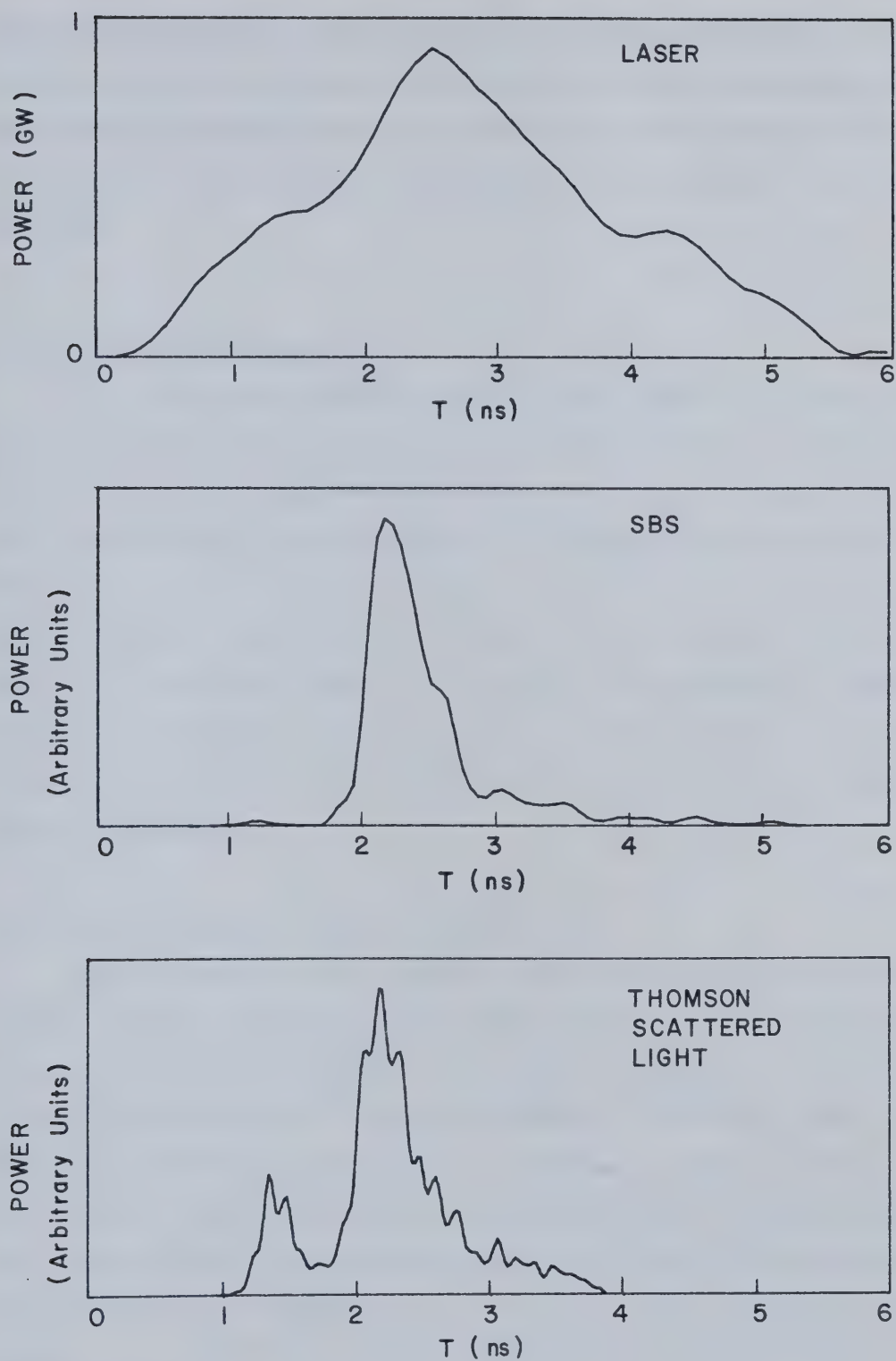


Figure 4.6 SBr and Thomson Scattering From an IML Laser Irradiated Plasma

the gain switched CO₂ laser because of the high initial pump intensities. Again, the Brillouin instability decreased abruptly and from Figure 4.6, was clearly not related to lack of pump intensity. The instability duration was even less than that normally seen with the gain switched laser and may have been related to rapid plasma modification in the strong laser pump field.

4.5 Infrared Light Diagnostics

In the last section, preliminary remarks were made on the Brillouin instability without expanding on its characteristics and how they compare to model predictions. Here, infrared spectral measurements and CO₂ light reflectivity determination will be reported and analysed. The complex behaviour of stimulated Brillouin scattering in a real experiment is difficult to explain through one self-consistent model. However, a composite description can satisfactorily account for the principal observations. The results will be interpreted through the ion heating models developed in Chapter 2. All together, the observations indicate that the convective saturation of the Brillouin instability is principally determined from plasma density gradients and ion acoustic wave damping on heated ions.

4.5.1 Backscattering with a Gain Switched CO₂ Laser

The first observations of stimulated Brillouin scattering were made with the gain switched CO₂ laser irradiating the gas target. Red shifted backscattered light was focussed onto either a Ge: Au detector or a pyroelectric detector with a suitable number of mylar sheet attenuators in front of the detector to ensure linear signal response. Reflectivity calibrations were made by inserting a sodium chloride window retro-reflector in the CO₂ laser beam path to provide 8% back-reflected light when the laser system was fired into an evacuated target. With average focal spot intensities of 6×10^{12} W/cm², power reflectivities of $R = 0.20$ were recorded and at half this intensity $R = 0.14$. Yet a further reduction of two in pump intensity to 1.5×10^{12} W/cm² resulted in a drastic reduction in reflectivity to $R = 0.04$. Thus a knee in the reflectivity as a function of pump intensity occurred at 3×10^{12} W/cm² above which R slowly varied. These results are similar to those reported before on this gas

target [24]. The values referred to are peak power reflectivity; as a consequence of the short scattering time as compared to the pump duration, the energy reflectivity was lower by approximately an order of magnitude.

Further details on the Brillouin instability, which assist in formulating a model, came from time integrated infrared spectra of the backscattered light. For these measurements, the backscattered light was directed onto the infrared multichannel analyser after passing through a grating spectrograph. Figure 4.7 shows three types of spectra which were detected. Figure 4.7(a) is a representative spectrum of red shifted backscattered light generated in stimulated Brillouin scattering. The apparent wavelength red shift from 10.59 microns was 55 \AA with a 20 \AA FWHM. Before deconvolving the instrumental function as discussed in section 3.4.1, the apparent width was 30 \AA , indicating that careful handling of the spectral data was required.

Several interpretations could possibly account for the spectral width though the most probable explanation appears to be ion wave damping. Plasma velocity gradients or density gradients could also cause spectral broadening, but are much less likely for our conditions. The frequency dispersion due to an approximately 100 micron long Brillouin active region, as determined through model reflectivity predictions and direct measurement through ruby Thomson scattering, determines the possible spectral spread. Doppler shifted ion mode and electromagnetic wave dispersion together alter the ion mode frequency by $d\omega \sim (c_s + u)dk + kdu$ where u is the plasma axial flow speed. Electromagnetic dispersion enters through wavenumber matching in k . Without the laser depositing energy in the plasma, it would be simple to estimate the flow velocity gradients du/dk from the observed density gradients by using the pressure balance equations $\nabla n_i u^2/2 = -\nabla T_e n_e$. However, the presence of both electron temperature and electron density gradients in the plasma compound the difficulty of directly applying the pressure balance equation. More rigorous computer simulations using CASTOR indicate [51] axial velocities $\dot{\pm} 1 \times 10^6 \text{ cm/s}$ which are small compared to c_s . Also, the measured 600 micron density gradient scale length is long compared to the 100 micron Brillouin interaction zone, eliminating it as a likely candidate to explain the observed backscattered light spectral widths. Thus, ion acoustic wave damping remains as the most likely explanation for the large Brillouin instability

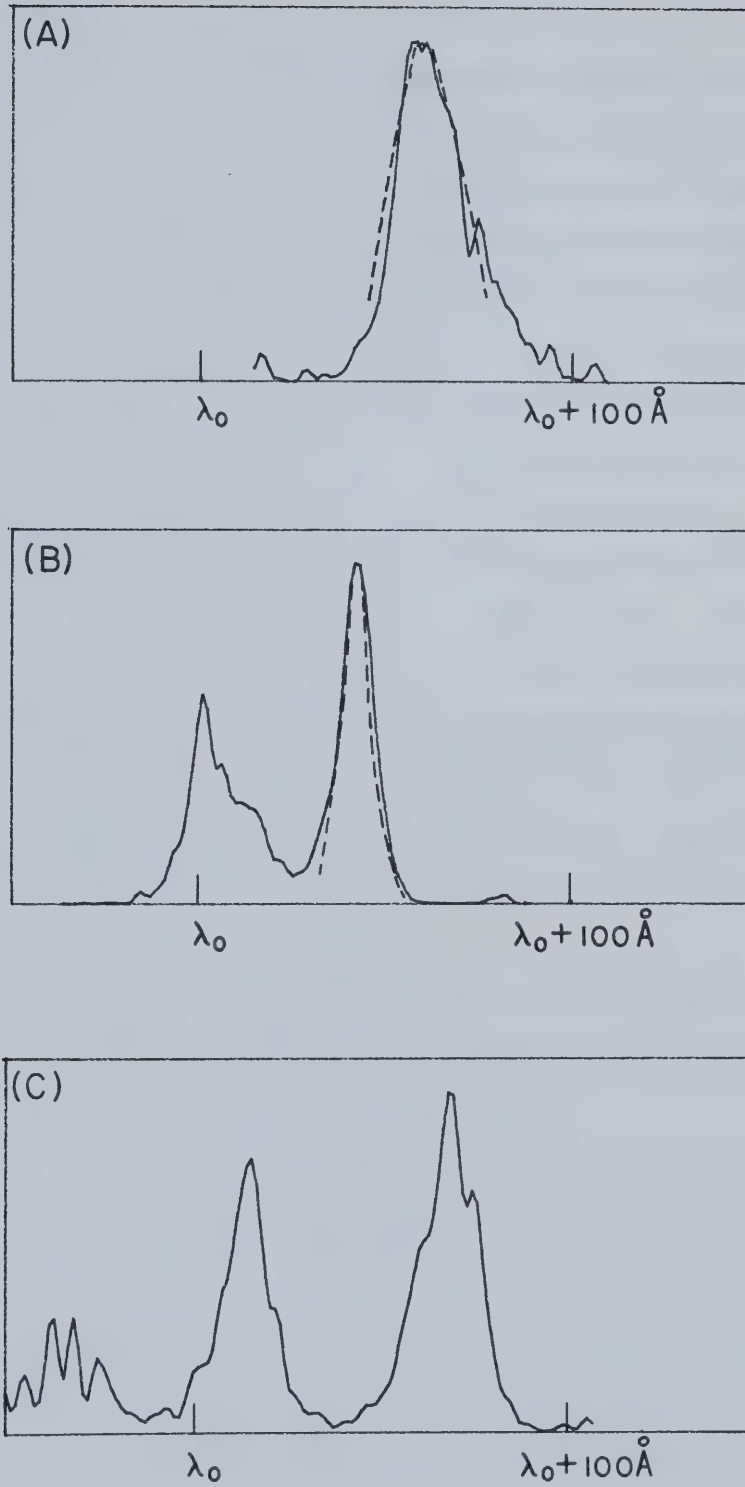


Figure 4.7 Backscattered Light Spectra from a Gain Switched Laser Irradiated Plasma

frequency bandwidth.

Ion wave damping can broaden the resonant frequency spectrum (even for $\Delta k/k \ll 1$) and indeed the damping coefficient can be estimated from the observed backscattered light spectrum, which we calculate now. Although a significant contribution of the backscattered light was due to the rising and falling portions of the Brillouin signal, application of steady-state formulae allow spectral width estimates. Pump depletion can be ignored for low Brillouin reflectivities whereby $R \approx \epsilon \exp G$ where G is the convective gain in the unstable region, $G = k_0 L n_{os} v_{os}^2 / 8 v_e^2 \gamma_s n_c$. The ion wave frequency dependence in G is through the ion wave damping γ_s / ω_s . The noise source ϵ is estimated from Equation 2.24 to be CO₂ laser light reflected from the plasma density gradients. This approximation yields $\epsilon = 10^{-3}$ when $n/n_c = 0.5$ and the density gradient scale length is 20 microns. Noise source estimates from the reflectivity curves [24] give similar values. Typical reflectivities and pump intensity are, $R = 0.15$ and $(v_{os}/v_e)^2 \approx 1$ respectively. With an 80 micron interaction length and the estimated gain $G=5$, the inferred ion wave damping from the gain expression is $\gamma_s / \omega_s = 0.6$. This large damping factor implies strong ion wave dissipation.

The correct kinetic frequency dependent gain calculation incorporating ion Landau damping provides a comparison to the measured spectra shown in Figure 4.7. The gain factor G written to include frequency dependence is

$$G = G_{\max} \frac{\gamma_s / \omega_s}{(\gamma_s / \omega_s)_{\max}}$$

Equation 2.26 is used to calculate the damping factor, γ_s / ω_s as a function of the backscattered light wavelength. A curve fitting of the calculated backscatter spectra to the experimental spectra in Figure 4.7 using the proper susceptibilities for variable T_e , T_i gives the plasma electron temperature and electron-to-ion temperature ratio. The calculated spectral peaks were sensitive to the electron temperature while the widths were sensitive to the temperature ratio. However, the spectral shape was not strongly affected by the choice of G_{\max} . This

weak G_{\max} dependence increases the confidence in the curve fitting estimates of T_e and ZT_e/T_i from the backscatter spectra. The dashed line in Figure 4.7(a) is a curve fitting with $T_e = 130$ eV and $ZT_e/T_i = 1.0$. This value for T_e is in good agreement with the value of 120 eV determined from X-ray measurements. The large ion temperatures $0(ZT_e)$, however, are not expected from electron-ion collisional equilibration alone, further justifying an ion heating model.

We now address the question of ion heating. At low Brillouin reflectivities, heating estimates from the energy deposited to the ions in the Brillouin interaction show that there may not be sufficient time to heat all the ions. The fastest ion heating rate for a stationary plasma would be

$$dT_i/dt = (\omega_s/\omega_0)(RI/n_iL)$$

where ω_s/ω_0 is the Manley Rowe energy fraction transferred to the ions in the Brillouin instability, R is the power reflectivity, I is the pump intensity, n_i is the ion density and L is the interaction length. For 20% Brillouin reflectivities and 1×10^{13} W/cm² pump intensities, the ≈ 600 eV/ns ion heating rate calculated from the above can account for the high ion temperatures. However, for 5% reflectivities and 3×10^{12} W/cm², the ion heating rate is too slow. Under these low reflectivity conditions, it seems more probable that some ion fraction is trapped and heated to $T_i \sim 0(ZT_e)$. Indeed, simulations would suggest that this occurs [11]. The broadened gain bandwidth due to ion Landau damping on the fraction of heated ions n_t/n , would be the same as if all the ions were heated. The damping factor, however, is diminished by n_t/n and the curve fitted ion temperature estimate is that of the trapped and heated ions. Any low temperature ions in the plasma would not broaden the Brillouin backscatter resonance.

The spectral data are not always so easily interpreted as seen in Figure 4.7(b) and 4.7(c). Both of these spectra show significant specular reflection as well as the clearly identified Brillouin backscattered component. In Figure 4.7(b), the narrow ion wave feature is curve fitted as above only now the electron temperature and electron-to-ion temperature ratio are $T_e = 90$ eV, $ZT_e/T_i = 2.5$. The smaller ion Landau

damping is attributed to decreased Brillouin reflectivity resulting from a lowered pump intensity. In some laser shots, the time integrated backscattered light had a large specular reflection coefficient. Figure 4.7(b) and 4.7(c) are two examples of this. Overdense plasma could form in the supersonic gas target during the laser-plasma interaction and reflect incoming CO₂ laser light. This specular scattering from overdense plasma and the Brillouin scattering do not necessarily occur simultaneously or at the same power levels. Unfortunately, the temporal features of the specular light component are not known from these time integrated spectral measurements. Figure 4.7(c) also has a small amount of 20 Å blue shifted light due to Doppler shifted reflection from a moving plasma boundary. Overall, the backscatter spectra in Figures 4.7(b) and 4.7(c) occurred infrequently and the majority of the backscatter spectra were well behaved Brillouin spectra as illustrated in Figure 4.7(a).

Although the reflectivity and spectra of the Brillouin backscattered light could be accounted for through ion trapping, heating and Landau damping, the effective interaction length, remains to be explained. For a Gaussian laser beam, a diffraction limited focus has a half intensity waist $\lambda/\pi \times (\text{focal length}/\text{beam radius})^2 = 240$ microns. This calculated beam waist dimension is within a factor of 3 of L calculated from the Brillouin gain and that determined from ruby Thomson scattering off the ion mode, but it is misleading. As explained in Chapter 3, the focussing parabola's aberrations extended the effective beam waist to 1 mm so that the interaction region was not determined solely from the pump intensity.

Density gradients in the plasma can potentially limit the resonance zone for the instability. Inspection of Equation 2.18 shows that when $H(x) \sim 0(1)$, sufficient dephasing of the coupled waves reduces the instability gain to zero. For an assumed linearly varying wavenumber mismatch resulting from electromagnetic wave dispersion, the estimated unstable region is then:

$$L = \left(\frac{2L_n}{k_0} \frac{(1 - n/n_c)^{1/2}}{n/n_c} \right)^{1/2}$$

where L_n is the density gradient scale length. This limit on the unstable region occurs because the ion acoustic waves can propagate into plasma where they no longer

satisfy the local $2k_0$ matching with the electromagnetic wave pump. From the interferometric measurements showing $L_n = 600$ microns and $n/n_c = 0.5$, we estimate $L = 50$ microns. This interaction length is less than the 80 microns determined from reflectivity and ruby Thomson scattering measurements. It is likely that during the interaction, a number of ion modes are excited whose resonant points are axially separated. Once the plasma density gradients fix L , the heavily damped Brillouin instability convectively grows as described by the ion heating or ion trapping and heating models. In summary, ion heating and density inhomogeneity appear adequate to account for the spectral and gain length characteristics observed experimentally.

4.5.2 IML Laser Backscatter Spectra

Backscattered light observations were made with the IML CO_2 laser as a pump source. The large pump intensity range was sufficient to give a wide range of Brillouin backscatter reflectivities. Figure 4.8 shows the reflectivity as a function of laser intensity over the intensity range $1 \times 10^{12} \text{ W/cm}^2 \leq I \leq 1.7 \times 10^{13} \text{ W/cm}^2$. The nonlinear reflectivity trend can nominally be explained through ion trapping and heating. Application of the steady state model of section 2.3.2 qualitatively predicts a reflectivity minimum because ion Landau damping does not increase significantly once all the ions are trapped. The steady state ion heating model also exhibited a similar behaviour but because of the long time required to heat all the ions ($t \geq ZKT_e n_i L \omega_0 / RI \omega_s$), it was not likely to occur, at least for short interaction times and low reflectivities. The dashed line in Figure 4.8 was computed from the ion trapping and heating Equation 2.32. The best fitting plasma and interaction parameters for these results are, $\epsilon = 10^{-4}$, $ZT_e/T_i = 15$, $n/n_c = 0.3$, $\gamma_s/\omega_s = 0.3$. The large electron-to-ion temperature ratio is that of the plasma before ion heating from the Brillouin instability. The fitted curve shows higher than measured reflection. This could be in part due to the assumption that only trapped and heated ions damp the ion wave. The ion energy equipartition time is 400 ps and so some heating of all the ions can take place during the laser-plasma interaction. Increased ion Landau damping of the Brillouin ion mode would result and the measured SBS reflectivity would be lower than the theoretical estimate. Once the reflectivity begins to increase again at $I = 3 \times 10^{12} \text{ W/cm}^2$, almost all of the ions

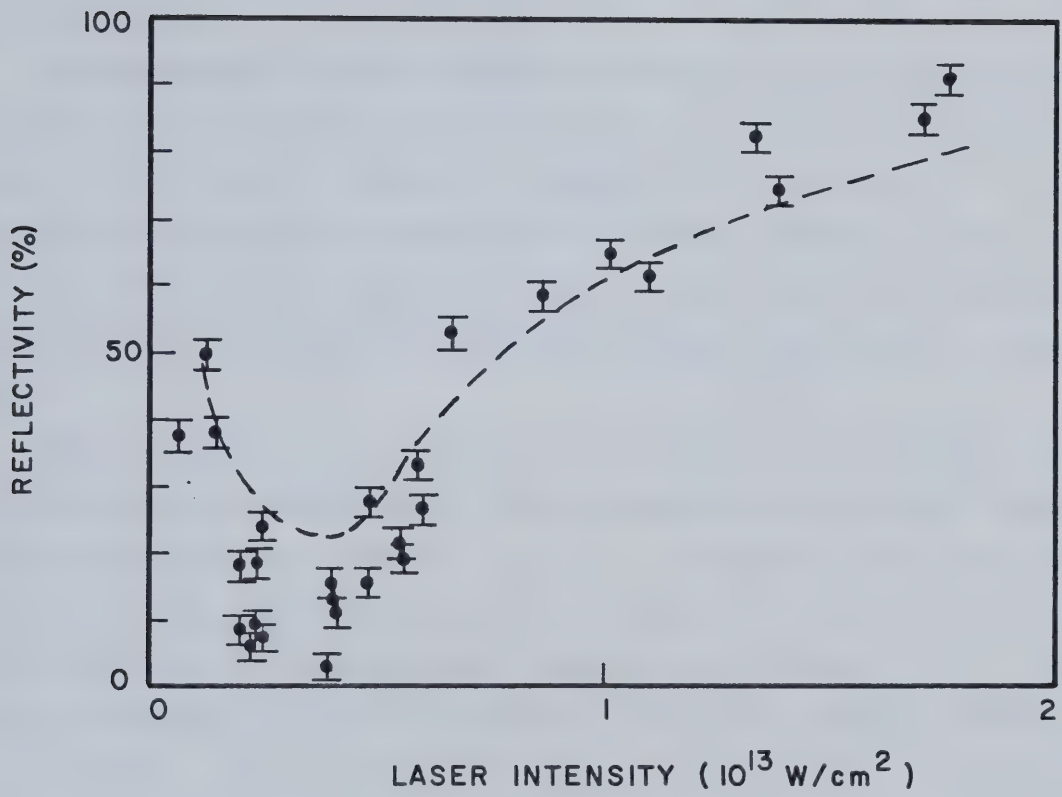


Figure 4.8 SBS Reflectivity from an IML Laser Irradiated Plasma

are trapped and ion thermal equilibration is not important. Above this pump intensity, the Brillouin ion mode density fluctuations approach unity and nonlinear effects such as wave breaking (Forslund et al. [11]) can take place. Nevertheless, reasonable agreement is shown between experiment and model calculations based on ion heating, to further limit the Brillouin instability.

The time integrated spectra of the Brillouin backscattered light was still broad as expected for ion Landau damping on the high temperature ion fraction. Figure 4.9 shows a series of infrared spectra recorded for conditions $0.1 \leq R \leq 0.53$. At these intensities, the pump level determines the instability strength and very large reflectivities were observed. Specularly reflected infrared light was not detected because the short laser pulse did not have time to ionize the gas target to critical densities.

Theoretical spectral curves were generated by the same method as those for the gain switched laser backscatter spectra. In all three theoretical spectra plotted in Figure 4.9, the electron-to-ion temperature, ZT_e/T_i , was selected to be 1. The ion temperatures corresponding to these theoretical curves are 120 eV, 240 eV and 300 eV in Figures 4.9(a), 4.9(b) and 4.9(c) respectively. Together with the measured 150 ± 20 eV electron temperature, these ion temperatures indicate a low average ionization. If

$T_i \approx 0(ZT_e)$ from ion trapping and heating, the average ionization, Z , is less than 2. However, interferometric measurements of the electron density in the IML laser irradiated plasma indicated $Z \geq 3$. This contradiction in Z suggests that the ion temperature is less than ZT_e , although a decreased T_i would not account for the backscatter spectral width. Other laser-plasma effects such as Doppler shifting from plasma motion and ion mode frequency pulling due to the intense laser pump (see section 2.2) could have contributed to altering the time integrated spectra from theoretical estimates and making their exact interpretation difficult. Also, unlike the long pulse spectra, the short pulse spectra exhibit tails to the longer wavelengths, suggesting that the differences may be related to time dependent conditions for the short pulse case.

In summary, these backscatter spectra demonstrate again the elevated ion temperatures and strong ion wave damping in the laser-plasma interaction. The quantitative agreement with our steady-state model is not as complete as time dependent

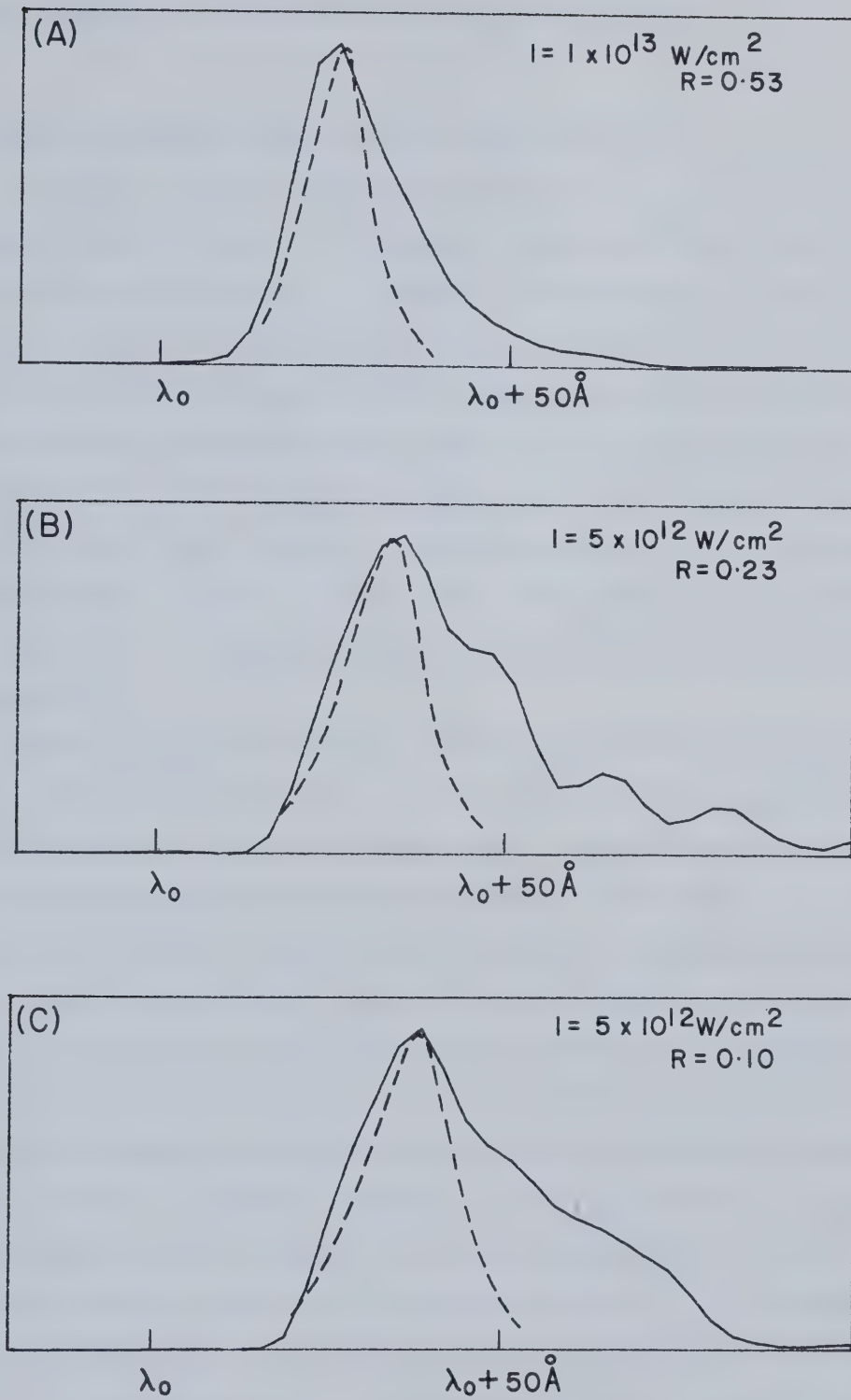


Figure 4.9 SBS Spectra for an IML Laser

effects are likely of some importance for short pulse irradiation.

4.6 Stimulated Brillouin Scattering with a Multiline CO₂ Laser

Stimulated Brillouin backscattered light levels are a direct measure of the instability's strength. In view of its practical importance in laser fusion, a series of experiments were performed in an attempt to decrease Brillouin gain and consequently reduce the amplitude of the backscattered light. As described in Chapter 3, both the gain switched CO₂ laser and the injection mode-locked laser could be induced to oscillate on two or more laser lines simultaneously. When the laser frequency separation $\Delta\omega$ was much greater than the homogeneous growth rate $\gamma_0 = (\omega_0/\omega_s)^{1/2} v_{os} \omega_{pi}/2c$, our experimental results verified the theoretical predictions of reduced SBS with increased number of lines as expected. More complex behaviour was observed when $\Delta\omega \sim \gamma_0$ for which backscattering from the various laser pump lines were not decoupled.

Brillouin backscatter reflectivities with the gain switched CO₂ laser operated both single wavelength and multiline are plotted in Figure 4.10. Average single wavelength (10.59 microns) power reflectivities were seven to ten times higher than that observed for the same total pump intensity equally distributed in 10.59 micron and 10.55 micron laser lines. The residual 2% reflectivity for more than one line did not change with three or four equal intensity lines and, moreover, showed longer temporal features than the Brillouin backscatter light. These observations indicated that this remaining light was specularly reflected from a critical density layer or steep density gradient somewhere in the plasma. This behaviour is consistent with the spectral measurements mentioned earlier as being unrelated to the Brillouin instability. The Brillouin gain reduction was greater than the algebraic reduction expected from the ion heating model. In these results the reflectivity reduction is closer to an exponential reduction $R \sim \epsilon \exp(G/N)$ when modifications due to ion heating are not incorporated. For $G = 5$, two lines result in a 12 times reduction of the reflected light. From this, it is very likely that the ion heating model is no longer valid at these reduced reflectivities since the ion heating rate is correspondingly low.

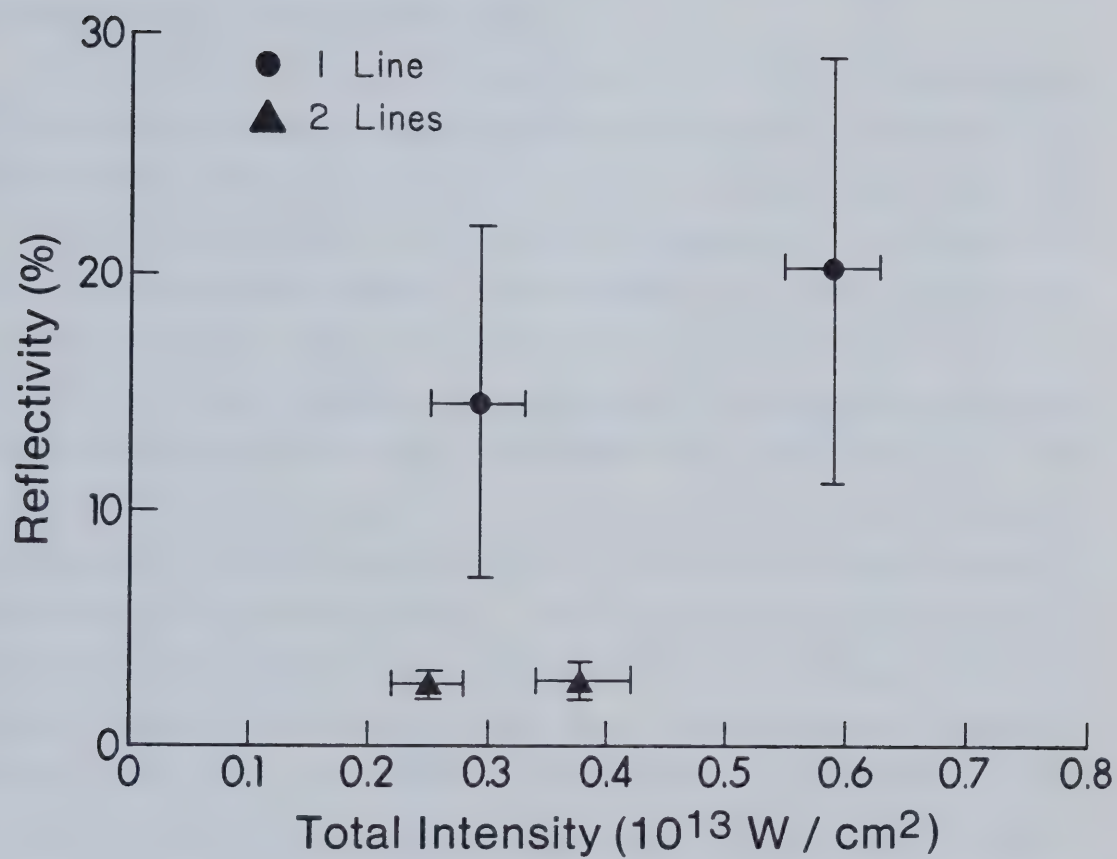
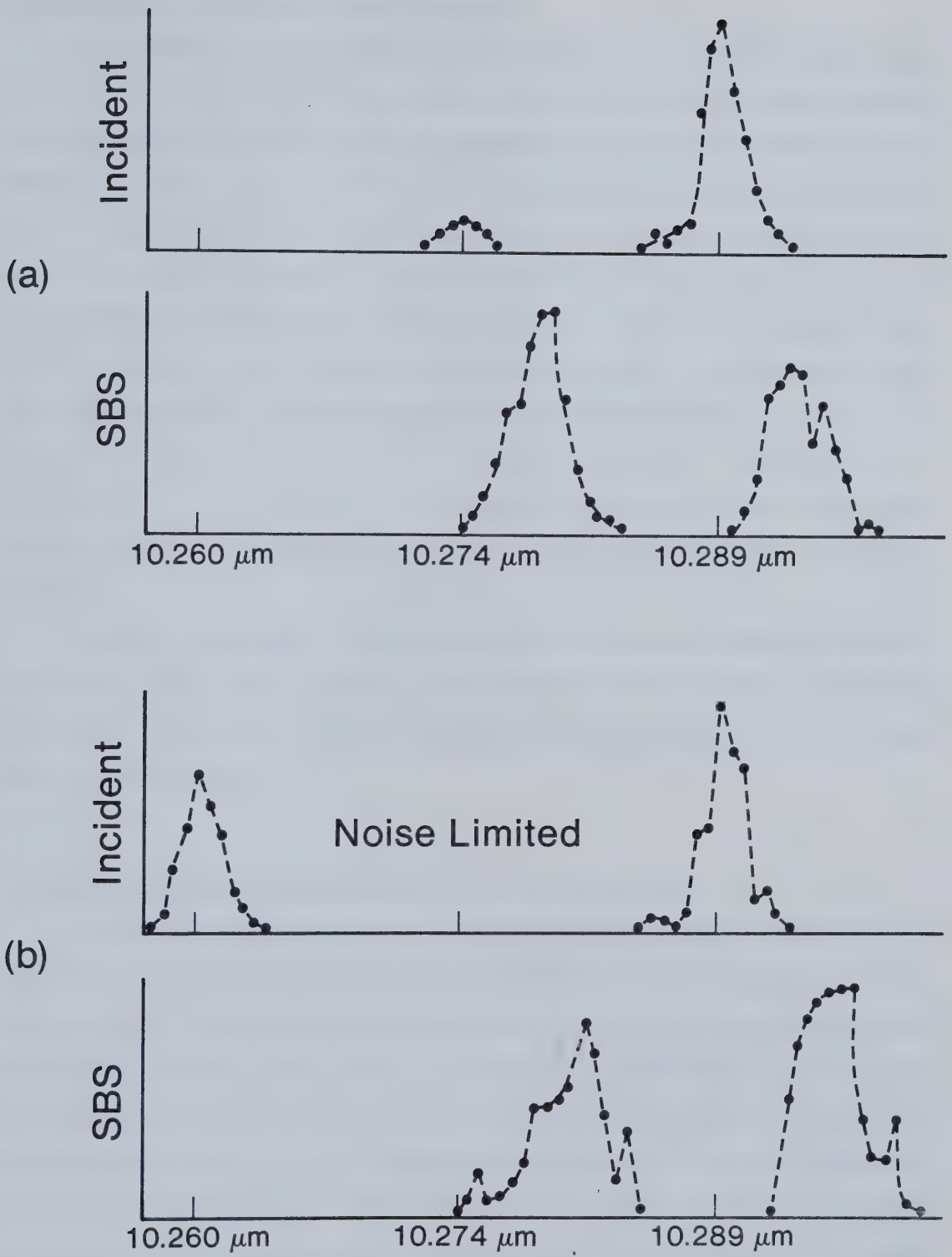


Figure 4.10 SBS Reflectivity for a Multiline Laser

In yet other experiments with a multiline pump laser satisfying $\Delta\omega \sim \gamma_0$, the SBS reduction was considerably less than above. For roughly equal line intensities at 10.289 microns and 10.274 microns for a total irradiance of 5×10^{12} W/cm², the SBS reflectivity, shared equally between the two lines, was reduced only 30% from single line lasing at 10.289 micron. The small effect of the two line irradiation on SBS in this case is attributed to the lack of wave decoupling when $\Delta\omega \sim \gamma_0$.

Further evidence of anomalous behaviour when $\Delta\omega \sim \gamma_0$ was seen when one of the laser lines was much weaker than the other. Figure 4.11(a) shows the time integrated spectral content obtained with the infrared multichannel analyser. This plot shows that the SBS reflectivity of the weaker line approached unity whereas the dominant line maintained $\approx 9\%$ reflectivity. For this particular shot, the line intensity ratio was 1:11 and the SBS ratio was 1.2:1, indicating that, within experimental error, the weak line was entirely Brillouin reflected. This suggested that the strong pump drove ion fluctuations from which the weak pump could scatter. When a third pump line at 10.26 micron was introduced, the presence of the very weak 10.274 micron line led to only moderate reduction in SBS reflectivity. In Figure 4.11(b), the laser intensity was nearly equally divided into two lines where $\Delta\omega$ was large enough to expect significant reduction in reflectivity. However, a weak 10.274 micron pump was strongly reflected as it apparently coupled to the ion modes driven by the 10.289 micron pump; consequently there was no reduction in overall reflectivity. In this example, the 10.26 micron line did not produce Brillouin scattering in spite of it being much more intense than the 10.274 micron line. This clearly shows the complex behaviour of SBS which can result with multiline irradiance when the line separation $\Delta\omega$ does not significantly exceed the homogeneous growth rate.

In order to determine whether any significant temporal differences in SBS existed for multiline irradiation, the gain-switched CO₂ laser was operated at 10.28 microns and 9.55 microns. For these widely separated frequencies, narrowband filters and two Ge:Au detectors were used to monitor the individual laser lines or their associated Brillouin backscatter. As expected for these two widely separated lines ($\Delta\omega = 1.4 \times 10^{13} \text{ s}^{-1} \gg \gamma_0$), the reflectivity was greatly reduced. Within the 2 ns instrumental resolution, both lines exhibited identical characteristics in input and

Figure 4.11 Multiline CO₂ Laser Backscatter Spectra

SBS reflection characteristics, thus precluding scattering from the different lines at different times during the laser-plasma interaction.

Finally, SBS reflectivity measurements were made with the injection mode-locked CO₂ laser to verify similar SBS reduction for short laser pulses. Unfortunately, additional laser cavity losses from the intracavity SF₆ absorption cell lowered the available focussed intensity to a region where the SBS reflectivity was already low. A maximum intensity of $2.8 \times 10^{12} \text{ W/cm}^2$ was achieved from which a single line (10.289 micron) reflectivity of $2.0 \pm .3\%$ was found. With the same total intensity in two lines (10.289 micron and 10.274 micron), the reflectivity was reduced to $1.2 \pm .6\%$ and the three line (10.289, 10.274 and 10.260 micron) reflectivity was decreased to $0.5 \pm .1\%$. As with the gain switched laser results, it was likely that the reduction of SBS reflectivity was somewhat moderated because of the small frequency separation ($\Delta\omega = 2.6 \times 10^{11} \text{ s}^{-1}$, $\gamma_0 = 10^{12} \text{ s}^{-1}$). Nevertheless, these observations were again consistent with the expected reduction of Brillouin backscatter reflectivity for a multiline laser pump.

In summary, a dramatic reduction in Brillouin reflectivity has been observed for long pulse multiline laser irradiation of a plasma. This is the first experimental demonstration of this very effective method for virtually eliminating the Brillouin process in a laser-plasma interaction.

4.7 Ruby Thomson Scattering Measurements of SBS Ion Modes

The Brillouin instability excites both electromagnetic and electrostatic waves in a plasma. The backscattered light has been analysed showing the essential details of the instability, that is, ion trapping and heating along with convective growth and plasma inhomogeneity moderating the growth rates and saturation levels. Here, the ion acoustic wave is examined directly to further clarify the behaviour of the instability. The diagnostic method employed was ruby laser Thomson scattering, which has been described in Chapter 3. Scattered ruby laser light was detected with either an Optical Multichannel Analyser for time integrated spectral measurements, a photomultiplier for average scattered light measurements and absolute fluctuation level determination, or a high speed streak camera for temporal details of the ion wave k spectrum and its spatial

distribution in the plasma.

4.7.1 Determination of Absolute Level of Ion Fluctuations

Probably the most convincing evidence for the existence of a heavily damped convective instability was obtained from the photomultiplier scattered light measurements. By determining the ion mode fluctuation level for known pump intensity and backscatter reflectivity, an effective damping constant was found which directly demonstrated strong damping. The observed simple functional dependence of the ion fluctuation level on reflectivity, $\delta n/n \propto \sqrt{R}$, was the signature of heavy ion wave damping. The ion fluctuation level $\delta n/n$ was calculated from the Thomson scattered light power.

Calibration of the detector response was made with a tungsten filament blackbody source positioned at the CO₂ laser focus. Figure 4.12 shows the two lens scattered light collection used in the photomultiplier detection system. The tungsten ribbon filament was placed at the parabola's focus and oriented normal to the collection axis. The blackbody emitting area was determined with an iris located between the two lenses. Once the filament temperature T was measured with an optical pyrometer, the blackbody source light reaching the detector could be calculated from

$$P = I(\lambda, T) A \, d\Omega \, d\lambda$$

where I , the blackbody emissivity is

$$I(\lambda, T) = (2hc^2/\lambda^5) \epsilon(\lambda) [\exp(c_2/\lambda T) - 1]^{-1} \text{ erg}/\text{\AA} \, \text{s} \, \text{cm}^2 \, \text{sr}$$

$$c_2 = 1.438 \text{ } ^\circ\text{K cm}$$

$$\epsilon = 0.43 \text{ for Tungsten at } 6943 \text{ \AA}$$

and A is the effective emitting area, $d\Omega$ the collection solid angle and $d\lambda$ was the detection bandwidth. Here $d\lambda = 4 \text{ \AA}$ was determined by a narrow

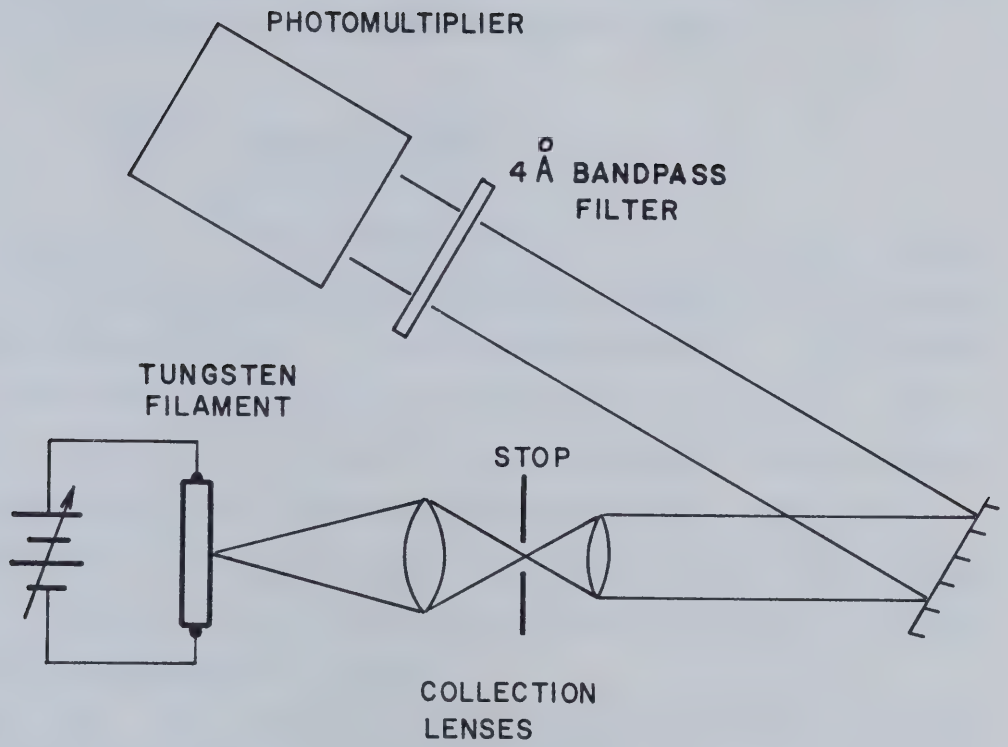


Figure 4.12 Blackbody Calibration of Thomson Scattering Photomultiplier Detector

bandpass filter located in front of the photomultiplier. This calibration together with the known attenuation introduced to obtain linear response to scattered light signals allowed absolute Thomson scattered power levels to be calculated.

The scattering form factor $S(k)$ which is related to the ion fluctuation level $|\delta n|^2$ could be deduced from the Thomson scattered power

$$S(k) = P_{\text{scattered}} / I n_e V \sigma_e d\Omega^*$$

where $P_{\text{scattered}}$ is the scattered light power, n_e the plasma electron density, V the scattering volume estimated from the intersection of the ruby probe beam and the Brillouin active region, I the probe beam intensity, σ_e the Thomson scattering cross section ($8.8 \times 10^{-26} \text{ cm}^2$). The scattering solid angle $d\Omega^*$ was not necessarily the same as $d\Omega$, the collection optics solid angle. As will be discussed later, the k spectral width of ion fluctuations was measured to be $\Delta k/k = 0.20$, which translated into a small angular spread of ± 0.6 degrees in the scattered light. Consequently, the effective Thomson scattering solid angle at the first collection lens was less than the available collection solid angle.

Once $S(k)$ was calculated, the fluctuation level, $\delta n/n$ could be determined from the Thomson scattering theory result [58]:

$$\frac{\delta n^2}{n^2} = \left(\frac{1}{2\pi} \right)^3 \left(\frac{2}{n_e} \right) \int S(k) k^2 dk$$

If $S(k)$ is assumed to vary slowly over the wavenumbers of interest, then defining $(2 - \Delta)k_0 < k < (2 + \Delta)k_0$ where Δ is a measure of the k spectral width, we have:

$$\frac{\delta n^2}{n^2} \approx \frac{16\Delta}{\lambda^3 n_e} S(k)$$

where λ is the wavelength of the CO_2 laser light inducing the collective ion fluctuation.

The experimental results for an average gain switched CO₂ laser intensity of 3×10^{12} W/cm² are plotted in Figure 4.13 as $(\delta n/n)^2$ versus backscattered light reflectivity, R . The ion fluctuation level is seen to be linearly related to the backscatter reflectivity as expected for a strongly damped convective instability. In steady state, Drake et al [9] have shown that $\delta n/n$ is related to the ponderomotive force by

$$\frac{\delta n}{n} = \frac{-k^2}{8\pi n_e m_e \omega_0^2} \frac{x_i x_e}{(1 + x_i + x_e)} \frac{\mathbf{E}_0 \cdot \mathbf{E}_0}{2}$$

which reduces (as shown for the coupled mode equation calculations of Chapter 2) to

$$\frac{\delta n}{n} = \frac{1}{2} \left(\frac{v_{os}}{v_e} \right)^2 \frac{\omega_s}{2\gamma_s} \sqrt{R}$$

From these equations and a curve fit to the results in Figure 4.13, the damping coefficient, γ_s/ω_s , was estimated to be 0.3. The solid line in Figure 4.13 is the fitted curve. This large damping coefficient is still less than $\gamma_s/\omega_s \sim 0.6$ which was estimated from the Brillouin backscatter spectra. It is difficult to isolate the reasons for the different damping coefficients although it must be realized that all the models used to obtain these figures are approximate. Possibly the lower reflectivity ($R \sim 10\%$) in these results account for less heating and a lower γ_s . In any case, both these damping coefficients are the result of Brillouin induced ion heating and ion Landau damping of the ion acoustic waves.

4.7.2 Spatially Resolved Thomson Scattering

The remaining Thomson scattering experiments used the high speed streak camera for light detection. The streak camera not only had the advantage of providing up to 10 ps temporal resolution, but the multichannel detection capability allowed streaking of either spatially imaged, wavenumber resolved or wavelength resolved Thomson scattered light. Each of these measurements will be discussed here. In the first two arrangements, a two lens telescope was used to relay Thomson scattered light to the

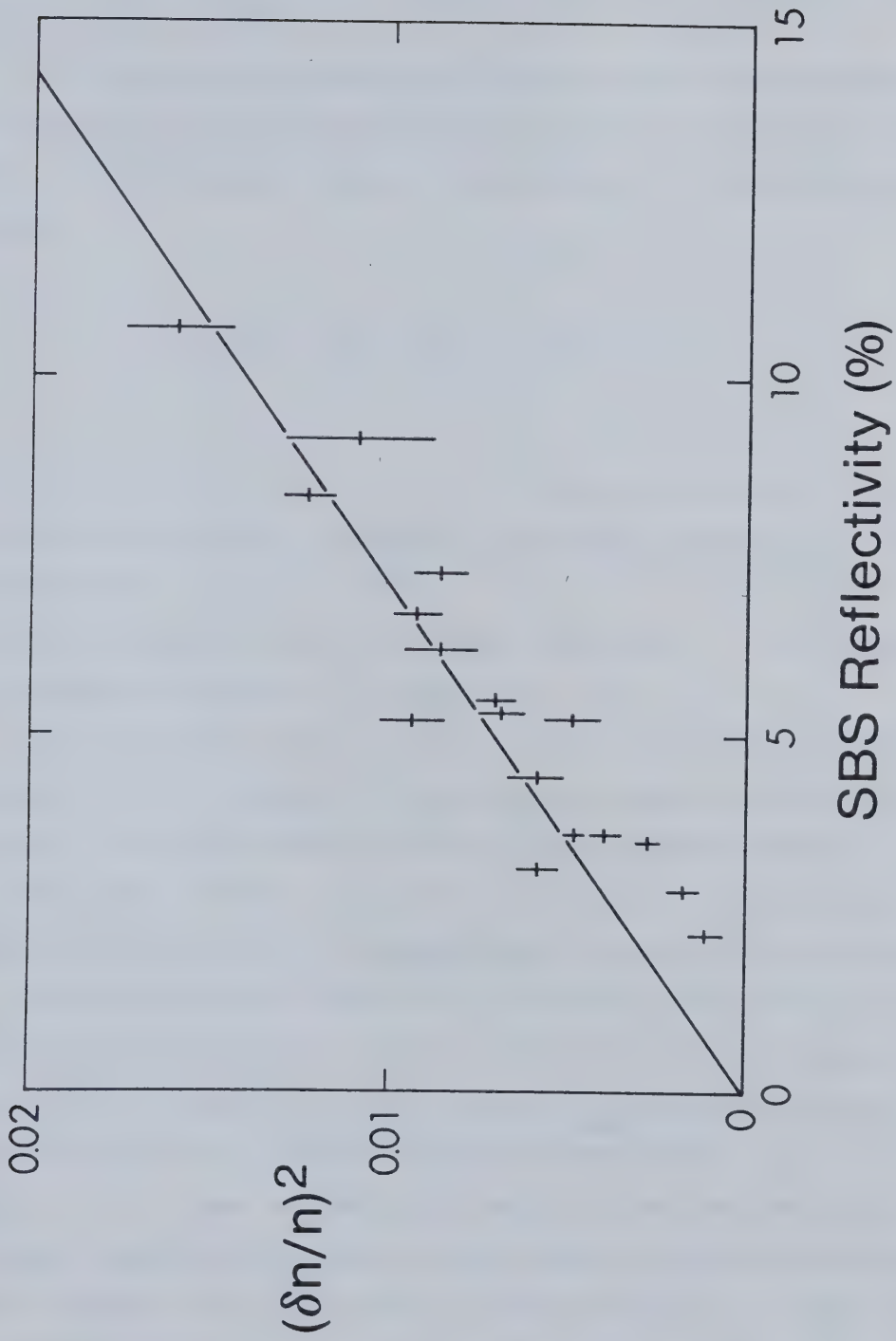


Figure 4.13 SBS Ion Fluctuation Levels Determined from Thomson Scattering

streak camera slit. For spectral measurements, the light was dispersed through an E1 monochromator located at the focus of the second lens and its output was imaged onto the streak camera slit with a third lens.

The length of the stimulated Brillouin scattering zone is an important parameter in describing the instability. The infrared backscattered light levels have been analysed from which an interaction length is inferred. A rough estimate of L from the Bragg reflectivity relation is

$$(L/\lambda)^2 = R/[(\pi/2)^2(n/n_c)^2(\delta n/n)^2]$$

Here the ion fluctuation $\delta n/n$ is not self consistently calculated from the coupled mode equations, but rather is determined experimentally. With the gain switched CO_2 laser parameters, this equation implied $L/\lambda = 3$ for $(\delta n/n)^2 = 0.02$ which is much smaller than both the CO_2 laser focal depth (500 micron) and the density gradient scale length ($L_n = 600$ micron).

Ruby Thomson scattering from the Brillouin driven ion modes allowed direct measurement of the stimulated Brillouin interaction length as well as the fluctuation distribution. The $f/10$ focussing optics' 6 micron resolution limit did not interfere significantly with the spatial imaging. For both the gain switched CO_2 laser and the injection mode locked laser, the average interaction region FWHM was measured to be 80 ± 20 microns although a range from 50 microns to 160 microns was seen for different laser shots. Figure 4.14 illustrates a streak camera plot (relative scattering levels only), of SBS ion fluctuations in a gain switched CO_2 laser-plasma interaction. Thus the directly measured value is greater than either the inhomogeneous $L \sim k^{-1/2}$ or the Bragg L but is less than the optical depth. This gain switched laser result was particularly interesting in that it had two intensity peaks 1 ns after the most intense phase of the interaction. This is supportive of density gradients or at least axial density nonuniformity determining the instability zone. The spatial density fluctuation distribution at the time of most intense scattering is qualitatively similar to the damping calculation of section 2.3.2. It must be remembered that the wavenumber dephasing from a density

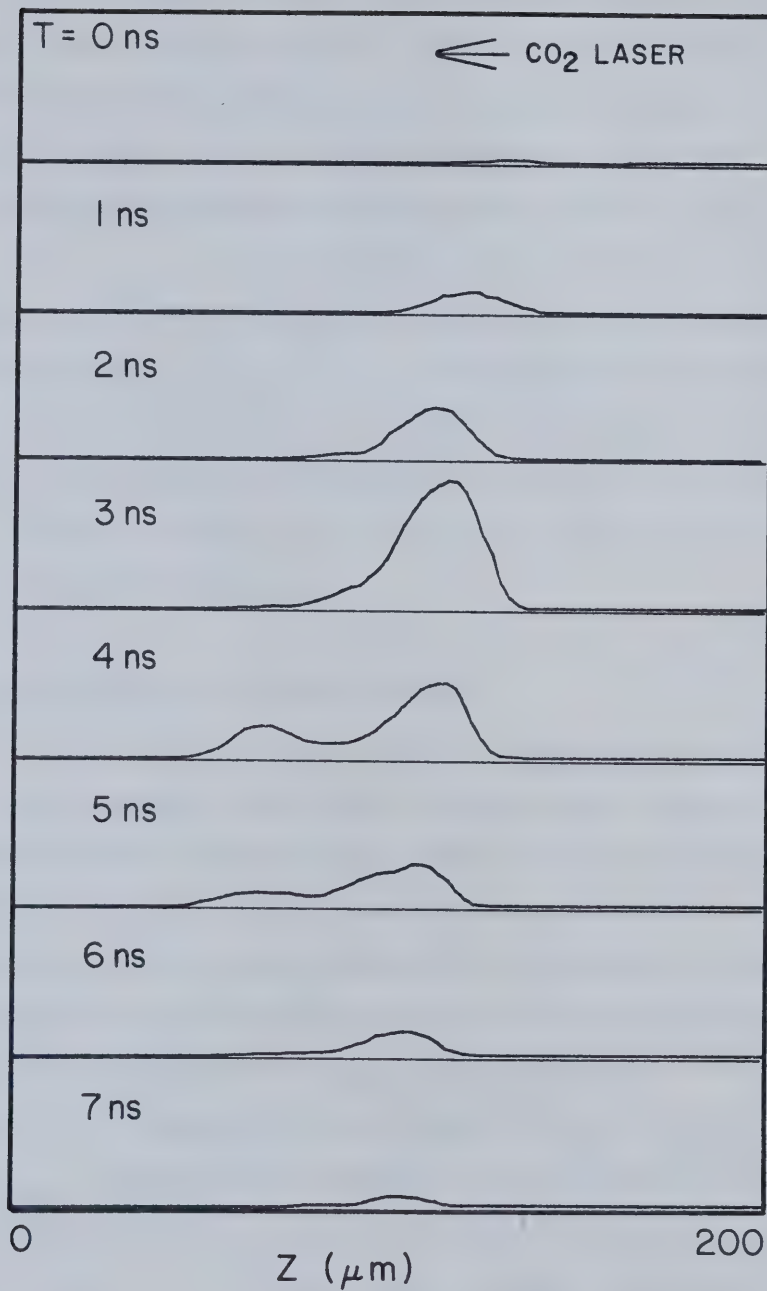


Figure 4.14 Time Evolution of the Spatial Distribution of SBS Ion Fluctuations (Gain switched Laser)

gradient alters the coupling coefficients in the coupled mode equations. Two examples of the ion fluctuation spatial distribution for an IML laser pump are illustrated in Figure 4.15. The two plots show the observed variation in the interaction length. The most significant difference between these results and those obtained for the gain switched laser is the shorter time duration of the ion fluctuations.

The 80 micron average spatial dimension of the scattering region corresponds to $\zeta = 15$ in the steady state, WKB spatial solution of Equation 2.20. For the laser and plasma conditions, the corresponding normalized damping, β is ≈ 10 from which one infers $\gamma_s/\omega_s = 1$. This anomalously large damping figure is probably due to inexact determination of the laser pump intensity in the interaction zone. In any case, the large ion wave damping inferred confirms the convective gain model concluded from SBS reflectivity and backscattered light spectra as well as time integrated Thomson scattering results.

4.7.3 SBS Ion Acoustic Fluctuation Wavenumber

The ion fluctuation calculation from the photomultiplier results required an estimate of the wavenumber distribution. This figure was obtained from the streak camera measurements of the wavenumber resolved Thomson scattered light. The streak camera entrance was moved away from the second lens focus of the collection telescope used in the spatial imaging experiment. As discussed in Chapter 3, the light detected across the streak camera slit was proportional to the Thomson scattering angle. From Thomson scattering theory, $k_{ion} \approx 2k_{ruby} \sin\theta/2$ or for the small scattering angle θ probing Brillouin fluctuations, $k_{ion} \approx k_{ruby} \theta$. Hence the ion wavenumber k_{ion} was immediately calculated from the scattering angle measurement. A typical wavenumber spectrum is plotted in Figure 4.16. The wavenumber width, $\Delta k/k_{ion} = 0.15$ in this case is slightly lower than the average, $\Delta k/k_{ion} = 0.20$. The scattering angle was reduced from the 7.5 degrees calculated for k corresponding to the vacuum CO_2 laser wavelength because of the plasma refractive index, i.e.

$$k \approx 2\omega_0 \sqrt{1 - n/n_c} / c$$

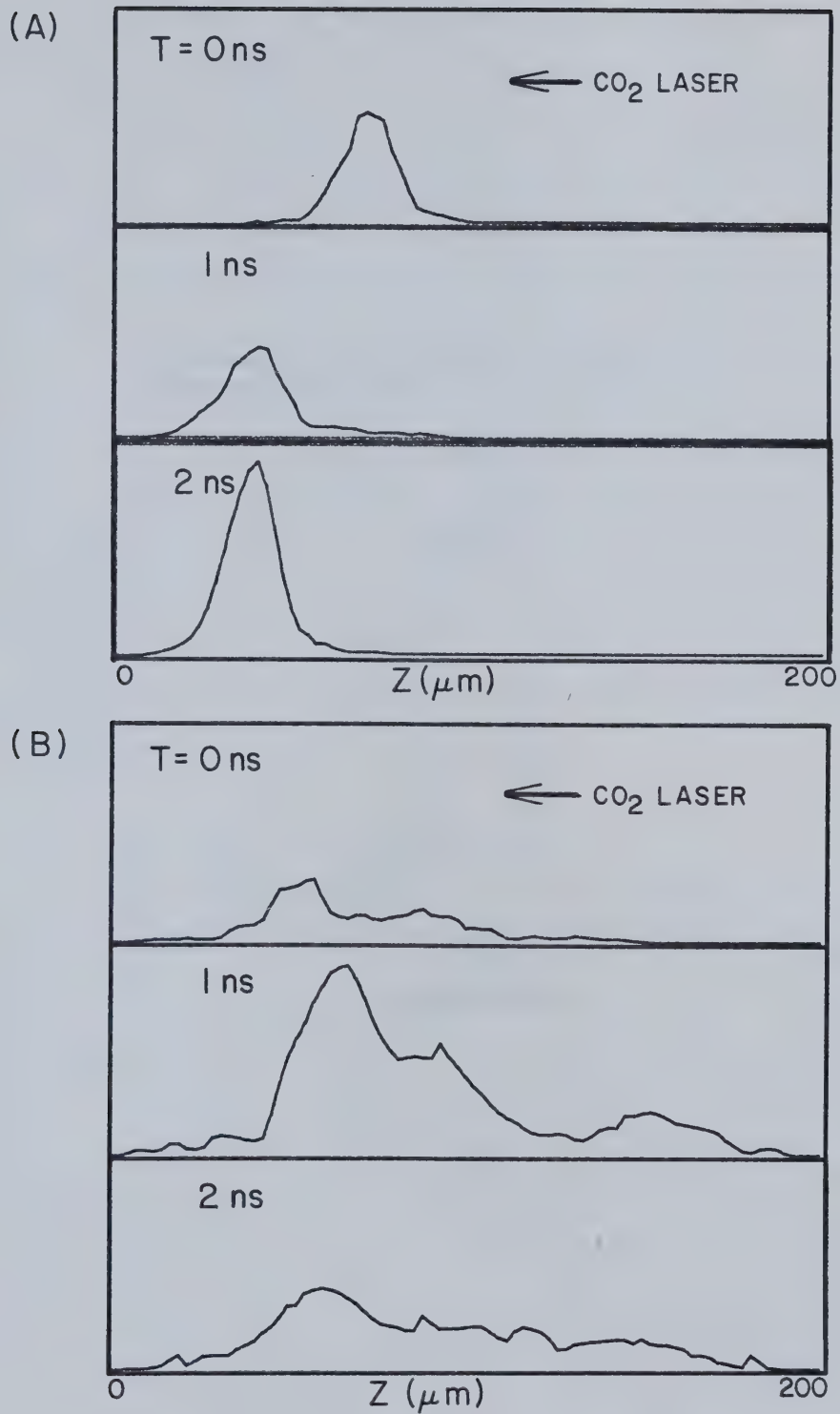


Figure 4.15 Time Evolution of the Spatial Distribution of SBS Ion Fluctuations (IML Laser)

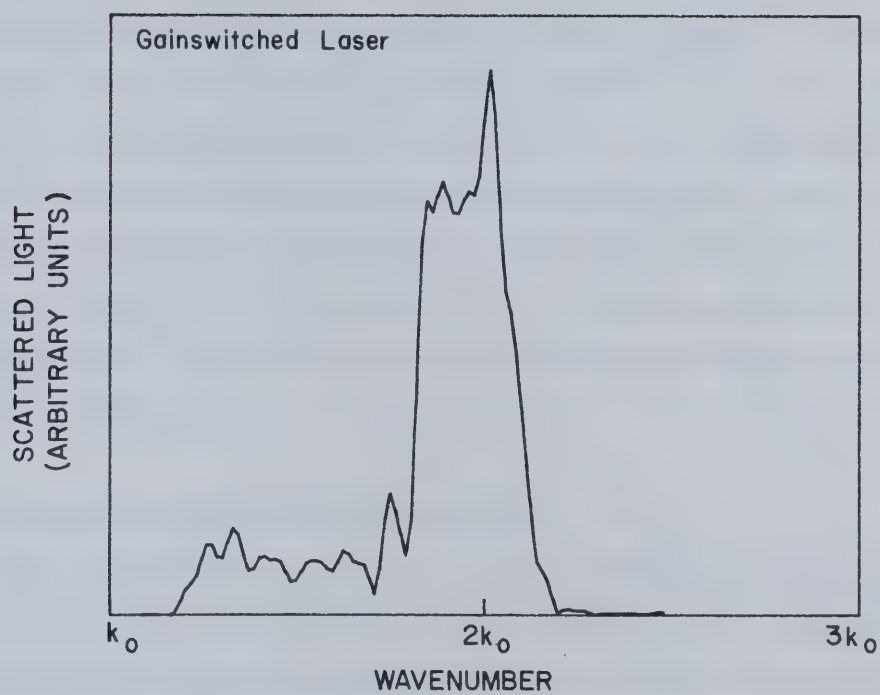


Figure 4.16 Wavenumber Spectrum of SBS Ion Fluctuations Determined from Thomson Scattering

A more careful calibration of the absolute scattering angle would evidently allow the plasma density in the Brillouin instability region to be calculated.

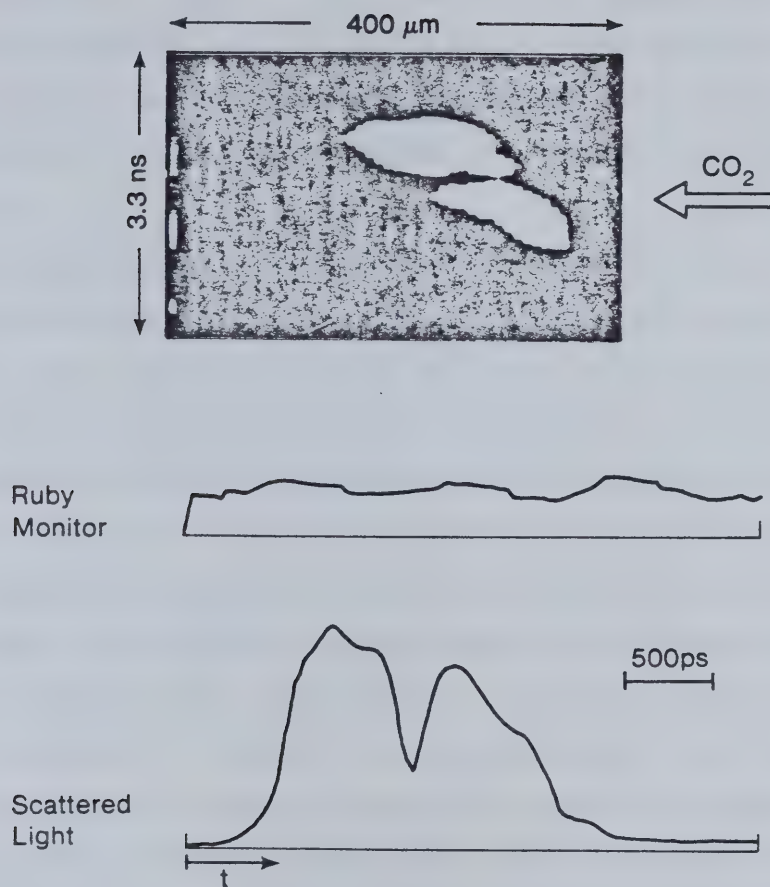
A significant observation also made was that no subharmonics (k_0) or harmonics ($4k_0$) were detected with the pump levels used in this experiment,

$I \leq 6 \times 10^{12} \text{ W/cm}^2$ even though saturated Brillouin backscatter levels of 10 to 20% occurred. Either of these harmonic fluctuations, if excited by the Brillouin decay products could act to saturate the instability [59] [60]. This absence of harmonic ion waves contrasts sharply with experiments of Walsh and Baldis [61] where $4k_0$ was seen even for 6 to 10% saturated backscatter reflectivity with a short pulse CO_2 laser pump. Both lower pump intensities and higher ion wave damping can explain the difference in results, though the stronger damping is a more likely cause. This result again confirms the heavy ion wave damping of the present experiments. The absence of subharmonic spectra rules out secondary ion wave decay as a saturation mechanism in this case as well. This too was consistent with the large ion wave damping since decay requires $\delta n/n \geq \gamma_s/\omega_s$.

4.7.4 Temporally Resolved SBS Ion Fluctuations

The 10 ps temporal resolution of the Hamamatsu streak camera allowed accurate determination of the Brillouin instability growth as well as decay along with the observation of high frequency fine structure, if present. Figure 4.17 shows typical streak camera results of the spatially imaged Thomson scattered light with a gain switched CO_2 laser pump. These figures illustrate the monotonic growth of the ion acoustic fluctuation level which over many shots showed growth periods of 150 to 700 ps with an average of 500 ps. The instability decayed in similar periods. The absence of exponential growth in time or rapid modulation in the Thomson scattered light was clear evidence for strong ion wave damping appearing well ahead of the peak ion fluctuation level. The scattering risetime was less with the IML CO_2 laser pump (average risetime ≈ 400 ps) and again did not show rapid modulation. This temporal behaviour was confirmed over a detection dynamic range of better than 10,000, obtained by using different neutral density filters to attenuate the Thomson scattered light and by changing the camera streak speed.

• (A) 3.3 ns Streak



(B) 1.3 ns Streak

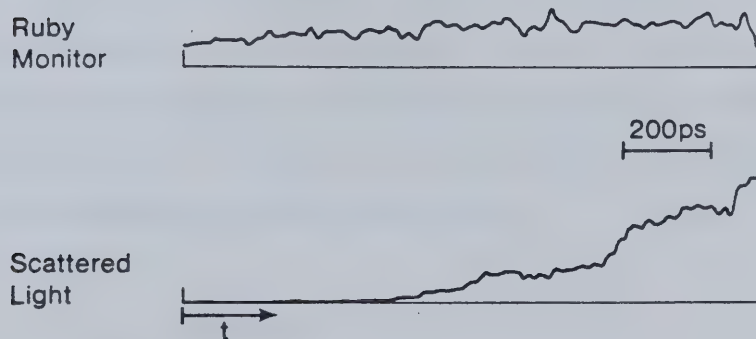


Figure 4.17 SBS Ion Fluctuation Growth (Gain Switched Laser)

The homogeneous growth rate γ_0 gives a risetime of 1 ps, or for heavy damping, simple convective gain calculations give a risetime estimate of $GL/c \approx 12$ ps which are far too rapid for the observed signal growths. The more detailed convective growth rate calculations from the coupled wave equations in section 2.3.3 also do not seem to apply to the above observations except that the lack of any oscillation in the ion fluctuation level is qualitatively consistent with the strongly damped wave calculation.

On the other hand, ion trapping and heating is a wave energy sink that can account for the slow rise to saturation. As the ion wave amplitude grows, energy is expended in trapping and heating ions. From balancing the fraction of the incident pump energy imparted to the ion acoustic wave and thereby to the trapped ion energy, a growth rate can be calculated. In this model, the instability convectively saturates to levels determined by ion Landau damping and/or plasma inhomogeneity. Now, Kartunnen and Heikkinen [62] previously demonstrated, by solving the coupled mode equations including wave damping through trapping, that the saturated instability levels were unaffected by trapping, even though the growth rates were. Their formulation did not include other wave damping or account for wavenumber mismatches in inhomogeneous plasma. Conversely, Rosenbluth et al [7] who solved the equations including both plasma inhomogeneity and wave damping but ignored ion trapping, did not find a reduced growth rate to saturation of the instability. Furthermore both of these models did not allow for increased ion Landau damping on the trapped and heated ions.

Such a model is proposed here. A steady state solution to this problem was derived earlier in Chapter 2. A rough estimate of the Brillouin instability temporal growth was made from the energy balance which ignored ion convection and trapping dynamics. Three equations were used to obtain an expression relating the trapping velocity width and the Brillouin backscatter reflectivity. These were

$$v_{tr} = \sqrt{2Ze\phi/M_i}$$

$$\delta n/n = e\phi/T_e$$

$$\delta n/n = 0.5(v_{os}/v_e)^2(\omega_s/2\gamma_s)\sqrt{R}$$

Eq. 4.1

all of which have been introduced earlier. Eliminating ϕ and $\delta n/n$ in these equations gives

$$v_{tr} = (v_{os}/v_e) \sqrt{ZT_e/M_i} \sqrt{\omega_s/2\gamma_s} R^{1/4}$$

Next, the net energy, dE_T expended to accelerate (and decelerate ions) to c_s upon trapping them is determined from

$$\begin{aligned} dE_T = & f(c_s - v_{tr}) (M_i c_s^2/2 - M_i (c_s - v_{tr})^2/2) dv_{tr} \\ & - f(c_s + v_{tr}) (M_i (c_s + v_{tr})^2/2 - M_i c_s^2/2) dv_{tr} \end{aligned} \quad \text{Eq. 4.2}$$

Integrating the right hand side of this equation gives the total energy E_T absorbed by the trapped ions. A Maxwellian distribution is assumed for f and the trapping velocity v_{tr} is normalized to $v_{tr} = c_s V$. With these assumptions, Equation 4.2 reduces to

$$\begin{aligned} E_T = & \sqrt{1/2\pi} n (ZT_e + 3T_i) (ZT_e/T_i + 3)^{1/2} \cdot \\ & \int_0^{v_{max}} \{ V[(2 - V) \exp(-ZT_e/2T_i - 3/2)(1 - V)^2 - \\ & (2 + V) \exp(-ZT_e/2T_i - 3/2)(1 + V)^2] \} dV \end{aligned} \quad \text{Eq. 4.3}$$

$$v_{max} = (v_{os}/v_e) \sqrt{\omega_s/2\gamma_s} \sqrt{ZT_e/(ZT_e + 3T_i)} R^{1/4}$$

The available ion wave energy is a small fraction of the incident electromagnetic wave energy. If the backscatter reflectivity grows linearly from 0 to R , the energy available to the ion waves in a time τ can be approximated as

$$E_W = IR\omega_s \tau / 2L\omega_0 \quad \text{Eq. 4.4}$$

Equating E_W to the energy delivered to the trapped ions allows the risetime τ to saturation to be estimated. Figure 4.18 shows the results of such risetime calculations for various experimental parameters of interest. What is illuminating is that if steady state reflectivity R increases, the risetime does not diminish proportionately because even though more energy goes into ion waves, more ions are trapped and heated. Also, it is clear that lower density plasmas have fewer available ions to trap and heat and the risetime decreases. In the case of the short pulse CO_2 laser pump where lower electron densities were measured interferometrically, faster instability risetimes were detected. Even with this crude model, the estimated time scales are close to those observed experimentally and qualitatively substantiate the differences between injection mode locked and gain switched CO_2 laser pumps. Incidentally, as the instability growth rate is $\propto n_e k_0$, one would expect the high density plasma with the gain switched CO_2 laser to exhibit faster risetimes. The opposite trend gives further credence to the ion trapping and heating picture presented here, at least until ion wave convection occurs. The characteristic time scale for this convection would be $\tau_{\text{conv}} \approx L/c_s$, which is much longer than the instability risetimes.

4.7.5 Wavelength resolved Thomson Scattering

The final Thomson scattering experiment was undertaken to measure the frequency spectrum of the scattered light. Unfortunately, time broadening through the monochromator made high speed streaks unuseable. Instead, time integrated scattering measurements were made with the PARC Optical Multichannel Analyser. Absolute wavelength calibration was difficult to achieve because of the small wavelength shifts from λ_0 which were present, although the instrumental resolution (0.4 \AA) was sufficient to observe the scattered line width after deconvolution. Figure 4.19 shows a typical Thomson scattered light spectrum when the gain switched CO_2 laser irradiated the oxygen plasma ($I = 5 \times 10^{12} \text{ W/cm}^2$). For comparison, the 0.30 \AA spectral FWHM can be correlated with the infrared backscattered light spectral width. From Thomson scattering theory, $d\lambda_r/\lambda_r = dv/c \cdot \theta$ where $d\lambda_r$ is the scattered ruby light spectral width and dv is the spread in the ion wave phase velocity. The Brillouin ion mode wave number is $2k_0$, so the frequency spread in

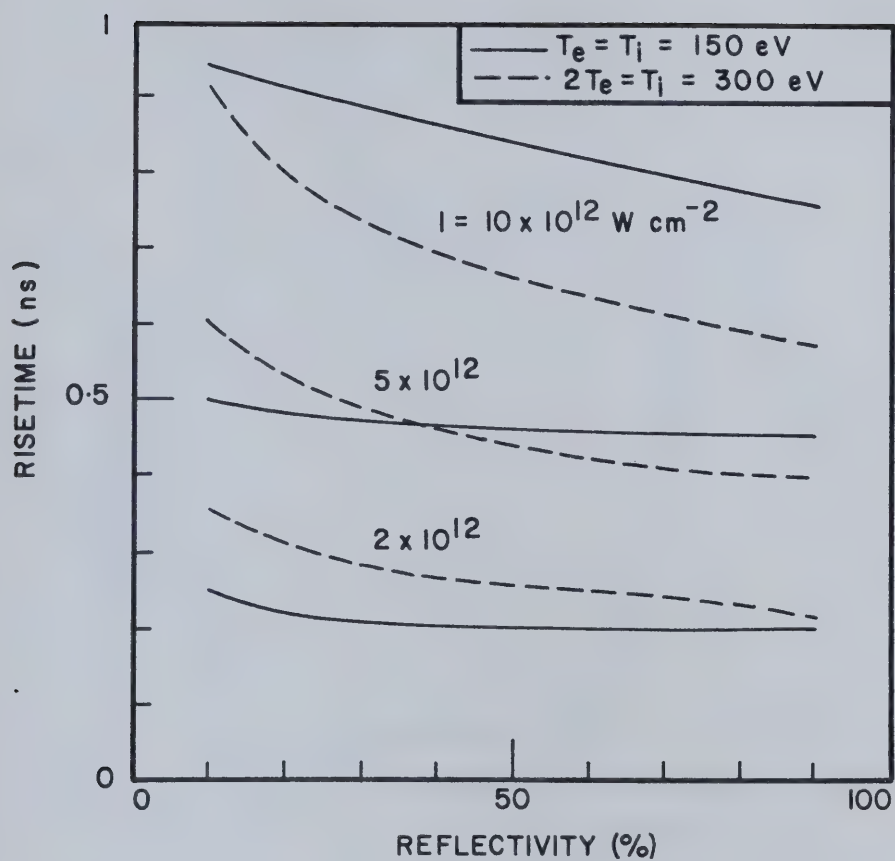


Figure 4.18 SBS Riset Time Estimates from Ion Trapping

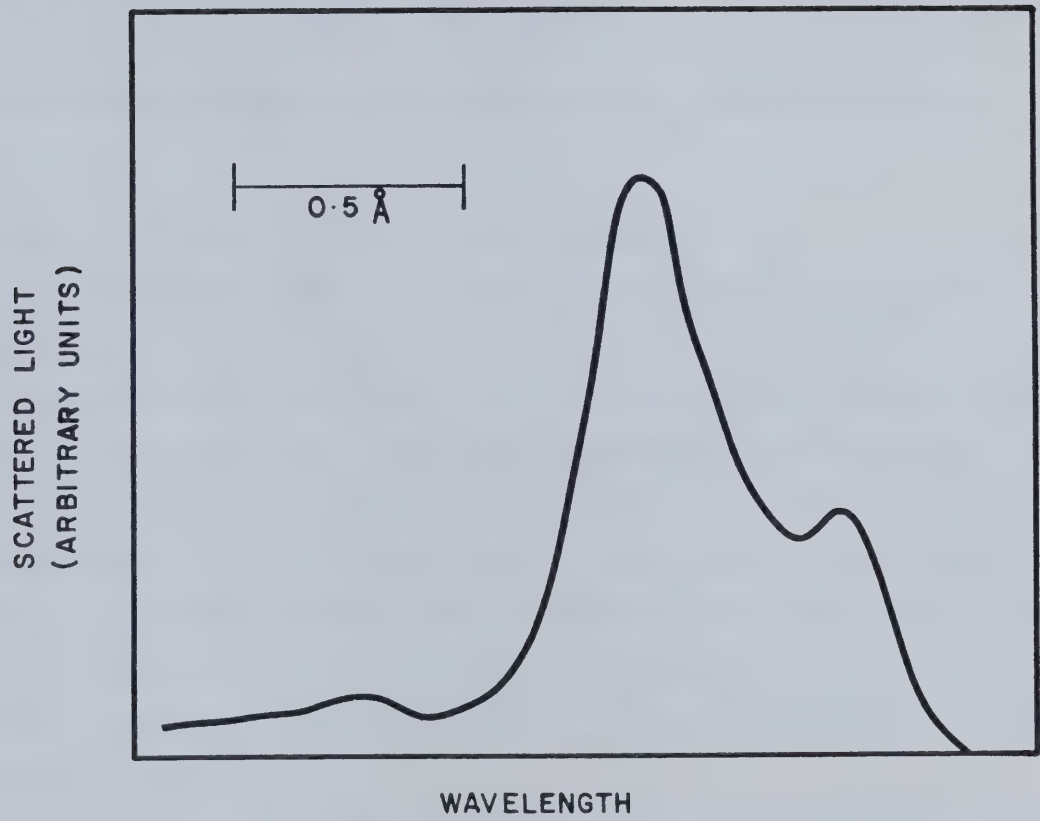


Figure 4.19 Time Integrated Thomson Scattered Light Spectrum

the infrared backscattered light is $2k_0 dv$ and the corresponding wavelength spread is $d\lambda = (2\lambda_0/\theta) \cdot (d\lambda_r/\lambda_r)$. Thus for the 0.30 Å Thomson scattered light spectral width, one expects a 70 Å infrared backscattered spectral width. This estimated $d\lambda$ is larger than the directly observed 30 Å average backscattered light spectral width. It is likely that $d\lambda$ was overestimated since the Thomson scattering detection instrumental width was larger than $d\lambda_r$. In any case, the Thomson scattered light spectral width again indicates strong ion wave damping.

4.8 Termination of SBS in the Laser-Plasma Interaction

The fundamental question still remains as to what caused the stimulated Brillouin scattering to terminate well ahead of both the IML and gain switched laser pump. Interferometry showed that the plasma was still sufficiently dense to provide a high gain medium and no anomalous density structure such as profile steepening was seen. Pump cutoff through critical layer reflection was also unlikely since the Brillouin backscattered light ceased even with 0 Torr helium background gas where underdense plasma was assured. The remaining possibilities include filamentation with resultant electron heating, increased pump absorption through enhanced ion turbulence or inverse bremsstrahlung absorption, large velocity gradients resulting in wave phase mismatch or plasma susceptibility changes.

Filamentation occurs when transverse pump inhomogeneities intensify and the pump wave is channelled into a number of high intensity filaments. This happens because the incident light beam's ponderomotive force on the plasma electrons $f_p = -(e^2/2m_e\omega_0^2)\nabla\langle E^2\rangle$, drives the electrons from the region of highest pump intensity. The resulting refractive index change focusses the laser light to create even higher local pump intensities to reinforce the original pump inhomogeneity. Although the light intensity is higher due to filamentation, the decreased plasma density and elevated electron temperature can result in an overall reduction of the Brillouin gain.

When $ZT_e/T_i \gg 1$, the convective Brillouin growth rate is much larger than that for filamentation. However, from the results discussed in this chapter, the ions can be significantly heated to Landau damp the ion modes associated with Brillouin scattering (this is often called Compton scattering). In this case filamentation can compete

with Brillouin scattering. The maximum filamentation growth occurs for $\underline{k}_{\parallel} = 0$ and

$$k_{\perp}^2/k_0^2 = (n/4n_c)(v_{os}/v_e)^2(1/(1 + T_i/ZT_e))$$

where $\underline{k}_{\parallel}$ is the filament wavenumber parallel to \underline{k}_0 and \underline{k}_{\perp} is the perpendicular component [12]. The spatial growth rate of the filament for large damping is

$$\text{Im } k_{\parallel} = \sqrt{1 - n/n_c} (\omega_{pe}^2/8\omega_0 c)(v_{os}/v_e)^2(1 + T_i/ZT_e)$$

Since the density fluctuation wavenumbers associated with filamentation are not normal modes, these growth rates are not diminished by increased Landau damping as they are for the Brillouin instability. Brillouin scattering has a spatial growth rate larger by $\sim (\omega_s/2\gamma_s)$ which means that for heavy damping, the growth rates of the two instabilities are comparable. For $n/n_c = 0.5$, $(v_{os}/v_e)^2 = 2$, $T_i = ZT_e$, the optimum filament transverse dimension is 30 microns which indicates that if a single filament forms (whole beam self focussing), the local pump intensity can increase tenfold over the usual focal spot intensities. Density rarefaction in the filament through the ponderomotive force will act to decrease the Brillouin gain and also the filament transverse dimension as calculated above, will enlarge. Further, filamentation can give electron heating as well [12], thus reducing $(v_{os}/v_e)^2$. Although difficult to confirm, there is separate experimental evidence for filamentation in the jet (Offenberger [53]) and it is feasible that filamentation could provide a mechanism to inhibit Brillouin scattering, at least until normal plasma rarefaction could do so.

A second possible mechanism to interfere with the Brillouin instability is enhanced short wavelength ion turbulence. An increase in the plasma resistivity due to strong density fluctuations, results in increased light absorption over classical inverse bremsstrahlung (Dawson and Oberman [63]). Faehl and Kruer [64] show that the ion turbulence absorption length is

$$L \approx 4v_g/[\omega_0(\delta n/n_c)^2] = 2\lambda_0/[\sqrt{1 - n/n_c} \pi |\delta n/n_c|^2]$$

where $|\delta n/n_c|^2$ is the square of the normalized homogeneous and isotropic density fluctuations. Ruby Thomson scattering measurements on the gas jet target have revealed short wavelength ($k\lambda_D \approx 0.5$) ion fluctuations in the plasma which grew as the Brillouin instability decayed (Al-Shiraida et al. [65]). A 240 micron absorption length is calculated from the observed $|\delta n/n_c|^2 = 0.04$. Although this length is larger than the 80 micron Brillouin interaction region, the integrated effect of the enhanced absorption over its extent in the plasma ahead of the focus could be sufficient to interrupt the Brillouin instability at later time as the turbulence develops. The classical absorption length for comparison, was ≈ 1.7 mm which is even larger still and is therefore unlikely to contribute to decrementing the laser pump.

Although several mechanisms are postulated for ion turbulence generation, one predicts an even worse situation if the Brillouin instability itself is participating in the ion turbulence generation. Ion trapping in the Brillouin ion fluctuation potential can excite a bump-in-tail instability (Davidson, [28]) whereby short wavelength ion fluctuations are generated (Kartunnen [62]). This new instability is an energy sink to the Brillouin ion fluctuations which lowers the Brillouin growth rate and at the same time is a source for the ion turbulence. The effectiveness of the mechanism has not been studied thoroughly but qualitatively suggests that the short wavelength ion turbulence produced in this manner can have a twofold influence on the Brillouin instability through laser pump absorption and ion wave damping. The ion fluctuations produced by this instability are nominally parallel with \underline{k}_0 and do not affect absorption. However, mode coupling and diffusion in k space may be important for large fluctuations. This bump in tail instability also succeeds in explaining the relative timing of the the two instabilities.

In conclusion, the abrupt termination of the stimulated Brillouin scattering is as yet unexplained though it is plausible that filamentation and strong ion turbulence which are known to exist, may account for the observed behaviour.

5. Conclusions

A comprehensive study of short and long pulse CO₂ laser induced Brillouin scattering at intensities $I \sim O(10^{13} \text{ W cm}^{-2})$ has been done. The careful characterization of the plasma parameters which included electron temperature, electron density and electron density gradients, allowed a quantitative interpretation of the stimulated Brillouin scattering results. Both the electromagnetic and electrostatic waves of the Brillouin decay triplet were detected and the dominant laser and plasma effects were identified.

The broadened, red-shifted spectrum of the CO₂ laser light backscattered from the oxygen plasma positively identified stimulated Brillouin scattering as the generating mechanism. Backscatter reflectivity and spectra for both the gain switched and IML laser suggested that a self consistent ion trapping/heating effect was responsible for elevating the ion temperature as required for ion Landau damping to broaden the instability's bandwidth. For the gain switched laser, a large ion wave damping coefficient, $\gamma_s/\omega_s = 0.6$ was estimated from the infrared backscatter reflectivity. The comparison of a kinetic, frequency dependent gain calculation to the backscattered light spectra yielded electron-to-ion temperature ratio estimates, $ZT_e/T_i = 1$. This small temperature ratio confirmed that strong ion Landau damping took place.

The IML laser backscatter results were a convincing demonstration of ion heating from the Brillouin interaction. The interaction time was too short for significant electron-ion collisional equilibration and yet the broad backscatter spectra again substantiated an ion trapping/heating description. A simple model prediction based on ion heating accounted for the IML laser reflectivity including the high backscatter at low laser intensities. The ion trapping/heating model was prepared from the WKB coupled mode equations with ion Landau damping from a fraction of the ions heated to temperatures $O(ZT_e)$.

Ion fluctuations driven by the Brillouin instability were diagnosed through Thomson scattering of a ruby laser probe beam. In Thomson scattering wavenumber measurements, the detected ion fluctuations were clearly those of the Brillouin instability since the measured k wavenumber corresponded to that expected from Brillouin wavenumber matching. No k_0 or $4k_0$ ion wave harmonics were detected in the Thomson scattering experiments, thus eliminating ion wave decay as a

Brillouin saturation mechanism at our laser intensities and for our plasma conditions. In a second experiment, measurements of the normalized ion fluctuation level, $\delta n/n$, and its \sqrt{R} reflectivity dependence, verified that convective saturation of the Brillouin instability through ion heating had indeed taken place. A third experiment was the direct observation of the Brillouin interaction zone through spatially and temporally resolved ruby Thomson scattering. The observed 80 micron interaction length was explained through wavenumber mismatch of the participating waves away from the instability's resonant point. This length coincided with earlier estimates made from the infrared backscattered light reflectivity. In these same experiments, the 500 ps ion fluctuation risetime was strong evidence for ion heating. These slow risetimes agreed with the model of heated ions diverting energy from the Brillouin ion waves to lower the Brillouin growth rate. Risetime estimates from the ion trapping/heating model were close to those observed.

A successful attempt was made to reduce the Brillouin scattering by using a multiwavelength CO₂ laser. The selected laser lines had to have frequency separations larger than the Brillouin homogeneous growth rate otherwise anomalous mode coupling occurred and reduced the effectiveness of the multiwavelength laser. This unique demonstration of SBS reduction is encouraging evidence that simple laser modifications can potentially improve laser-plasma coupling in fusion experiments.

The termination of SBS in the laser-plasma experiment is still not fully understood, although filamentation and enhanced pump absorption remain as the most likely candidates to lower the SBS gain below threshold. Both filamentation and strong ion turbulence have been observed in other experiments made with the CO₂ laser and gas jet target. Indeed, the cessation of SBS just before enhanced ion turbulence takes place, suggests that strong laser absorption could be interrupting the Brillouin instability.

In summary, the complete characterization of the laser, plasma and interaction parameters permitted the quantitative interpretation of the observed stimulated Brillouin scattering. Spectral, spatial and temporal measurements of SBS and the associated ion fluctuations strongly support the model of ion heating and wave damping along with the finite matching length.

Bibliography

- [1] J Nuckolls, L. Wood, A. Thiessen and G. Zimmerman, *Nature* 239, 139 (1972)
- [2] V.N. Oraevsky and R.Z. Sagdeev, *Zh. Tech Fiz.* 32, 1291 (1962)
- [3] R.N. Franklin et al, *Phys. Rev. Lett.* 27, 1119 (1971)
- [4] K. Nishikawa, *J. Phys. Soc. of Japan* 24, 916 (1968)
- [5] F.W. Perkins and J. Flick, *Phys. Fluids* 14, 1012 (1971)
- [6] M.N. Rosenbluth, *Phys. Rev. Lett.* 29, 565 (1972)
- [7] M.N. Rosenbluth, R.B. White and C.S. Liu, *Phys. Rev. Lett.* 31, 1190 (1973)
- [8] D. Pesme, G. Laval and R. Pellat, *Phys. Rev. Lett.* 31, 203 (1973)
- [9] J.F. Drake, P.K. Kaw, Y.C. Lee, G. Schmidt, C.S. Liu and M.N. Rosenbluth, *Phys. Fluids* 17, 778 (1974)
- [10] D.W. Forslund, J.M. Kindel and E.L. Lindman, *Phys. Fluids* 18, 1002 (1975)
- [11] D.W. Forslund, J.M. Kindel and E.L. Lindman, *Phys. Fluids* 18, 1017 (1975)
- [12] B.I. Cohen and C.E. Max, *Phys. Fluids* 22, 1115 (1979)
- [13] R.Y. Chiao, C.H. Townes and B.P. Stoicheff, *Phys. Rev. Lett.* 12, 592 (1964)
- [14] R. Massey, K. Berggren and Z.A. Pietrzyk, *Proc. of 5th Annual Anomalous Absorption*

conference, UCLA 1975; A.A. Offenberger, M.R. Cervenak, A.M. Yam and A.W. Pasternak, J. Appl. Phys. 47, 1451 (1976)

[15] F.J. Mayer, G.E. Busch, C.M. Kinzer and K.G. Estabrook, Phys. Rev. Lett. 44, 1498 (1980)

[16] F.F. Chen, Third Workshop on "Laser Interaction and Related Plasma Phenomena" Troy, N.Y. 1973

[17] B.D. Fried and S.D. Conte, The Plasma Dispersion Function (Academic Press N.Y. 1961)

[18] S. Ichimaru, Basic Principles of Plasma Physics (W.A. Benjamin Inc. Reading Mass. 1973)

[19] A.A. Offenberger, A. Ng and M.R. Cervenak, Can. J. Phys. 56, 381 (1978)

[20] C.N. LashmoreDavies, Plasma Physics 17, 281 (1975)

[21] W.M. Manheimer and D.G. Colombant, Phys. Fluids 24, 447 (1981)

[22] C.L. Tang, J. Appl. Phys. 37, 2945 (1966)

[23] M. Born and E. Wolf, Principles of Optics (5th ed.) (Pergamon Press Oxford 1975)

[24] A. Ng., A.A. Offenberger and S.J. Karttunen, Optics Comm. 36, 200 (1981)

[25] V.N. Tsytovich, Nonlinear Effects in Plasma, (Plenum Press N.Y. 1970)

[26] D.W. Phillion, W.L. Kruer and V.C. Rupert, Phys. Rev. Lett. 39, 1529 (1977)

- [27] J.J. Thomson, Nucl. Fus. 15, 237 (1975)
- [28] R.C. Davidson, Methods in Nonlinear Plasma Theory, (Academic Press N.Y. 1973)
- [29] J.M. Dawson, W.L. Kruer and B. Rosen in Dynamics of Ionized Gases edited by M. Lighthill, I. Imai and H. Sato, (University of Tokyo Press, Tokyo 1973) p 47
- [30] K. Estabrook, J. Harte, E.M. Campbell, F. Ze, D.W. Phillion, M.D. Rosen and J.T. Larsen, Phys. Rev. Lett. 46, 724 (1981)
- [31] J. Weiland and H. Wilhelmsson, Coherent Non-Linear Interaction of Waves in Plasmas, (Pergamon Press 1977) pp 104–120
- [32] N.H. Burnett and A.A. Offenberger, J. Appl. Phys. 44, 3617 (1973)
- [33] H.J. Sequin, J. Tulip and D.C. McKen, IEEE J-QE Vol. QE10, 311 (1974)
- [34] O.P. Wood II, Proc. IEEE 62, 355 (1974)
- [35] K.J. Andrews, P.E. Dyer and D.J. James, J. Phys. E 8, 493 (1975)
- [36] A.E. Siegman, Appl. Optics 13, 353 (1974)
- [37] T. Li, Bell Sys. Tech. J., 917 (1965)
- [38] H. Kogelnik and T. Li, Proc. IEEE 54, 1312 (1966)
- [39] P.B. Corkum, Laser Focus, June, 80 (1979)
- [40] K.R. Manes and H.J. Sequin, J. Appl. Phys. 43, 5073 (1972)

- [41] P.B. Corkum and A.J. Alcock, Opt. Comm. 26, 103 (1978)
- [42] J.D. Cobine, Gaseous Conductors, (Dover Publ. N.Y. 1958) p 29
- [43] M. Pilch, Opt. Commun. 7, 397 (1973)
- [44] P.E. Dyer and I.K. Perara, Opt. Lett. 4, 250 (1979)
- [45] A.H. Shapiro, The Dynamics and Thermodynamics of Compressible Fluid Flow Vol. 1 (Ronald Press Co. N.Y. 1953) p 462
- [46] B.W. Arnold and A.A. Offenberger, Rev. Sci. Instrum. 47, 762 (1976)
- [47] R.N. Jones et al., Spectrochimica Acta 23A, 925 (1967)
- [48] R.C. Elton and A.D. Anderson, NRL Report 6541, Mar. 1967
- [49] J. Sheffield, Plasma Scattering of Electromagnetic Radiation (Academic Press N.Y. 1975)
- [50] N.H. Schiller and R.R. Alfano, Opt. Commun. 35, 451 (1980)
- [51] J. McMullin, University of Alberta, private communication
- [52] M.J. Herbst, C.E. Clayton, W.A. Peebles and F.F. Chen, Phys. Fluids 23, 1319 (1980)
- [53] A.A. Offenberger, Modern Plasma Phys., 437 (1981)
- [54] R.H. Lehmberg and B.H. Ripin, Proc. Int. Conf on Lasers, Orlando Florida (1978)
- [55] C.E. Clayton, C. Joshi, A. Yasuda and F.F. Chen, Phys. Fluids 24, 2312 (1981)

- [56] R.S. Massey, Z.A. Peitzyk and D.W. Scudder, *Phys. Fluids* 21, 396 (1978)
- [57] American Institute of Physics Handbook 3 rd edition, edited by D.E. Gray, (McGraw Hill N.Y. 1980) p7-200
- [58] D.R. Gray and J.D. Kilkenny, *Plasma Phys.* 22, 81 (1980)
- [59] S.J. Karttunen and R.R.E. Salomaa, *Phys. Lett.* 88A, 350 (1982)
- [60] S.J. Karttunen, J.N. McMullin and A.A. Offenberger, *Phys. Fluids* 24, 447 (1981)
- [61] C.J. Walsh and H.A. Baldis, *Phys. Rev. Lett.* 48, 1483 (1982)
- [62] S.J. Karttunen and J.A. Heikkinen, *Plasma Phys.* 23, 869 (1981)
- [63] J.M. Dawson and C. Oberman, *Phys. Fluids* 6, 394 (1963)
- [64] R.J. Faehl and W.L. Kruer, *Phys. Fluids* 20, 55 (1977)
- [65] Y.S. AlShiraida, A.A. Offenberger and A. Ng, *Phys. Rev. A* 25, 2857 (1982)
- [66] C.J. Cromaus and R.C. Birkebak, *Appl. Optics* 5, 1057 (1966)

Appendix A

Nonlinear Equations

Several nonlinear equations had to be solved including the ion heating reflectivity calculation in Eq. 2.26, the ion trapping in Eq. 2.32 and the stimulated Brillouin dispersion relation in Eq. 2.11. The first two nonlinear equations were solved through Newton Raphson methods implemented on a computer. Except in the simplest nonlinear equations, the function derivative was approximated by a forward difference so the iteration formula became:

$$x_{i+1} = x_i - hf(x_i)/(f(x_i + h) - f(x_i))$$

Careful selection of initial values of x were required due to the exponential behaviour of the nonlinear equations. The simultaneous nonlinear equations describing the stimulated Brillouin dispersion were solved through an iterative substitution method as described in Chapter 2.

Ordinary Differential Equations

Systems of ordinary differential equations had to be solved for the rate equation model of the injection mode locked laser, the spatial coupled mode equations, and the temporal coupled mode equations. A second order Runge-Kutta integration formula was used with interval halving to ensure that the error was within 0.5%. The two step computational method used to calculate $y_j \quad 1 \leq j \leq N$ was:

$$\begin{aligned}\bar{y}_{ji} &= y_{ji} + hy_j'(x_i, y_{1i}, \dots, y_{Ni})/2 \\ y_{j(i+1)} &= y_{ji} + hy_j'(x_i + h/2, \bar{y}_{1i}, \dots, \bar{y}_{Ni})/2\end{aligned}$$

The above shows the calculation of y_{j+1} from y_j with step size h .

Deconvolution of Spectra

The analysis of spectral data was complicated by the instrumental function of the dispersing elements. In particular, the resolution of a grating spectrograph is determined by the number of grating lines, N , dispersing the incident light, i.e., $\Delta\lambda/\lambda = 1/N$ for first order diffraction. For infrared light measurements with the 75 lines/mm grating spectrometer, the resolution is 28 \AA which is the same order of magnitude as the detected line shifts and width in Brillouin backscattered light. The pseudodeconvolution of Jones et al [47] was used to remove the instrumental responses from the spectra. This iterative method involves convolving the original data with the instrument response and the resulting function is compared with the original data to give a measure of the spectral broadening. The algorithm for this discrete point method is:

$$\left. \begin{aligned} (1) \quad S' &= S_i \times (S_i/C(S_i)) \\ (2) \quad S_{i+1} &= S' \times (S_i/C(S')) \end{aligned} \right\} \quad \text{for } 0 \leq i \leq n$$

where $C(S_j)$ is the convolution of the j^{th} spectrum S_j with the instrument function. To reduce computational noise, a five point least squares smoothing was passed over each S_i

$$\bar{S}_{ik} = [17S_{ik} + 12(S_{i(k-1)} + S_{i(k+1)}) - 3(S_{i(k-2)} + S_{i(k+2)})]/35$$

where \bar{S}_{ik} is the k^{th} averaged point of S_i . Typically four iterations were used to deconvolve the spectra and S_n were convolved with the instrument function for comparison with the original data S_0 to ensure that it could be recovered.

Abel Transform

The computation of radial functions from data integrated along cords in a cylindrically symmetric system is achieved through the Abel transform. This transform was applied to a numerical routine used to invert plasma interferograms and obtain the radial electron density profiles at various axial positions in the plasma. The usual inversion formula for refractive index can be written

$$\mu(r,z) - 1 = \frac{-\lambda}{\pi} \int_U^{U_s} \frac{d\delta}{du} (u - U)^{-1/2} du$$

where $\mu(r,z)$ is the refractive index at radial position r in a cylindrically symmetric plasma of radius r_s . The fringe shift at u is δ where $u = r^2$ and $U_s = r_s^2$. The refractive index profile is related to the electron density by $\mu^2 = 1 - n_e e^2 / \epsilon_0 m_e \omega^2$ from which $n_e(r,z)$ is found. A linear approximation to $d\delta/du$ between data points reduces the integral to the numerical computation:

$$\mu_i - 1 = \sum_{j=1}^{N-1} 2 \frac{\delta_{j+1} - \delta_j}{u_{j+1} - u_j} [(u_{j+1} - u_i)^{1/2} - (u_j - u_i)^{1/2}]$$

The refractive index at the i th of N equispaced data points is μ_i . Although this is a highly simplified computation scheme (for comparison see for example [66]), tests done on analytic solutions confirmed its accuracy to within a satisfactory 5%.

Plasma Susceptibility Calculation

The kinetic limit of the SBS dispersion relation in Equation 2.11 required the ion susceptibility $\chi_i(\omega, k) = (k_{Di}^2/k^2)W(z)$ where

$$W(z) = 1 - z \exp(-z^2/2) \int_0^z \exp(-y^2/2) dy + i\sqrt{\pi/2} z \exp(-z^2/2)$$

and $z = \omega/v_j k$ which is complex. The function $W(z)$ is related to the usual plasma dispersion function $\Gamma(z)$ (Fried and Conte [17]) by:

$$W(z) = (z/\sqrt{2}) \cdot \Gamma(z/\sqrt{2}) + 1$$

Two computations were appropriate for calculating $W(z)$ and $\Gamma(z)$, depending upon $\text{Im}(z)$. When $|\text{Im}(z)| > 1$, a continued fraction algorithm (Fried and Conte) was used to compute $\Gamma(z)$ from which $W(z)$ was derived. A convergent series (Ichimaru [18]) gave $W(z)$ directly for all other cases. These two algorithms are summarized below with corrections to the original references.

$$|\text{Im } z| > 1$$

$$\text{if } \text{Im } z > 1 \quad \Gamma(z) = \lim_{n \rightarrow \infty} (A_n/B_n)$$

$$\text{where} \quad A_{n+1} = b_{n+1}A_n + a_{n+1}A_{n-1} \quad A_{-1} = 1 \quad A_0 = 0$$

$$B_{n+1} = b_{n+1}B_n + a_{n+1}B_{n-1} \quad B_{-1} = 0 \quad B_0 = 1$$

with

$$a_1 = z$$

$$a_{n+1} = -n(2n - 1)/2 \quad n = 1, 2, \dots$$

$$b_{n+1} = -z^2 + 1/2 + 2n$$

$$\text{if } \text{Im } z < -1 \quad \Gamma(z) = \Gamma(z^*) + i2\sqrt{\pi} \exp(-z^2)$$

$$-1 \leq \text{Im } z \leq 1$$

$$W(z) = i\sqrt{\pi/2} z \exp(-z^2/2) + 1 + \sum_{j=0}^N T_j$$

$$T_0 = -z^2$$

where

$$T_{n+1} = T_n(-z^2/(2n + 3))$$

Appendix B

Free Jet Program

The method of solution for free jet flow is well known from hodograph theory (Shapiro [45]). Reference should be made to elementary texts on supersonic flow theory to assist in understanding the equations in this appendix. Figure B.1 is a diagram of the free jet showing the Mach lines a-h separating flow fields 1 to 8. Upon crossing a Mach line, the gas flow parameters change, consistent with the various isentropic relations. The free boundary angle, θ_0 is found first by calculating the Mach number, M_3 in region 3 from pressure balance $P_3 = P_A$ where P_3 is the pressure in region 3 and P_A is the ambient pressure (pressure difference does not occur across stationary free boundaries) and then applying the Prandtl-Meyer equation. The change of the flow direction when going from region 1 to region 3 is

$$\theta_0 = \omega_1 - \omega_3 \quad . \text{ The two equations for calculating the above are}$$

$$M = [(2/(\gamma - 1))(P_0/P_A)^{(\gamma-1)/\gamma} - 1]^{1/2} \quad \text{Eq. B.1}$$

$$\omega(M) = \text{Atan}(M^2 - 1) - \left(\frac{\gamma + 1}{\gamma - 1} \right)^{1/2} \text{Atan} \left(\frac{\gamma - 1}{\gamma + 1} (M^2 - 1) \right)^{1/2} \quad \text{Eq. B.2}$$

Equation B.1 is an isentropic flow relation and B.2 is the Prandtl-Meyer equation. The ratio of specific heats, γ is equal to 1.4 for a diatomic molecule. For example, if

$P_0 = 2000$ Torr, $P_A = 10$ Torr and $M_1 = 2.96$ (from the nozzle calculations outlined in Chapter 3) then $M_3 = 4.21$ and

$$\theta_0 = -(\omega(4.21) - \omega(2.96)) = 68.45 - 48.98 = 19.47^\circ$$

Depending upon whether a Mach line is a compression (Type I) wave or rarefaction wave (Type II), the flow direction after crossing them is determined from

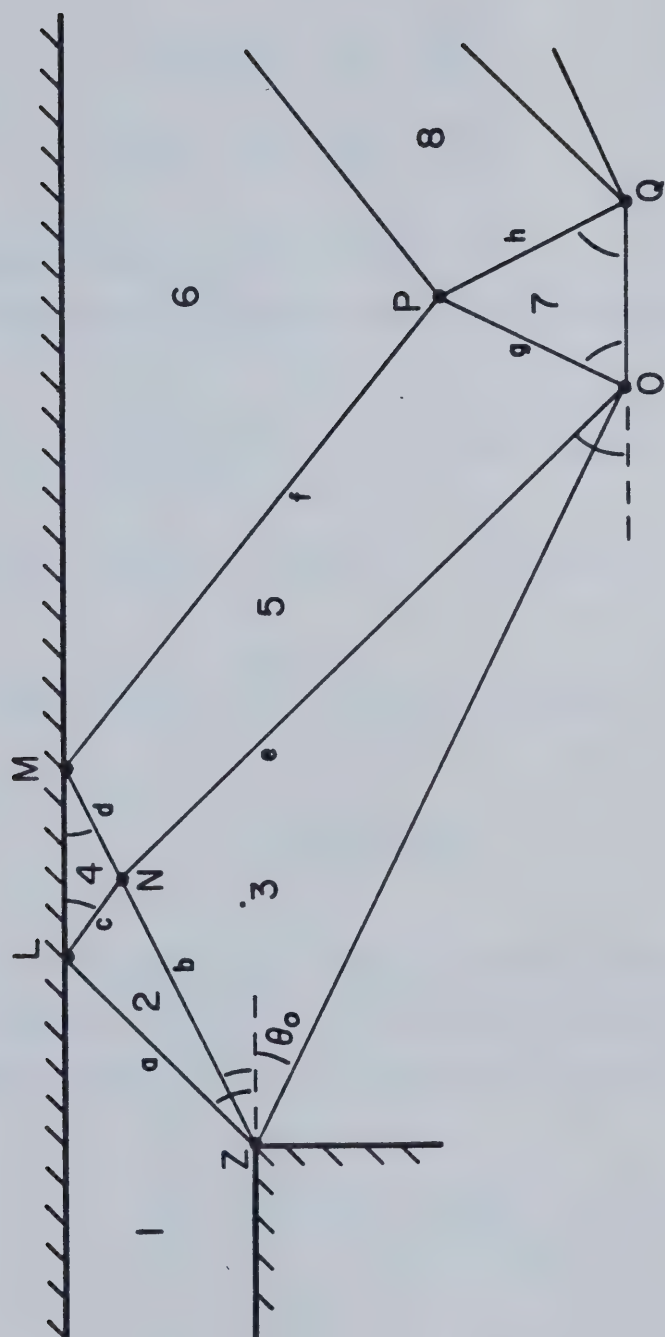


Figure B.1 Flow fields and Mach Lines in a Gas Jet

θ_I and θ_{II} defined as

$$\theta_I = -\omega(M) + 2I - 1000$$

$$\theta_{II} = \omega(M) + 2II - 1000$$

The integration constants $2I - 1000$ and $2II - 1000$ are useful during computations. From above, if one travels from flow field i to flow field j , then

$$\theta_j - \theta_i = \omega_j - \omega_i \quad \text{for Type I}$$

$$\theta_j - \theta_i = -(\omega_j - \omega_i) \quad \text{for Type II}$$

Eq. B.3

A type II Mach line is inclined to the jet axis at an angle $\overline{\alpha + \theta}$ where

$$\alpha = \text{Atan}(1/\sqrt{M^2 - 1})$$

Clearly α is the angle that the Mach line makes to the downstream streamlines and θ is added to it to restore it to an angle with respect to the jet axis. Similarly, a type I Mach line is at angle $\overline{\theta - \alpha}$ to the jet axis. Equation B.3 can be rewritten as

$$\theta = I + II - 1000$$

$$\omega = I - II$$

The variable I is unchanged when crossing a type II wave, and II is unchanged when a type I wave is crossed. It is then a simple matter to calculate θ , ω for different flow regions in the jet. From ω , M is calculated with Equation B.2 and then α

from above. Once all θ and α are known, then all Mach line angles are determined. From this information, trigonometric relations are used to locate the intersection of the Mach lines and the flow field pattern can be drawn.

The free jet program below is written for a Texas Instruments 99/4A computer.

The key variables are:

$A(2,8)$ = (I,I) values for the 8 fields

$OM(8)$ = ω

$TH(8)$ = θ for the 8 fields

$MM(8)$ = M for the 8 fields

$AL(8)$ = α for the 8 fields

$A1-G1$ = Mach line angles to the jet axis

$XX(N), YY(N)$ = x,y coordinates of the points L to Q

```

100  DIM A(28)
110  REM FIRST CALCULATE W(M1),W(M3)
120  INPUT "PO,PA": PO,PA
130  M3=SQR(5*((PO/PA)!.4/1.4)-1))
140  M4=M3
150  REM 1170 IS W(M) SUBROUTINE
160  GOSUB 1170
170  W1=W
180  M4=2.96
190  GOSUB 1170
200  REM INITIAL AND B.C.
210  OM(1)=W
220  TH(1)=0
230  TH(3)=W-W1
240  TH(2)=TH(3)/2
250  TH(4)=0
260  TH(6)=0
270  TH(7)=0
280  REM START OF FIELD CALC.
290  A(1,1)=500+OM(1)/2+TH(1)/2
300  A(2,1)=500-OM(1)/2+TH(1)/2
310  A(1,2)=A(1,1)
320  OM(2)=2*A(1,1)-TH(2)-1000
330  A(2,2)=(1000-OM(2)+TH(2))/2
340  A(1,3)=A(1,2)
350  OM(3)=2*A(1,2)-TH(3)-1000
360  A(2,3)=(1000-OM(3)+TH(3))/2
370  A(2,4)=A(2,2)

```



```

380 OM(4)=1000-2*A(2,2)
390 A(1,4)=1000+OM(4)+TH(4))/2
400 A(1,5)=A(1,4)
410 A(2,5)=A(2,3)
420 OM(5)=A(1,4)-A(2,3)
430 TH(5)=A(1,4)+A(2,3)-1000
440 OM(6)=1000+TH(6)-2*A(2,5)
450 A(2,6)=A(2,5)
460 A(1,6)=1000+OM(6)+TH(6))/2
470 A(1,7)=A(1,5)
480 OM(7)=2*A(1,5)-1000
490 A(2,7)=(1000-OM(7))/2
500 A(1,8)=A(1,6)
510 A(2,8)=A(2,7)
520 OM(8)=A(1,6)-A(2,7)
530 TH(8)=A(1,6)+A(2,7)-1000
540 FOR I=1 TO 8
550 T=OM(I)
560 GOSUB 1000
570 MM(I)=M
580 AL(I)=57.29578*ATN(1/SQR(M*M-1))
590 NEXT I
600 PRINT "MACH + STREAM ANGLES"
610 FOR I=1 TO 8
620 PRINT OM(I),TH(I)
630 NEXT I
640 PRINT "MACH NO, ALPHA"
650 FOR I=1 TO 8
660 PRINT MM(I),AL(I)
670 NEXT I
680 A1=(TH(1)+TH(2)+AL(1)+AL(2))/2
690 B1=(TH(2)+TH(3)+AL(2)+AL(3))/2
700 C1=(AL(2)+AL(4)-TH(2)-TH(4))/2
710 D1=(TH(4)+TH(5)+AL(4)+AL(5))/2
720 E1=(AL(3)+AL(5)-TH(3)-TH(5))/2
730 F1=(AL(5)+AL(6)-TH(5)-TH(6))/2
740 G1=(TH(5)+TH(7)+AL(5)+AL(7))/2
750 H1=(AL(7)+AL(8)-TH(7)-TH(8))/2
760 Q=1/57.29578
770 XX(1)=1/TAN(Q*A1)
780 YY(1)=1
790 XX(3)=(1+XX(1)*TAN(Q*C1))/(TAN(Q*B1)+TAN(Q*C1))
800 YY(3)=1-(XX(3)-XX(1)*TAN(Q*C1)
810 XX(2)=XX(3)+(1-YY(3))/TAN(Q*D1)
820 YY(2)=1
830 XX(4)=(XX(3)*TAN(Q*E1)+YY(3))/(TAN(Q*E1)-TAN(-TH(3)*Q))
840 YY(4)=-XX(4)*TAN(-TH(3)*Q)
850 XX(5)=(1-YY(4)+XX(2)*TAN(Q*F1)+XX(4)*TAN(Q*G1)/
      (TAN(Q*F1)+TAN(Q*G1))
860 YY(5)=YY(4)+(XX(5)-XX(4))*TAN(Q*G1)
870 XX(6)=XX(5)+(YY(5)-YY(4))/TAN(Q*H1)
880 YY(6)=YY(4)
890 PRINT "CHARACTERISTIC COORD."

```



```

900   FOR I=1 TO 6
910   PRINT XX(I),YY(I)
920   NEXT I
930   PRINT "FIELD DENSITIES"
940   FOR I=1 TO 8
950   M=MM(I)
960   GOSUB 1210
970   PRINT NC
980   NEXT I
990   END
1000  G=1.4
1010  GG=SQR(G+1)/(G-1))
1020  M=1.1
1030  DM=.0001
1040  M1=M
1050  GOSUB 1130

1060  F1=F
1070  M1=M+DM
1080  GOSUB 1130
1090  M2=M
1100  M=M2-DM*F1/(F-F1)
1110  IF ABS(M2-M)>1E-4 THEN 1040
1120  RETURN
1130  MR=SQR(M1*M1-1)
1140  F=57.29578*(GG*ATN(MR/GG)-ATN(MR))-T
1150  RETURN
1160  REM W(M) SUBROUTINE
1170  GG=SQR((2.4/.4))
1180  MR=SQR(M4*M4-1)
1190  W=57.29578*((GG*ATN(MR/GG)-ATN(MR))
1200  RETURN
1210  G=1.4
1220  P=PO/(1+.2*M*M)!2.5
1230  NC=P/2000*12*6.41
1240  RETURN

```


Appendix C

Fresnel Mirrors Interferometer

The plasma electron density measurements reported in this thesis were generated from the Abel inversion of interferograms. Implementing a workable and convenient interferometer was not as trivial as it would first seem. The usual folded wavefront and Mach-Zender interferometers were tried and found unsatisfactory. Both of these are division of wavefront interferometers with an unacceptable 50% reduction of the interferogram exposure. Also, the Mach-Zender optical elements were located inside the experiment target chamber, making adjustments awkward. Finally, the minimum number of critical components in the Fresnel Mirrors interferometer made it attractive to use.

Figure C.1(a) and C.1(b) will be referred to in explaining the interferometer. Several design goals had to be satisfied simultaneously through the appropriate selection of lenses' focal lengths and positions. These design objectives included the image magnification, fringe spacing, lens L1 clearance from the CO₂ laser beam and not damaging the exit etalon with focussed Ruby laser light. The expanded and collimated laser light passed through the plasma position O1 in figure C.1(a). One half of the laser light was the reference beam and the other half the test beam. The telescope lenses were separated by $f_1 + f_2$ to recollimate the Ruby light. At the same time the fringes were localized at the plasma. From the thin lens equation, the real image location,

I_2 and telescope magnification M were

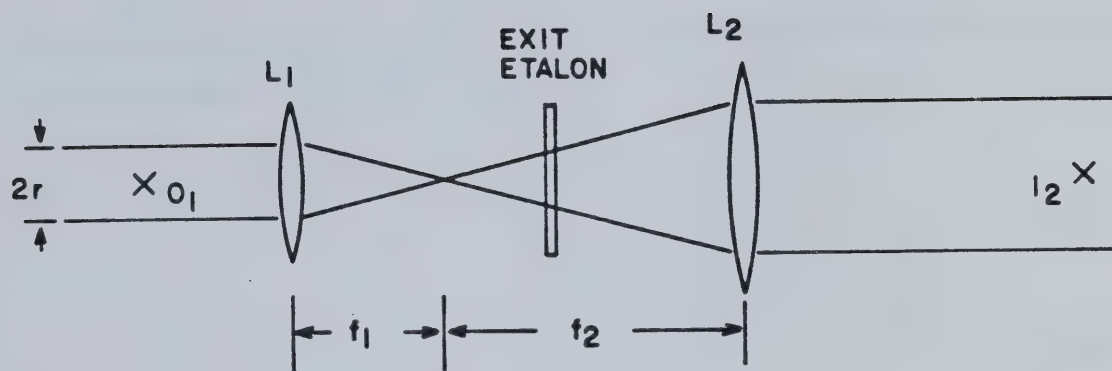
$$I_2 = (1 + M^*)f_2 - O_1 M^{*2} \quad \text{Eq. C.1}$$

$$M = I_2/O_1 \quad \text{Eq. C.2}$$

where $M^* = f_2/f_1$

The overall magnification, M_T was the product of M and the camera magnification, M_{camera} . The Fresnel mirrors were slightly inclined to each other (angle ϕ in Fig. C.1(b)) to cause beam overlap. By locating the mirrors very close to L2, $D \sim I_2$. Further, the interference fringe spacing at I_2 was

(A) IMAGING LENSES



(B) FRESNEL MIRRORS

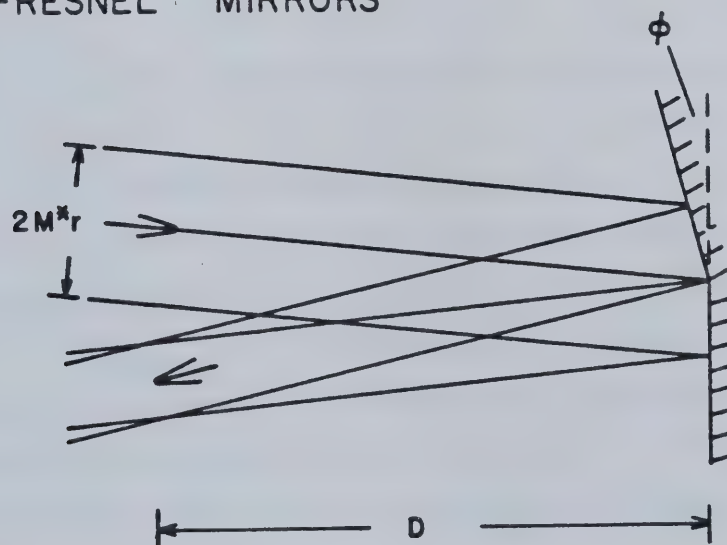


Figure C.1 Principal Interferometer Components

$\Delta x = \lambda I_2 / rM^*$, where λ was the Ruby laser wavelength in this case. The width of the overlapping area was rM^* . Referring this fringe spacing back to the plasma, the interferometer's line resolution is then:

$$\Delta x_p = \Delta x / M \quad \text{Eq. C.3}$$

Some convenience results in normalizing O_1 and obtaining slightly different expressions for the magnification and resolution. These are:

$$M = [M^* + M^{*2}(1/O_1^* - 1)] \quad \text{Eq. C.4}$$

$$\Delta x_p = \lambda O_1^* f_1 / rM^* \quad \text{Eq. C.5}$$

where $O_1^* = O_1 / f_1$

Figure C.2 shows O_1^* as a function of M^* for various M .

Once M^* and M are selected, O_1^* is easily determined from Fig. C.2.

Also, $I_2^* = M O_1^*$ where $I_2^* = I_2 / f_1$. One set of parameters for the interferometry are indicated with intersecting dashed lines. In this particular arrangement,

$f_1 = 30$ cm and $rM^* = 0.7$ cm, and the resolution is calculated with

Equation C.5 to be 26 microns. This fringe spacing corresponds very closely to the 25 micron resolution estimated from counting 8 He-Ne laser fringes across a 200 micron diameter alignment microball positioned at the CO_2 laser focus. The overall magnification,

$M_T = M \times M_{\text{camera}}$ was 50X onto the Polaroid type 410 film in the

interferometry camera. It should be mentioned that CO_2 laser beam clearance and a safe Ruby laser intensity onto the exit etalon were also satisfied in this configuration. Normal Abel inversion analysis was then done on the collected interferograms.

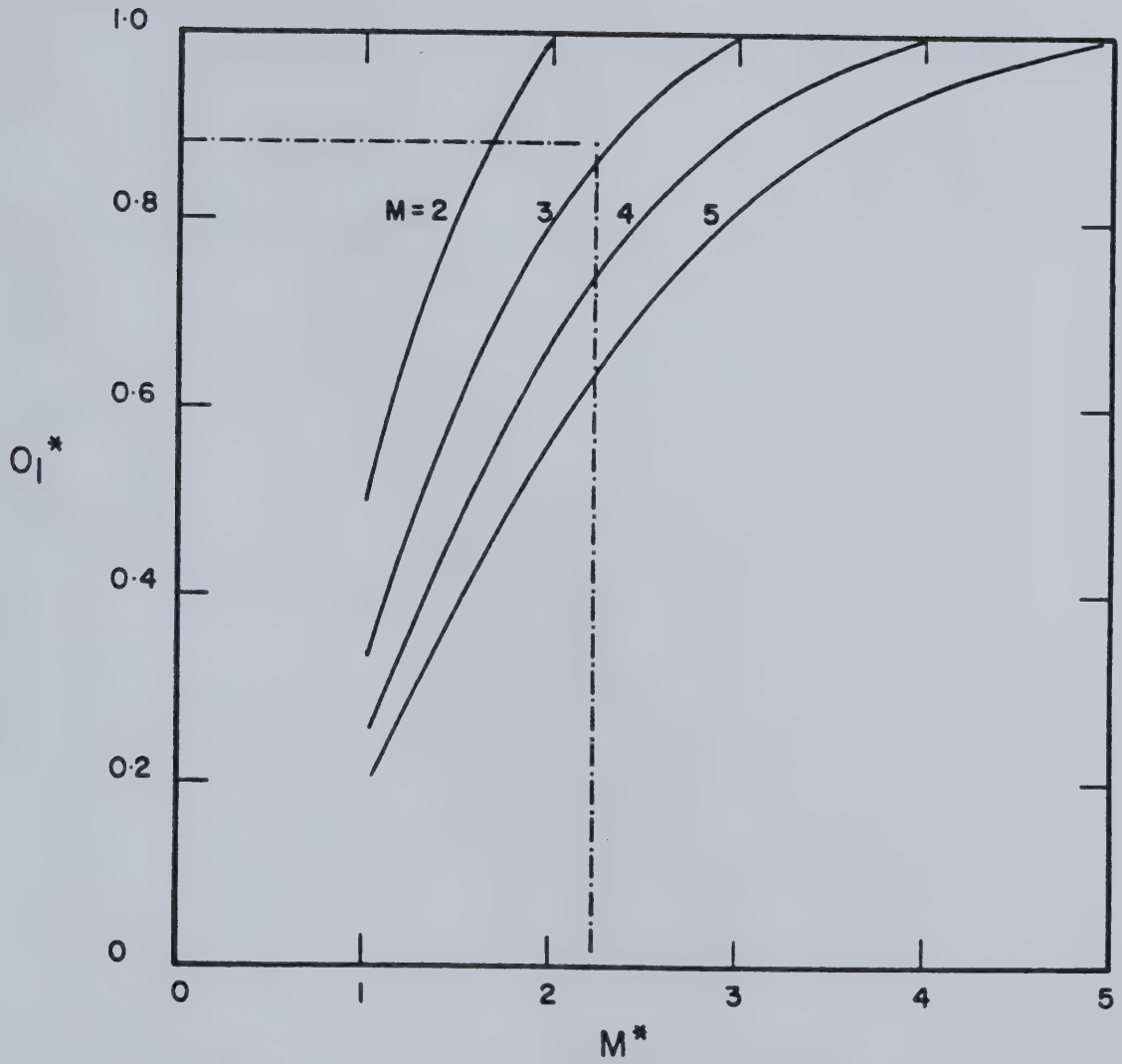


Figure C.2 Interferometer Design Parameters

B30392